STRUCTURE AND ELECTRICAL PROPERTIES OF STRONTIUM ZIRCONATE

Nongluck Pankurddee Suriyayothin
B.Sc., Chulalongkorn University, Bangkok, Thailand, 1970
M.E., Youngstown State University, Youngstown, Ohio, U.S.A., 1979

A dissertation submitted to the faculty
of the Oregon Graduate Center
in partial fulfillment of the
requirements for the degree
Doctor of Philosophy
in
Materials Science and Engineering

July, 1984

The dissertation "Structure and Electrical Properties of Strontium Zirconate" by Nongluck Suriyayothin has been examined and approved by the following Examination Committee:

Nicholas G. Eror, Thesis Advisor
Professor

Jack H. Devletian
Associate Professor

Richard A. Elliott
Professor

Thomas M. Loehr
Professor

© 1985

NONGLUCK PANKURDDEE SURIYAYOTHIN

All Rights Reserved

DEDICATION

To dearest Art

ACKNOWLEDGEMENT

I thank Prof. N.G. Eror for his guidance throughout this work. I also thank Profs. R.A. Elliott, J.H. Devletian and T.M. Loehr for reviewing my thesis and Prof. W.E. Wood for his support. I am indebted to Profs. T.M. Loehr and R. Drosd for the many invaluable discussions I had with them. I also thank especially A. Ryall, B. Ryall, M. Seaman, C. Lightcap, J. Bar-Tzur, S. Sibbett, M. Gesley, M. Scholl, R.Uhde R. Turpin and D. Robert for their help during some phases of this project. Special thanks are due to Dr. U. Balachandran for his assistance in the initial stages of my research and Dr. R. Padmanabhan for his help with electron microscopy studies.

TABLE OF CONTENTS

LIST OF TABLES

LIST OF FIGURES

ABSTRACT

Undoped and doped $SrZrO_3$ compounds find a variety of uses as semiconductor and dielectric materials, in MHD flow, as piezoelectric crystals and in many device applications such as delay lines, slow wave structures, optical modulators etc. However, studies on the electrical characteristics and defect structure analysis of these perovskites are surprisingly sparse. Further, systematic efforts to understand the electrical behavior of these pure and doped crystals on the basis of point defect chemistry and structure are lacking.

This investigation addresses some of the above issues. First, the different defect disorders in ternary ionic crystals of the type ABO_3 were considered and defect concentrations as functions of several independent thermodynamic variables were evaluated. This analysis was then applied to interpret the specific case of the electrical behavior of $SrZrO_3$. The analysis was next extended to explain the effects of partially and completely ionized foreign atoms, both acceptors and donors, added intentionally or present as impurities, to achieve controlled properties. Equilibrium conductivity experiments were performed over a wide range of temperature, P_{O_2} and dopant concentration and the applicability of point defect chemistry in solving these results was demonstrated. The range of existence of the homogeneous perovskite phase, $SrO-La_2O_3-ZrO_3$, within which conductivity measurements were made, was evaluated through a series of experiments involving scanning and transmission electron microscopy and x-ray diffractometry. Thermogravimetric studies, under both oxidizing and reducing conditions, were conducted to understand the self-compensation phenomenon in $SrZrO_3$ with dopant additions and a model was proposed to explain the compensation process. The underlying mechanisms involved in the conduction process were also directly studied through diffusion experiments, by following the kinetics of interdiffusion through transient electrical conductivity measurements, again over a wide range of temperature and P_{O_2} steps. Chemical diffusion coefficients were also calculated through these transient conductivity data and the activation enthalpies for the total process of diffusion of the diffusing species were evaluated from both the transient and equilibrium conductivity results. A limited attempt was also made to investigate interdiffusion in (Sr,Ba)ZrO_3 diffusion couples, since these compounds are particularly useful in device applications. Finally, a comprehensive study was made of laser-excited Raman spectral characteristics of undoped and doped zirconates at various temperatures. Factor group analysis was carried out to interpret the results and a correlation method was used to obtain vibrational selection rules. The predicted lattice vibrations from the irreducible representations and the spectral activity of each mode were used for band assignment of the observed Raman spectra.

1. INTRODUCTION

All real crystals contain imperfections which may be point, line, surface or volume defects and which disturb locally the regular arrangement of atoms. These defects play an important role in determining the properties of crystals.

For the purpose of this present work, a distinction is first made between point defects which can exist in a state of complete thermodynamic equilibrium and one- or two- dimensional imperfections where concentrations are not determined by thermodynamic equilibria. Nonequilibrium defects may be very stable, especially at lower temperatures, but it is impossible to create them thermally in an ideal crystal solely by a slow raising of temperature.

Primary defects can be divided in turn into two types - atomic defects and electronic defects. Vacant lattice sites, interstitials and foreign atoms are the major atomic defects and excess electrons in the conduction band and holes in the valence band are the major electronic defects that are considered in this discussion.

In the past fifty years or so, interest in disorder in ionic crystals was mainly directed towards binary systems. An excellent summary of disorder in binary system was compiled by Kroger and Vink (1). Only recently have researchers turned their attention to ternary compounds (2). The purpose of this present work is to make a study of point defects in ternary ionic compounds. A ternary ionic crystal consists of one phase and three components. To define the thermodynamic state of the crystal, four state variables must be fixed in accordance with the phase rule. In a ternary system, it is generally convenient (theoretically) to fix the thermodynamic activity of one of the cations or the ratio of the two types of cations in addition to temperature (T), total pressure (P) and partial pressure of oxygen (P_{O_2}) . If four of the state variables are not fixed, the state is not defined, and measurements of disorder phenomena are generally meaningless.

1.1 Defects in Ternary Crystals

The defect disorder in binary systems have been studied thoroughly (1,3-5). From the knowledge of binary crystals it is to be expected that in ternary ionic crystals also the limiting cases of disorder types exist generally.

In a stoichiometric binary compound (MX), five primary types of atomic disorder can be distinguished (3-8):

1. Frenkel defect : equal numbers of vacancies on X sublattice (V_x) and X interstitial atoms (X_i), viz.,

$$MX = MX_{(1-\delta)}+\delta V_x+\delta X_i \qquad \delta<<1 \tag{1.1}$$

2. Frenkel defect : equal numbers of vacancies on M sublattice (V_m) and M interstitial atoms (M_i), viz.,

$$MX = M_{1-\delta}X+\delta M_i+\delta V_m \tag{1.2}$$

3. Schottky - Wagner : equal numbers of vacant sites on M sublattice (V_m) and X sublattice (V_x), viz.,

$$MX = MX+\delta V_m+\delta V_x \tag{1.3}$$

4. Anti - Schottky - Wagner defect : equal numbers of M and X interstitial atoms, viz.,

$$MX = M_{1-\delta}X_{1-\delta}+\delta M_i+\delta X_i \tag{1.4}$$

5. Antistructure defect : M atoms occupying X sites and X atoms occupying M sites, viz.,

$$MX = M_{1-\delta}X_{1-\delta}+\delta M_x+\delta X_m \tag{1.5}$$

In an actual crystal, several of these types of disorder may coexist. The occurrence of one type does not preclude the existence of another type.

In contrast to binary compounds, multicomponent ionic crystals have an appreciably greater number of possible disorder types. In this section, the calculation of equilibrium defect concentrations as functions of the different independent, thermodynamic variables is demonstrated for the case of a ternary perovskite ABO_3, in order to obtain explicit expressions which can be applied to practical problems.

1.2 Stoichiometric Equation for Ions and Sites

The defect notations of Kroger and Vink (1) are given in Table 1.1. This notation uses dots to indicate excess positive charges and primes to indicate excess negative charges related to the nominal electrostatic charges of the normal lattice constituents.

For the formation of a ternary oxide from two binary oxides, according to the equation :

$$ABO_3 = AO + BO_2 \tag{1.6}$$

a chemical equation can be generated as :

$$(1+\alpha)AO+(1+\beta)BO_2 = A_{1+\alpha}B_{1+\beta}O_{3+\alpha+2\beta} \tag{1.7}$$

It is assumed that electronic disorder is negligible. With this notation, the stoichiometry of the crystal is defined by the ratio of the two constituent binary oxides, viz.,

$$\frac{1+\beta}{1+\alpha} = 1+y \tag{1.8}$$

This is the site balance equation, where $y \approx 0$ defines a stoichiometric perovskite, $y>0$ defines a perovskite containing excess BO_2 and $y< 0$ defines a perovskite

Table 1.1

DEFECT NOTATIONS

A_A	Cation A on its normal lattice site
B_B	Cation B on its normal lattice site
O_O	Anion O on its normal site
$A_i^{\cdot\cdot}$	Divalent cation A on an interstitial site
$B_i^{\cdot\cdot\cdot\cdot}$	Tetravalent cation B on an interstitial site
V_O	Anion vacancy in normal O site
$V_O^{\cdot\cdot}$	Doubly ionized anion vacancy in normal O site
V_A	Cation vacancy in normal A site
$V_A^{\prime\prime}$	Doubly ionized cation vacancy in normal A site
V_B	Cation vacancy in normal B site
$V_B^{\prime\prime\prime\prime}$	Multiply (tetra) ionized cation vacancy in normal B site
$A_B^{\prime\prime}$	Cation A on normal B site
$B_A^{\cdot\cdot}$	Cation B on normal A site
n	Electron
P	Electron hole

containing excess AO.

Let

$$w = \frac{[O_i'']}{[O_i]+[O_o]} - \frac{[V_o^{\cdot\cdot}]}{[O_i]+[O_o]} \tag{1.9}$$

where w is the concentration of excess or deficit anions.

$w>0$ if $[O_i]>[V_o]$;

$w = 0$ indicates absence of excess or deficit anion.

The average number of anions in $\frac{1}{4}$ of the unit cell is $3(1-w)$, giving,

$$3(1-w) = 3+\alpha+2\beta \tag{1.10}$$

where,

$$\alpha = -2\beta-3w \tag{1.11}$$

From equation (1.8), for a small value of y, since $\alpha y \approx 0$,

$$1+\beta-\alpha = 1+y \tag{1.12}$$

From equations (1.11) and (1.12),

$$\alpha = \beta-y = -2\beta-3w \tag{1.13}$$

Hence,

$$\beta = -w+\frac{y}{3} \tag{1.14}$$

From equations (1.13) and (1.14),

$$\alpha = -w-\frac{2}{3}y \tag{1.15}$$

Using these relationships, it is easy to write mass and site balance equations for all ions in the perovskite.

Mass balance (concentration balance) :

For A atoms,

$$[A_A]+[A_B]+[A_i] = 1+\alpha = 1-w-\frac{2}{3}y \tag{1.16}$$

For B atoms,

$$[B_B]+[B_A]+[B_i] = 1+\beta = 1-w+\frac{y}{3} \tag{1.17}$$

For O atoms,

$$[O_o]+[O_i] = 3+\alpha+2\beta = 3-3w \tag{1.18}$$

Site balance :

Another set of balance equations is obtained by summing up all regular sites of the various sublattices of ions.

For A sites,

$$[A_A]+[B_A]+[V_A] = 1 \tag{1.19}$$

For B sites,

$$[B_B]+[A_B]+[V_B] = 1 \tag{1.20}$$

For O sites,

$$[O_o]+[V_o] = 3 \tag{1.21}$$

From equations (1.18) and (1.21),

$$w = \frac{[V_o]-[O_i]}{3} \tag{1.22}$$

From equations (1.16), (1.19) and (1.22),

$$[B_A]+[V_A]-[A_B]-[A_i]-\frac{1}{3}[[V_o]-[O_i]] = \frac{2}{3}y \tag{1.23}$$

From equations (1.17) and (1.20),

$$[B_A]+[B_i]-[A_B]-[V_B]+\frac{1}{3}[[V_o]-[O_i]] = \frac{y}{3} \qquad (1.24)$$

Equations (1.23) and (1.24) can be used to derive a catalogue of all possible types of disorder as shown in Table 1.2.

Since point defects often exist in thermodynamic equilibrium with the crystal lattice and the gas phase, relationships between the concentration of point defects and the thermodynamic independent variables can be derived. The dependence of the defect concentrations on the oxygen partial pressure in a ternary compound ABO_3 will be found under the assumption that concentrations and thermodynamic activities can be set equal, since point defects usually occur in very small concentrations. Only fully ionized defects are considered. Further, the changes in concentration of the various states of atomic and electronic disorder are considered as functions of oxygen partial pressure in a crystal ABO_3, in which the native imperfections are Schottky - Wagner type, with fully ionized anion and cation vacancies. Frenkel reaction involving interstitials is not considered, since the following analysis is applied in this study only to pure or doped $SrZrO_3$ systems, whose unit cells are close packed structures, with possible interstitial sites bounded by positive and negative ions.

Consider that at a certain temperature the only defects present are V_A , V_A'' V_B , V_B'''' , V_o , $V_o^{\bullet\bullet}$, n and p. The defect equations involved are :

$A_A+B_B+3O_o = V_A+V_B+3V_o+ABO_3$, giving,

$$[V_A][V_B][V_o]^3 = K_s \qquad (1.25)$$

and

$$[V_A''][V_B''''][V_o^{\bullet\bullet}]^3 = K_s' \qquad (1.26)$$

Table 1.2

a) DEFECT MODELS FOR $A_{1+\alpha}B_{1+\beta}O_{3+\alpha+2\beta}$

	$A_i^{\cdot\cdot}$	$B_i^{\cdot\cdot\cdot\cdot}$	V_A''	V_B''''	A_B''	$B_A^{\cdot\cdot}$	$V_O^{\cdot\cdot}$	O_i''
$A_i^{\cdot\cdot}$			$y \sim 0$	$y<0$	$y<0$			$y<0$
$B_i^{\cdot\cdot\cdot\cdot}$			$y>0$	$y \sim 0$	$y<0$			$y>0$
V_A''						$y>0$	$y>0$	
V_B''''						$y>0$	$y<0$	
A_B''						$y \sim 0$	$y<0$	
$B_A^{\cdot\cdot}$								$y>0$
$V_O^{\cdot\cdot}$								$y \sim 0$
O_i''								

b) DEFECT CONCENTRATION RELATIONSHIPS FOR CATIONIC DISORDER TYPES

$y \sim 0$	$A_i^{\cdot\cdot}=V_A''$	$B_i^{\cdot\cdot\cdot\cdot}=V_B''''$	$A_B''=B_A^{\cdot\cdot}$	$V_O^{\cdot\cdot}=O_i''$		
$y<0$	$A_i^{\cdot\cdot}=V_B''''$	$A_i^{\cdot\cdot}=A_B''$	$A_i^{\cdot\cdot}=O_i''$	$B_i^{\cdot\cdot\cdot\cdot}=A_B''$	$V_B''=V_O^{\cdot\cdot}$	$A_B''=V_O^{\cdot\cdot}$
$y>0$	$B_i^{\cdot\cdot\cdot\cdot}=V_A''$	$V_A''=B_A^{\cdot\cdot}$	$V_A''=V_O^{\cdot\cdot}$	$V_A''''=B_A^{\cdot\cdot}$	$B_A^{\cdot\cdot}=O_i''$	

$np = n + p$, giving,

$$[n][p] = K_i \tag{1.27}$$

$V_o = V_o^{\cdot\cdot} + 2n$, giving,

$$\frac{[V_o^{\cdot\cdot}][n]^2}{[V_o]} = K_{28} \tag{1.28}$$

$V_A = V_A'' + 2p$, giving,

$$\frac{[V_A''][p]^2}{[V_A]} = K_{29} \tag{1.29}$$

$V_B = V_B'''' + 4p$, giving,

$$\frac{[V_B''''][p]^4}{[V_B]} = K_{30} \tag{1.30}$$

$O_o = \frac{1}{2}O_2 + V_o$, giving,

$$[V_o]P_{O_2}^{\frac{1}{2}} = K_{31} \tag{1.31}$$

and

$\frac{3}{2}O_2 = 3O_o + V_A + V_B$, giving,

$$[V_A][V_B] = K_{32}P_{O_2}^{\frac{3}{2}}[V_A][V_B] = K_{32}P_{O_2}^{\frac{3}{2}} \tag{1.32}$$

With the assumption that $[V_A] = [V_B]$, from equation (1.32),

$$[V_A] = [V_B] = K_{32}P_{O_2}^{\frac{3}{4}} \tag{1.33}$$

The equilibrium constant K may be written as:

$$K = \exp\left[-\frac{\Delta G_F^0}{RT}\right] = \exp\left[-\frac{\Delta H_F^0}{RT} + \frac{\Delta S_F^0}{R}\right] \tag{1.34}$$

where ΔG_F^0 , ΔH_F^0 and ΔS_F^0 are the standard Gibbs free energy, enthalpy and entropy of formation for the reaction, respectively. Thus, each of the above defect reactions have thermodynamic formation terms associated with it.

The important criterion which must be fulfilled at all times is that pertaining to charge neutrality. The crystal must be electrically neutral at all times so that the formation of a charged defect of one sign is balanced by defects of the opposite sign. Thus, the electrical neutrality equation is :

$$[p]+2[V_o^{\cdot\cdot}] = [n]+2[V_A^{\prime\prime}]+4[V_B^{\prime\prime\prime\prime}] \tag{1.35}$$

When the concentration of particular defects are dominant, the above electrical neutrality condition may be separated into 4 cases:

For low P_{O_2} values, $[V_o^{\cdot\cdot}]$ is much greater than $[V_A^{\prime\prime}]$, $[V_B^{\prime\prime\prime\prime}]$ and [p]. Then the neutrality condition reduces to :

$$2[V_o^{\cdot\cdot}] \approx [n] \tag{1.36}$$

Similarly, for sufficiently large values of P_{O_2} , $[V_A^{\prime\prime}]$ and $[V_B^{\prime\prime\prime\prime}]$ are greater than $[V_o^{\cdot\cdot}]$ and [n]. Then, the neutrality condition is :

$$2[V_A^{\prime\prime}]+4[V_B^{\prime\prime\prime\prime}] \approx [p] \tag{1.37}$$

For intermediate P_{O_2} values, there are two possible approximate solutions, depending on the actual values of the equilibrium constants of the above reactions. These neutrality conditions can be either:

$$[n] \approx [p] \tag{1.38}$$

or,

$$[V_o^{\cdot\cdot}] \approx [V_A^{\prime\prime}]+2[V_B^{\prime\prime\prime\prime}] \tag{1.39}$$

Combining equations (1.25) - (1.34) and the four neutrality conditions, viz., equations (1.36) - (1.39), yields expressions for all defect concentrations as a functions of P_{O_2} . The calculated P_{O_2} dependence of the fully ionized defect concentrations of the ternary compound ABO_3 is given in Table 1.3. Figures 1.1 and 1.2 are the isothermal pressure dependence of various defect concentrations. The neutrality condition in the intermediate region is $[V_o^{\cdot\cdot}] \approx [V_A^{''}]+2[V_B^{''''}]$ in Figure 1.1 and $[n] \approx [p]$ in Figure 1.2.

1.3 Effect of Foreign Atoms in a Ternary Compound ABO_3

Small amounts of impurities can have pronounced effects on the conductivity of ionic crystals. The incorporation of foreign atoms may have a variety of consequences which depend on the base crystal, the foreign atoms and the site which the impurity atoms occupy in the lattice. The effects arising from the incorporation of a foreign atom are partly associated with the foreign atom and its particular state and partly with the electronic and atomic imperfections of the base crystal.

Foreign atoms may be incorporated at cation or anion lattic sites or at interstitial sites. The position occupied depends on the energy balance with factors such as chemical bonding, Van der Waal's forces, Born repulsion, etc., playing a role. The following discussion is concerned only with the incorporation of impurity atoms on the cation sublattice.

If a foreign atom is incorporated in a crystal, it may yield or trap electrons and thus take part in reactions involving electrons and holes. The extent to which it does so is determined by the energy needed for the reaction, that is, by the position of the level associated with the foreign atom relative to the energy bands of the base crystal. The position of the levels associated with substitutional foreign atoms depends to a large extent on the relative number of valence electrons, on the foreign atoms and on the lattice constituents which normally occupy this position. If the foreign atom has more valence electrons than the atom which is replaced, it may give off one or more of the excess electrons to

Table 1.3

P_{O_2} DEPENDENCE OF COMPLETELY IONIZED DEFECT CONCENTRATIONS IN THE TERNARY OXIDE ABO_3

Defect	$[n]=2[V_O^{\cdot\cdot}]$	$[V_O^{\cdot\cdot}]=[V_A^{''}]+2[V_B^{''''}]$	$[n]=[p]$	$[p]=2[V_A^{''}]+4[V_B^{''''}]$
[n]	-1/6	-1/4	0	-3/16
[p]	1/6	1/4	0	3/16
$[V_O^{\cdot\cdot}]$	-1/6	0	-1/2	-1/8
$[V_A^{''}]=[V_B^{''''}]$	1/4	0	3/4	3/16

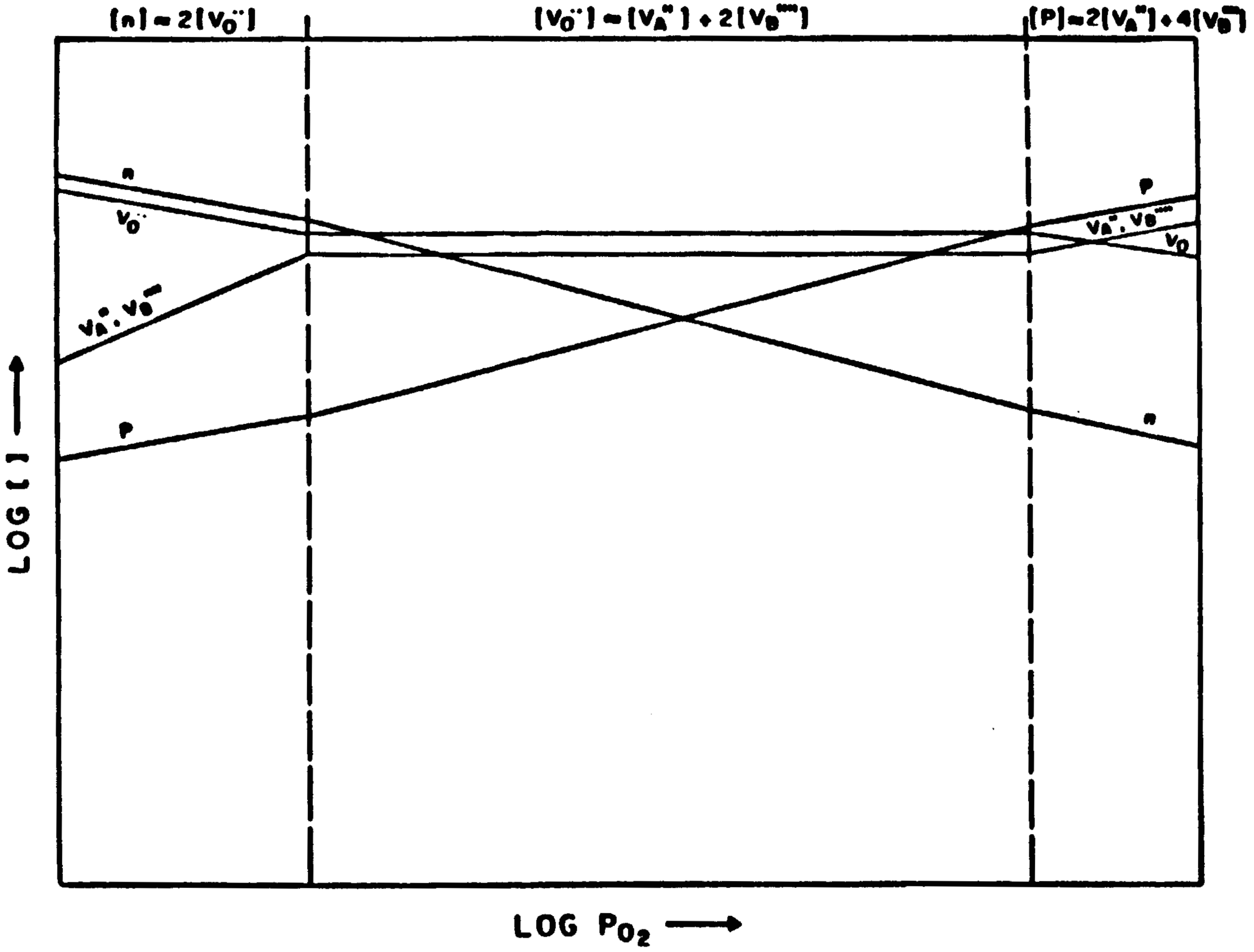

Figure 1-1: CALCULATED DEFECT CONCENTRATIONS VS. OXYGEN PRESSURE IN ABO_3 INTERMEDIATE NEUTRALITY CONDITION IS $[V_O^{\cdot\cdot}] = [V_A''] + 2[V_B'''']$

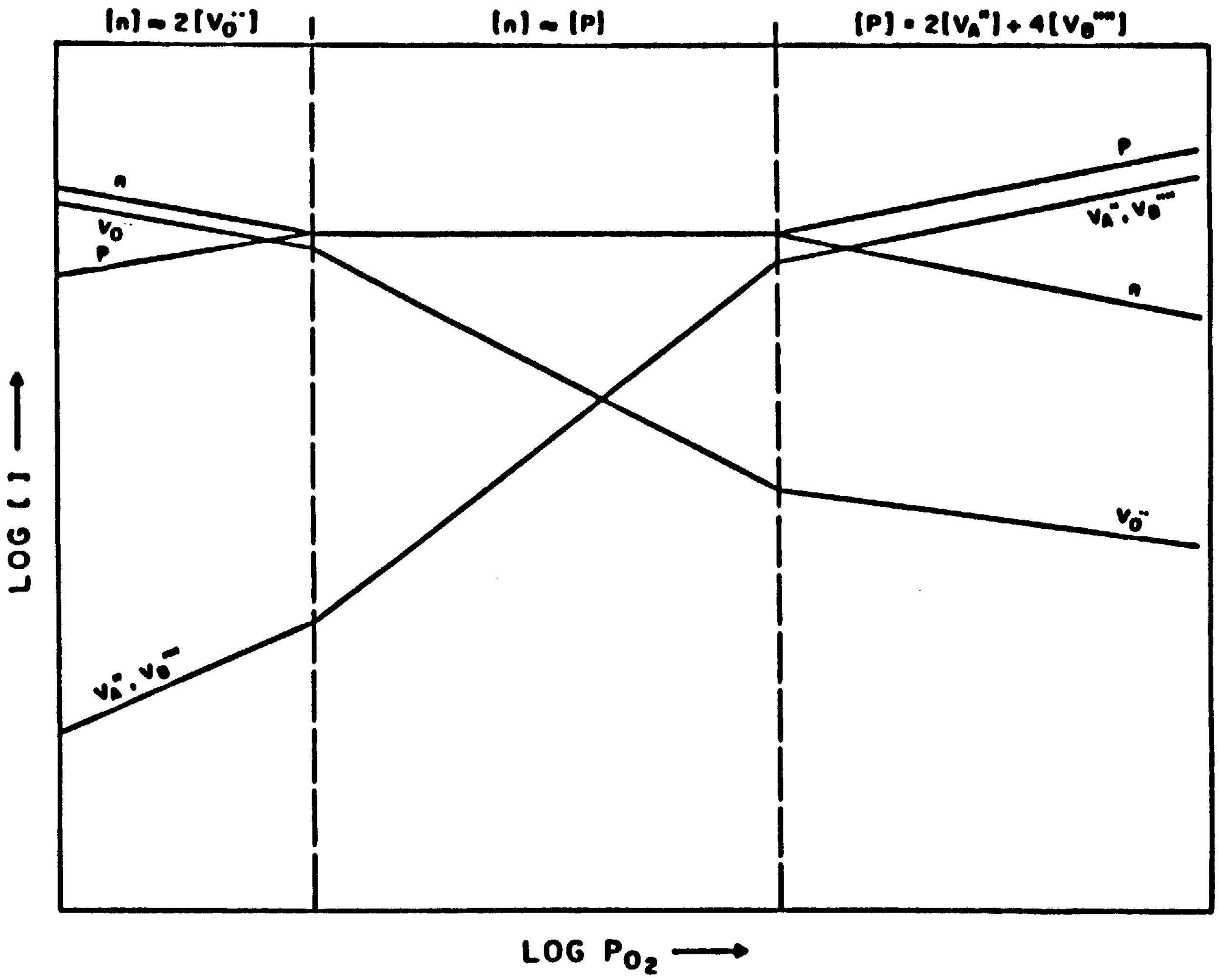

Figure 1-2: CALCULATED DEFECT CONCENTRATIONS VS. OXYGEN PRESSURE IN ABO_3
INTERMEDIATE NEUTRALITY CONDITION IS $[n] = [p]$

the conduction band. The tendency to bind additional electrons is often small and the atom is referred to as a donor. If, on the other hand, the foreign atom contains fewer valence electrons than the normal lattice constituent, it may bind extra electrons rather than release them and the atom is referred to as an acceptor.

Consider a perovskite ABO_3 in which a donor impurity is dissolved and assume that all the impurity atoms are completely ionized such that, $[I_m]_{total} = [I_m^{\cdot}] = constant$. The ionization equation involved is :

$[I_m] = [I_m^{\cdot}]+n$, giving,

$$K_{40} = \frac{[I_m^{\cdot}][n]}{[I_m]} \tag{1.40}$$

where $I_m^{\cdot}$ refers to an ionized donor impurity ion. If the concentration is sufficiently large, the electrical neutrality condition is changed due to the additional defect $I_m^{\cdot}$. Thus, a new electrical neutrality equation is obtained as follows :

$$[p]+2[V_o^{\cdot\cdot}]+[I_m^{\cdot}] = [n]+2[V_A^{''}]+4[V_B^{''''}] \tag{1.41}$$

The various possibilities for the sequence of reduced neutrality conditions are :

$[n] \approx 2[V_o^{\cdot\cdot}]$, $[n] \approx [I_m^{\cdot}]$,

$[I_m^{\cdot}] \approx 2[V_A^{''}]+4[V_B^{''''}]$ and

$[p] \approx 2[V_A^{''}]+4[V_B^{''''}]$,

or

$[n] \approx 2[V_o^{\cdot\cdot}]$, $[n] \approx [p]$ and

$[p] \approx 2[V_A^{''}]+4[V_B^{''''}]$.

The calculated P_{O_2} dependence of the defect concentrations is shown in Table 1.4. The plot of the variation of log defect concentrations vs. log P_{O_2} is

Table 1.4

P_{O_2} DEPENDENCE OF DEFECT CONCENTRATIONS IN THE DONOR-DOPED ABO_3

Defect	$[n]=2[V_O^{\cdot\cdot}]$	$[n] = [I_m^{\cdot}]$	$[I_m^{\cdot}]=2[V_A'']+4[V_B'''']$	$[p]= 2[V_A'' +4[V_B'''']$
$[n]$	-1/6	0	-1/4	-3/16
$[p]$	1/6	0	1/4	3/16
$[V_O^{\cdot\cdot}]$	-1/6	-1/2	0	-1/8
$[I_m^{\cdot}]$	0	0	0	0
$[V_A'' =[V_B'''']$	1/4	3/4	0	3/16

given in Figure 1.3. Only the case where Schottky reaction dominates is considered since the emphasis is on the effect of impurities.

If an acceptor impurity is dissolved in the ABO_3 system, then the ionization reaction yields :

$$\frac{[I_m'][p]}{[I_m]} = K_{42} \tag{1.42}$$

where I_m' and I_m refer respectively to an ionized impurity ion and an impurity ion on a normal cation sublattice site. The electrical neutrality equation in this case is :

$$[p]+2[V_o^{\cdot\cdot}] = [n]+[I_m']+2[V_A'']+4[V_B''''] \tag{1.43}$$

The possibilities for the sequence of the charge neutrality conditions are:

$[n] \approx 2[V_o^{\cdot\cdot}]$, $2[V_o^{\cdot\cdot}] \approx [I_m']$,

$[p] \approx [I_m']$ and $[p] \approx 2[V_A'']+4[V_B'''']$,

or

$[n] \approx 2[V_o^{\cdot\cdot}]$, $[n] \approx [p]$,

$[p] \approx [I_m']$ and $[p] \approx 2[V_A'']+4[V_B'''']$.

The resultant log defect concentrations vs. log P_{O_2} diagram is shown in Figure 1.4 and the slopes of the various curves are listed in Table 1.5. As before, only the situation where the Schottky reaction dominates is considered.

The stoichiometry indicated from a n-p transition for the pure ABO_3 crystal illustrated in Figures 1.1 and 1.2 is shifted to lower oxygen partial pressures with an acceptor impurity addition and to higher oxygen pressures when a donor impurity is added. The operative ranges (limiting widths) of the various electrical neutrality conditions and their positions as functions of P_{O_2} are determined from the actual values of the various equilibrium constants for disorders in the

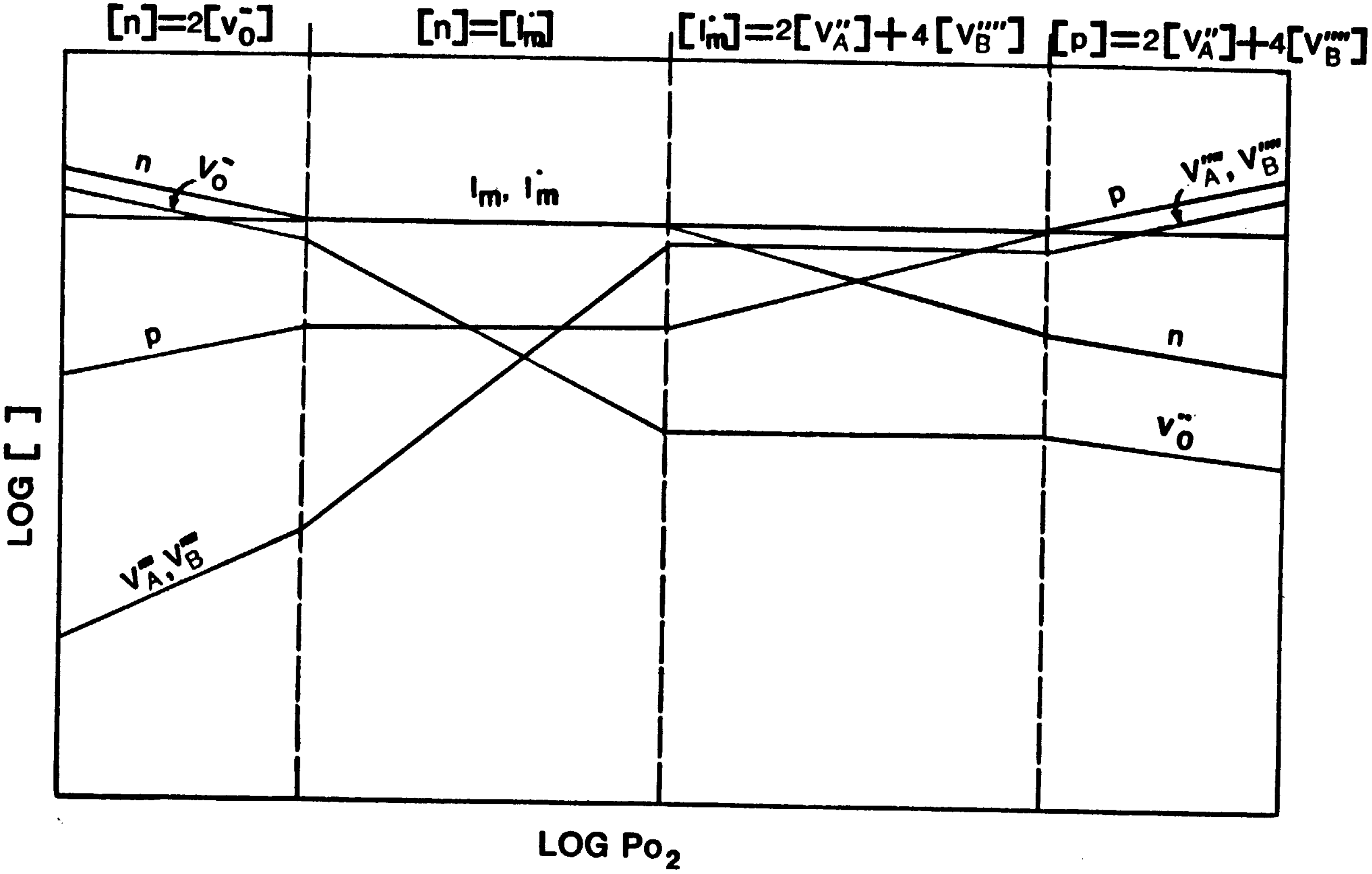

Figure 1.3: CALCULATED DEFECT CONCENTRATIONS VS. OXYGEN PRESSURE FOR DONOR-DOPED ABO_3

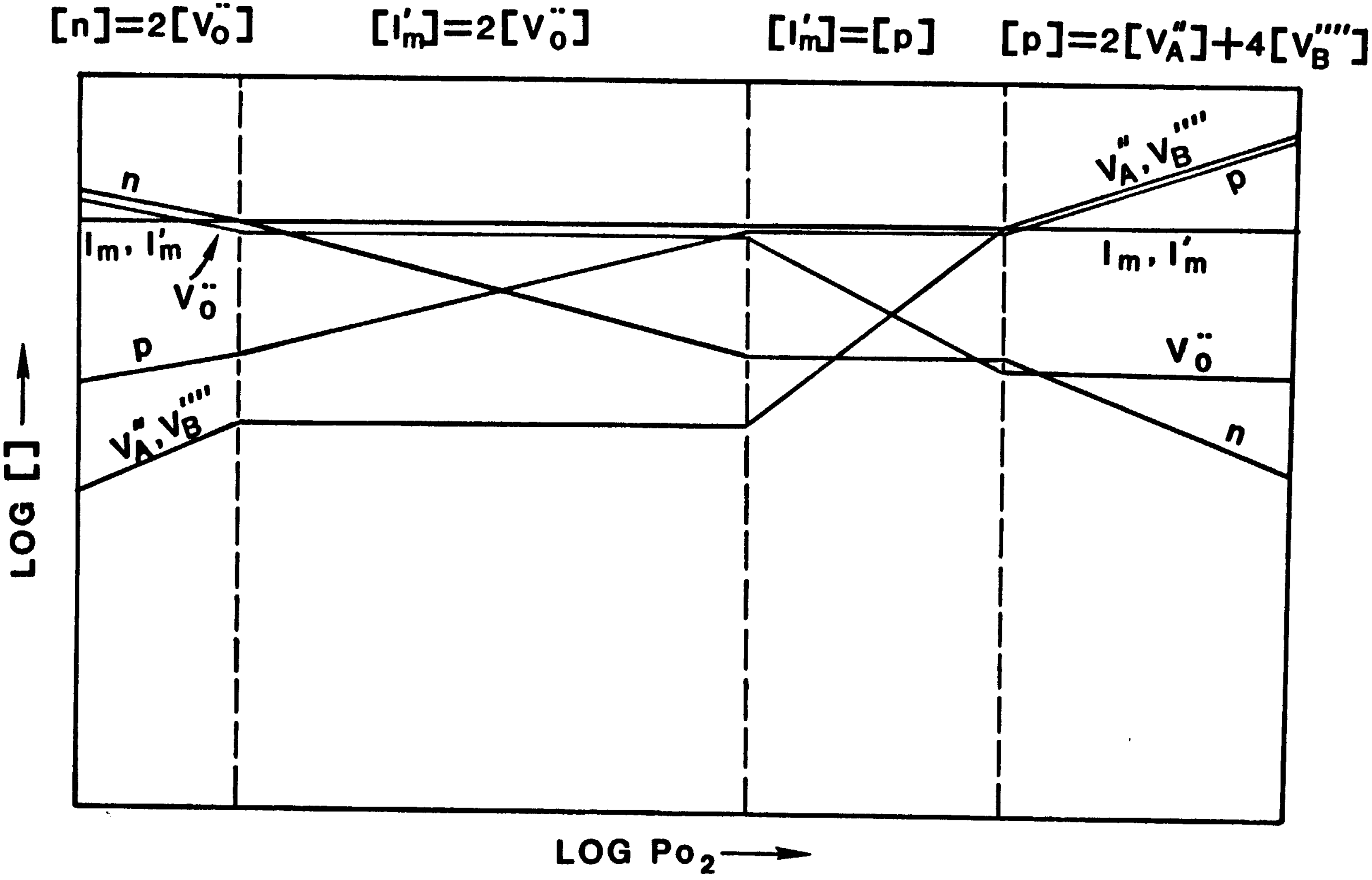

Figure 1.4: CALCULATED DEFECT CONCENTRATION VS. OXYGEN PRESSURE FOR ACCEPTOR-DOPED ABO_3

Table 1.5

P_{O_2} DEPENDENCE OF DEFECT CONCENTRATIONS IN THE ACCEPTOR-DOPED ABO_3

Defect	$[n]=2[V_O^{\cdot\cdot}]$	$[I_m']=2[V_O^{\cdot\cdot}]$	$[I_m']=[p]$	$[p]=2[V_A'']+4[V_B'''']$
$[n]$	-1/6	-1/4	0	-3/16
$[p]$	1/6	1/4	0	3/16
$[V_O^{\cdot\cdot}]$	-1/6	0	-1/2	0
$[I_m']$	0	0	0	0
$[V_A'']=[V_B'''']$	1/4	0	3/4	3/16

crystal.

For sufficiently large amounts of impurity, a region in which the electron concentration is independent of P_{O_2} is expected, as shown in Figures 1.3 and 1.4.

1.4 Diffusivity

The electrical conductivity in many oxides is proportional to the concentration of point defects. Since the point defects are often the mobile species in the diffusion process, it is possible to use electrical conductivity to follow the kinetics of interdiffusion in oxides. In fact, this has been done by several investigators (9-12).

Consider a bar shaped sample of dimensions :

$-a < x < a$, $-b < y < b$, $-c < z < c$,

in equilibrium with a gas phase of known composition. From the work of Newman (13), unidimensional diffusion flow in this sample can be expressed as :

$$\frac{\partial C}{\partial t} = D(\frac{\partial^2 C}{\partial x^2}) \quad (1.44)$$

where C is the concentration of the diffusing species at time t.

For 2-dimensional flow, the above equation can be rewritten as :

$$\frac{\partial C}{\partial t} = D(\frac{\partial^2 C}{\partial x^2} + \frac{\partial^2 C}{\partial y^2}) \quad (1.45)$$

Similarly, for diffusion in three dimensions :

$$\frac{\partial C}{\partial t} = D(\frac{\partial^2 C}{\partial x^2} + \frac{\partial^2 C}{\partial y^2} + \frac{\partial^2 C}{\partial z^2}) \quad (1.46)$$

The following Fourier series represent the solutions for the above equations :

For 1-dimensional flow:

$$\frac{C-C_1}{C_0-C_1} = \frac{4}{\pi}\left[\cos\left(\frac{\pi x}{2a}\right)\exp\left(-Dt\left(\frac{\pi}{2a}\right)^2\right) - \frac{1}{3}\cos\left(\frac{3\pi x}{2a}\right)\exp\left(-9Dt\left(\frac{\pi}{2a}\right)^2\right) + \frac{1}{5}\cos\left(\frac{5\pi x}{2a}\right)\exp\left(-25Dt\left(\frac{\pi}{2a}\right)^2\right) - \ldots\ldots\right] \tag{1.47}$$

or,

$$\frac{C-C_1}{C_0-C_1} = Series A \tag{1.48}$$

Similarly, for 2-dimensional flow:

$$\frac{C-C_1}{C_0-C_1} = (Series A)(Series B) \tag{1.49}$$

and, for 3-dimensional flow:

$$\frac{C-C_1}{C_0-C_1} = (Series A)(Series B)(Series C) \tag{1.50}$$

Series B and C are similar to Series A except that y and z are substituted for x, and 2b and 2c for 2a, respectively.

Now, conductivity, σ_0 , of this sample is proportional to the initial uniform concentration of defects, C_0 , within this sample. At time zero, through a step function change in the composition of the gas phase, the defect concentration is changed to C_f and the sample approaches a new equilibrium conductivity, σ_f , proportional to C_f , as t approaches ∞ .

Campbell, Kass and O'Keefe (14) calculated the quantity $\Sigma = \frac{\bar{\sigma}(t)-\sigma_f}{\sigma_0-\sigma_f}$ and compared it to $\frac{\bar{C}(t)-C_f}{C_0-C_f}$, where $\sigma(t)$ and C(t) equal the conductivity and the corresponding defect concentration at any time t (for t< ∞), as a function of $\frac{Dt}{C^2}$ for various shapes of samples and values of $\frac{\sigma_0}{\sigma_f}$. In general, they found that both quantities vary identically with $\frac{c}{b}$ (or $\frac{c}{a}$) ratios greater than unity (long, thin samples) and that for $\frac{\sigma_0}{\sigma_f}$ ratios not very different from unity, these two quantities are the same functions of $\frac{Dt}{c^2}$. In view of the above analysis, the series solutions of Newman, viz., equations (1.47)-(1.50) can be used to obtain diffusion coefficients from conductivity data for appropriately chosen sample shapes.

2. REVIEW OF RELATED WORK

2.1 Solubility Limit of La in $SrZrO_3$

The solubility limit of La in $SrZrO_3$ has not been studied in the past. However, the solid solution formation tendencies of La in certain other perovskite systems have been investigated elsewhere. Haertling and Land (15) indicated that La is only very slightly soluble at the $PbZrO_3$ end of the PLZT (La-substituted lead titanate-zirconate) phase diagram. Both $La_2Zr_2O_7$ and $PbZrO_3$ exist in a region extending from $PbZrO_3$ to PLZT with a Zr/Ti ratio of 90/10 (at.%). At ratios less than 90/10 and upto at least 30 at.% La, only a PLZT solid solution exists. Based on x-ray analysis, they reported that the unit cell volume decreases linearly as a function of increasing La content. Schulze et al (16) determined the solubility limit of La in PLZT using the disappearing-phase method. They observed only limited solubility for La towards the $PbZrO_3$ end (solubility increasing with decreasing Zr/Ti ratio), with cubic $La_2Zr_2O_7$ precipitation occurring beyond the solubility limit. However, towards the $PbTiO_3$ end, they observed a much higher solubility limit. In a somewhat similar system, $PbZrO_3$ - $PbTiO_3$ - $LaFeO_3$, Ikeda and Okano (17,18) found that at least 20 mole% $LaFeO_3$ enters into solid solution with lead zirconate-titanate. A similar study of the same system by Berlincourt (19) essentially substantiated the findings of Ikeda and Okano. Besides altering the optical transparency characteristics, the results of these investigations are similar to those obtained by introducing La alone into solid solution with lead zirconate-titanate. In another study of the PLZT system, Hardtl and Hennings (20) reported that single-phase perovskites of composition $Pb_{1-x}La_x[(Ti_{1-y}Zr_y)_{1-x/4}]O_3$ could not be produced and attempts to do so always result in second phases with coexisting A-site and B-site vacancies. While these results contradict the earlier ones in decreasing Zr/Ti ranges at the Zr rich end, they still point to almost negligible solubility of La in $PbZrO_3$

In all these studies, the firing temperature was above 1373 K. Sasamoto et al (21) investigated the system $La(Fe_{0.5}Cr_{0.5})O_3-Sr(Fe_{0.5}Cr_{0.5})O_3-SrZrO_3$. Through x-ray powder diffractometry, they studied the change in lattice constant for a series of compounds $(La_{1-x}Sr_x)(Fe_{0.5}Cr_{0.5})O_3-SrZrO_3$ and reported that the lattice parameter decreases with increasing Sr content (decreasing La content). The solubility characteristics of La in other simple perovskites such as $BaTiO_3$ and $SrTiO_3$ have also been studied elsewhere (22-27). Eror and Smyth (22) have reported that up to 20 at.% Ba may be substituted by La to retain a single phase fully oxidized material on the basis that no second phases are observed either optically or through x-ray studies. Bouwma et al (23) reported that a sample of composition $La_{0.35}Sr_{0.65}TiO_3$ and a large cation to small cation ratio of unity, consists of two or more phases, one of which is a perovskite phase. They inferred that this composition lies outside the perovskite homogeneity range. The existence of a perovskite (ABO_3) phase of composition $Sr_{1-1.5x}La_xTiO_3$ in the ternary system $SrO-TiO_2-La_2O_3$ has been reported by Tien and Hummel (24). In all their samples, the large cation to small cation ratio was less than unity. In a similar study, Balachandran and Eror (25) reported that a single phase cubic perovskite type solid solution is obtained for all compositions containing upto 40 at.% La in $SrTiO_3$ with $La_2Ti_2O_7$ precipitating at higher La concentrations. On the contrary, Tofield and Scott (26) reported that it is not possible to obtain single phase materials of composition $Sr_{0.8}La_{0.2}TiO_{3.0-3.1}$, based on the observation of La_2O_3 lines in the x-ray patterns of their compounds.

2.2 Electrical Conductivity of Undoped and Doped $SrZrO_3$

The studies of electrical properties and conduction mechanisms of pure and La-doped $SrZrO_3$ over a range of temperature and partial pressure of oxygen are lacking. The few investigations on electrical conductivity measurements were carried out at ambient P_{O_2}, using undoped $SrZrO_3$ only. Pivovar and Tolstaya-Belik (28) measured the electrical conductivity of $SrZrO_3$ and $SrHfO_3$ by AC (2500 Hz) and DC two-probe methods in argon at 1400 - 2600 K. For $SrZrO_3$ samples with porosities of 11-16 %, they obtained activation energy values through log σ vs. 1/T curves, of 44 Kcal/mole at 1400 - 2000 K, 64 Kcal/mole at 2000 - 2300 K and 116 Kcal/mole at 2300 - 2600 K, while for samples with porosities of 24-26 %, they obtained values of 48.5 Kcal/mole at 1400 - 2000 K and 90 Kcal/mole at 2000 - 2600 K. When these results are compared with the work of Anthony et al (29), the conductivity values differ by about an order of magnitude. Pivovar and Tolstaya-Belik (28) attributed this to differences in sample preparation techniques. Some electrical conductivity studies for $SrZrO_3$ were performed as a function of temperature and P_{O_2} (30-33). However, in these cases P_{O_2} was varied only over six decades. Longo and Ricciardiello (30,31) investigated the electrical conductivity of ABO_3-type perovskites and their solid solutions (A = Ca, Sr, Ba; B = Ti, Zr, Ce). They measured the electrical conductivity in the temperature range of 1073-1473 K, in air and also as a function of P_{O_2} in the range of 10^0–5×10^{-6} atm., with the temperature fixed at 1473 K. They concluded that the logarithm of electrical conductivity of these ABO_3 perovskites is a linear function of the reciprocal of absolute temperature. They also inferred that all the compounds examined are primarily electronic semiconductors. The titanates and their solid solutions are n-type semiconductors, and the zirconates and cerates and the corresponding solid solutions are p-type semiconductors. In a related study, Longo and Ricciardiello (32) determined the electrical conductivity for the same class of ABO_3 perovskites and analysed the effect of structure on conduction mechanism through activation energy measurements. Anthony and Foex (33) investigated the electrical properties of $SrZrO_3$ as a function of stoichiometry. They found that conductivity is a function of ZrO_2/ SrO ratio, but the dependence is less pronounced at higher temperatures. From their results, they inferred that conduction is principally due to thermal agitation which causes defects in the crystal lattice and hence, the more perfect the lattice, the greater the energy required for the formation of defects, with these defects appearing only at high temperature. The electrical characteristics of $CaZrO_3-SrZrO_3$ solid solution mixtures were also studied in the temperature range of 1073-1473 K and P_{O_2} range of 10^0 - 5×10^{-6} atm. (34). All compositions were found to exhibit only p-type electronic conductivity. Further, the enthalpy of the conduction reaction was found to be a function of P_{O_2}, with the mean value reported as 2.65-2.85 eV. The same investigators also studied the ternary system $CaZrO_3-SrZrO_3-BaZrO_3$ (35). In addition to exhibiting p-type conductivity, these ternary solid solutions were all found to yield superior conductivity values than either the pure compounds or the binary solid solutions. Frederikse and Hesler (36) studied the electrical conductivity of Ce-doped and Ti-Ta-doped $SrZrO_3$. In both cases, they demonstrated that conductivity is a strong function of temperature in the range of 1423 K-1923 K, while being virtually independent of frequency (AC measurements performed at 100 Hz duplicated DC data within experimental error) and oxygen pressure, at the three pressures examined. Based on this, they suggested that the conduction mechanism is electronic rather than ionic and the activation energies (4 eV and 3.6 eV for Ce-doped and Ti-Ta-doped samples respectively) correspond to that for intrinsic electron excitation across the energy gap of the mixed crystals. The conductivity value of these samples at elevated temperature was reported as 0.1 $(ohm\ cm)^{-1}$, an acceptable value for an MHD-electrode material. However, the very steep temperature dependence implies that these compounds have very large resistivities at lower temperatures. Carlsson (37) studied the high temperature phase transition of $SrZrO_3$, as well as the resistivity and dielectric properties. His resistivity data indicated that at temperatures above 1273 K, $SrZrO_3$ behaves as a semiconductor in the intrinsic range, with a band gap of about 2.1 eV. While Carlsson (37) noted a phase transition (tetragonal to cubic) at 1443 K , no anomaly was detected in the conductivity behavior at that temperature. Budim and Kozyreva (38) used the method of diffuse reflection spectra to determine the forbidden band width of $SrZrO_3$ (~2.9 eV). They concluded that the band gap is an inverse function of the interatomic distance (Zr-O distance), that is, increasing bond strength.

2.3 Diffusion Studies in Perovskites

Little published literature is available on the diffusion characteristics of $SrZrO_3$. However, a brief survey of the work on some analogous perovskites is presented here and the diffusion experiments in $SrZrO_3$ in this study are based on the results of these investigations. The diffusion of point defects was investigated in $SrZrO_3$ by Walters and Grace (11). Single crystals of $SrZrO_3$ were equilibrated with damp hydrogen of fixed P_{H_2O}/P_{H_2} ratio. Steps in the P_{H_2O}/P_{H_2} ratio were subsequently imposed over the samples and the transient electrical conductivity was measured until a new equilibrium was attained. The diffusion coefficient of oxygen vacancies was then obtained from the analysis of the transient conductivity measurements based on a method proposed by Dunwald and Wagner (39). Similar experiments were conducted by George and Grace (12) on $CaTiO_3$. The enthalpy of motion reported by these investigators for oxygen vacancy diffusion in $CaTiO_3$ is roughly twice that measured for $SrTiO_3$ by Walters and Grace (11). Also, unlike Walters and Grace, they reported a P_{H_2O}/P_{H_2} dependence of the diffusion coefficient which is not significantly affected by oxidizing or reducing conditions. The technique of using transient conductivity to obtain the chemical diffusion coefficient of point defects was also adopted successfully by other investigators (10,40,41).

Formation of mixed titanate layers by solid-solution reactions between single crystal $SrTiO_3$ and a second compound of the ABO_3 type was studied in a series of diffusion experiments (42) based on concentration vs. distance curves obtained from electron microprobe measurements. Interdiffusion was observed in the system $(Sr,Ba)TiO_3$, $(Sr,Ca)TiO_3$ and $Sr(Ti,Zr)O_3$. The corresponding diffusion coefficients as functions of concentration were calculated using the Boltzmann-Matano method. Interdiffusion was not observed in the $(Sr,Pb)TiO_3$, $(Sr,La)TiO_3$ and $Sr(Ti,Nb)O_3$ systems in the temperature range of study. However, in $(Sr,Ca)TiO_3$ and $(Sr,Ba)TiO_3$ system , interdiffusion of A-site atoms was observed while the Ti did not diffuse and similarly in $Sr(Ti,Zr)O_3$ system, interdiffusion of B-site atoms was noted while Sr concentration remained at a constant value.

2.4 Structure and Raman Spectra of Perovskites

The close relationship between the ferroelectric effect and lattice dynamics for the perovskite-structured materials has led to extensive investigation of their infrared and Raman spectra. Vibrational spectra have been obtained and interpreted for single crystals and solid solutions of perovskite titanates, tantalates, and niobates. However, very little work has been done with the perovskite zirconates. A few papers have been published on the infrared absorption and reflection spectra of some powdered zirconates (43-45) but only limited Raman data is available in the literature. Pasto and Condrate (46,47) obtained and interpreted the Raman spectra of powders or single crystals of several perovskite zirconates ($BaZrO_3$, $SrZrO_3$, $CaZrO_3$ and $PbZrO_3$). They also studied the perturbations on the Raman spectra of zirconate powders due to impurities and the temperature dependence of the Raman spectra of single crystal

$PbZrO_3$.

The ideal perovskite structure is cubic. Divalent A-cations are placed in the cube corners with B-cations at body centers, and O-anions at face centers. Through x-ray studies, Smith and Welch (48) reported that $SrZrO_3$ is a cubic form of deformed perovskite structure with eight formula units per cell. Roth (49) has classified perovskites on the basis of the ionic radii of A and B cations and according to his data, $SrZrO_3$ possesses an orthorhombic structure. The orthorhombic nature of $SrZrO_3$ was also verified by Swanson et al (50). Further work by Carlsson (37,51) supported this view. In addition, he also determined that there were two high temperature tetragonal phases, the first appearing around 973 K with a c/a ratio <1 and the second around 1103 K with a c/a ratio >1. He also found that at 1443 K, the tetragonal form transforms to a cubic one. On the basis of x-ray diffractometry results, the same investigator proposed that the true unit cells of $SrZrO_3$ in the high temperature phases are multiples of the simple small-cell perovskite, with a unit cell of the high temperature phase made up of eight formula units, and the axes of the true unit cell are twice the cell-edges of the ideal small-cell. Ahtee et al (52) studied the structure of $SrZrO_3$ at room temperature using neutron powder-profile refinement technique. They found that $SrZrO_3$ possesses an orthorhombic structure, with the space group being represented by P_{bnm}. The high temperature structure of $SrZrO_3$ was also determined through the same neutron powder profile refinement technique (53), and the phase transitions were described by the condensation of soft vibrational modes. These results were similar to those obtained by Carlsson (37,51), except that the tetragonal phase was seen only at 1173 K.

Since only limited work has been done on $SrZrO_3$, the data available in other similar perovskites are examined here briefly, to serve as a guideline. Cowley (54) analysed the lattice dynamics of $SrTiO_3$ through neutron diffraction and obtained the energy vs. wave vector dispersion curves of the vibrational branches in $SrTiO_3$. The lattice dynamics of $SrTiO_3$ have also been studied by infrared techniques. Barker and Tinkham (55) as well as Spitzer et al (56) measured the energy of three active TO modes and reported that the energy of the ferroelectric mode decreases with a decrease in temperature. The Raman spectra of $SrTiO_3$ was also studied extensively by Narayanan and Vedam (57) with conventional light sources. They obtained seven Raman lines, six of which were interpreted as the first order spectrum arising from a small deviation of cubic $SrTiO_3$ from its idealized symmetry. Nelson and Skinner (58) studied the Raman spectra of $SrTiO_3$ as a function of temperature and impurity. At room temperature, they found the spectra to be entirely second order and on the basis of the Raman scattering characteristics they reported that pure and impure samples undergo different phase transitions as the temperature is reduced. Perry et al (59) used the temperature dependence of the second-order Raman spectra of $SrTiO_3$ and $KTiO_3$, to differentiate between possible combination and summation processes and difference processes which contribute to the multiphonon spectra of these materials. Prater et al (60) studied the impurity induced ferroelectric phase transition in Li-doped $KTaO_3$ and reported that the pressure of Li impurities stiffens the TO branch at the zone center and that the ferroelectric phase results from an order-disorder transition of the off-center Li ions. Similar studies have been conducted on $BaTiO_3$ (61,62). In this system, a strong temperature dependent vibration was observed and was interpreted as the longitudinal mode associated with the low frequency transverse feroelectric soft mode (61). The temperature dependence of the A_1 (TO) broad phonon linewidth was accounted for by assuming a model where the Ti ions are located off the center of the unit cell and tunnel through a double well in the direction of the ferroelectric axes (62). Recently, the impurity effects on the Raman spectra of

$Sr_{0.6}Ba_{0.4}Nb_2O_6$ were also studied by Kuroda and Kubata (63). They observed that the degree of the crystal disorder is enhanced by doping rare earth ions (Pr^{+3} and Nd^{+3}), especially along the x-y plane compared with that along the polar c-axis.

3. OBJECTIVES

As mentioned earlier, studies on the electrical and diffusion properties and Raman spectral characteristics of pure $SrZrO_3$ and La-doped $SrZrO_3$ are sparse, eventhough these compounds are finding increasing use in many applications. Hence, this investigation was undertaken to furnish the above data for these compounds and to provide a comprehensive understanding of the behavior of these compounds. First, the solubility limit of La in $SrZrO_3$ was determined to establish the range of homogeneity. Evaluation of electrical conductivity and other properties were limited to this homogeneous perovskite range. Electrical conductivity studies were carried out for both pure and La-doped $SrZrO_3$ over a wide range of oxygen partial pressure and temperature. Studies of this nature help in understanding the disorder and the defect structure within these compounds in addition to establishing the regions of ionic and electronic compensations. Transient conductivity measurements were also performed to obtain the chemical diffusion coefficient of the major point defects. From equilibrium conductivity studies, the enthalpy of formation of the major point defects was obtained and from the transient conductivity experiments, the enthalpy of motion of these defects was evaluated. Separate diffusion studies were also attempted using diffusion couples and the interdiffusion coefficients of the major cation species were compared. The underlying mechanisms involving electronic defects, impurities, vacancies of anions or cations can be directly verified through such chemical diffusion and interdiffusion studies. Raman studies were carried out at various temperatures for both pure and La-doped samples and the spectra interpreted on the basis of factor-group analysis. These Raman studies were conducted to provide valuable insight into the structure, impurity and disorder effects of these perovskites.

4. EXPERIMENTAL PROCEDURE

4.1 Sample Preparation

A liquid mix technique was used to prepare thermodynamically defined compounds in order to make meaningful analysis of electronic and ionic disorder phenomena (22,64,65). To define a ternary ABO_3 system thermodynamically, oxygen partial pressure, temperature and the ratio of the cations (or the activity of one of the cations) must all be fixed (66). For non-volatile cations, through the liquid mix technique, the stoichiometries of the major and minor constituents can be controlled to within a few parts per million precision (<0.001%).

Mechanical communition involved in the conventional method of preparing powder formulations to achieve homogeneity and intimacy of the reacting species, introduces contaminates which affect the properties and yield inconsistent results. Also, the high temperature calcination necessary to complete the diffusion controlled solid state reactions promotes crystallite growth and in general, yields poorly dispersed oxides. Conventional evaporation techniques also have limitations. The high temperature and the high vacuum required to vaporize the oxides lead to variations in oxidation states and contamination from vapors. Pyrolysis of precipitation or hydroxides or mixed salts is another method of preparing mixed oxides (67,68), but, again, the use of this method is limited by stoichiometric requirements and lack of homogeneity due to compositional changes in the liquid medium during the deposition of the solid phase (65).

The liquid mix technique suffers from none of the limitations observed in the above methods. The purity of the final compound can be as high as that of the starting materials and the thorough intermixing leads to homogeneity on an atomic scale. The final particle size can be of the order of a few hundred angstroms. In this method, the individual cations are complexed in separate weak organic acid solutions or available in salts that are soluble in the weak organic acid solutions. The respective cation concentrations in the individual solutions or soluble salts are gravimetrically analyzed to better than 0.001% accuracy, assuming intermixing of the cations on an atomic scale in the liquid state. The mixed solutions are evaporated to a rigid polymeric state without any precipitation. The resulting uniformly colored transparent glass is then calcined at relatively low temperatures to obtain a homogeneous single phase oxide of precise stoichiometry and particle size of a few hundred angstroms. Normally, solutions of cations complexed in an ethylene glycol-citric acid solvent are used to ensure that the cation solutions are stable with respect to time at room temperature (absence of precipitation upon storage) and also stable when mixed together and heated near the boiling point of the solvent.

Samples were prepared by dissolving appropriate amounts of $Zr(CO_3)_2$ (Electronic Space Product, Inc., spec. pure), $SrCO_3$ (Johnson Matthey Corp., spec. pure) and $La_2(CO_3)_3$ (Rare-Earth Division, spec. pure) in an ethylene glycol-citric acid solution. The preparation stoichiometry was $Sr_{1-x}La_xZrO_3$. The mixed solutions were evaporated for approximately five days, to a rigid polymeric state as revealed by the formation of a uniformly colored transparent glass and then calcined at 1023 K in an oxidizing atmosphere for a period of 24 hrs.

4.2 Gas System

The gas train has been described in detail elsewhere (69,70). Oxygen partial pressure over the pressure range of 10^0-10^{-4} atm. was achieved by mixing argon and oxygen in required ratios. Lower P_{O_2} values were obtained by mixing appropriate ratios of carbon dioxide and carbon monoxide. Commercial tank gases of the following grades were employed in this investigation: carbon dioxide-grade 2.8 and carbon monoxide-grade 2.3. For oxygen, tank gases of various argon-oxygen mixtures with analysis for oxygen were employed. As shown in Figure 4.1, oxygen and argon-oxygen mixtures were passed through successive tubes containing magnesium perchlorate, ascarite and magnesium perchlorate. Carbon dioxide was passed through successive tubes containing drierite, copper turnings at 723 K and drierite. Carbon monoxide was successively passed through tubes containing magnesium perchlorate, ascarite and magnesium perchlorate. Magnesium perchlorate and drierite were employed to remove moisture. Copper turnings at 723 K were used to remove oxygen and ascarite was used to remove carbon dioxide.

Conventional manometric flow meters using capillary constructions were used to measure the gas flow rates. Adjustment of the level of the fluid (di-butyl phthalate) in the gas blow-off column determined the pressure drop across the capillary which was read from the manometer. The flow rates of all gases were obtained from the calibration curves of the flow rate vs. pressure drop. The calibration curves were obtained by measuring the displacement of a bubble interface in a graduated burette. For each selected value of P_{O_2}, the flow rate of the gas mixture (CO-CO_2) was set at a particular ratio and these gases were passed through a mixing chamber of glass beads to insure a completely uniform mixing before entering the furnace. These mixed gases were then introduced at the bottom of the vertical furnace reaction tube assembly from which they exited through a stop-cock and a di-butyl phthalate bubbler, at the top.

As mentioned earlier, low oxygen partial pressures were obtained by mixing various ratios of carbon dioxide and carbon monoxide. Each P_{O_2} value was fixed by defining the ratio of CO and CO_2. The reaction involved in obtaining the P_{O_2} value is :

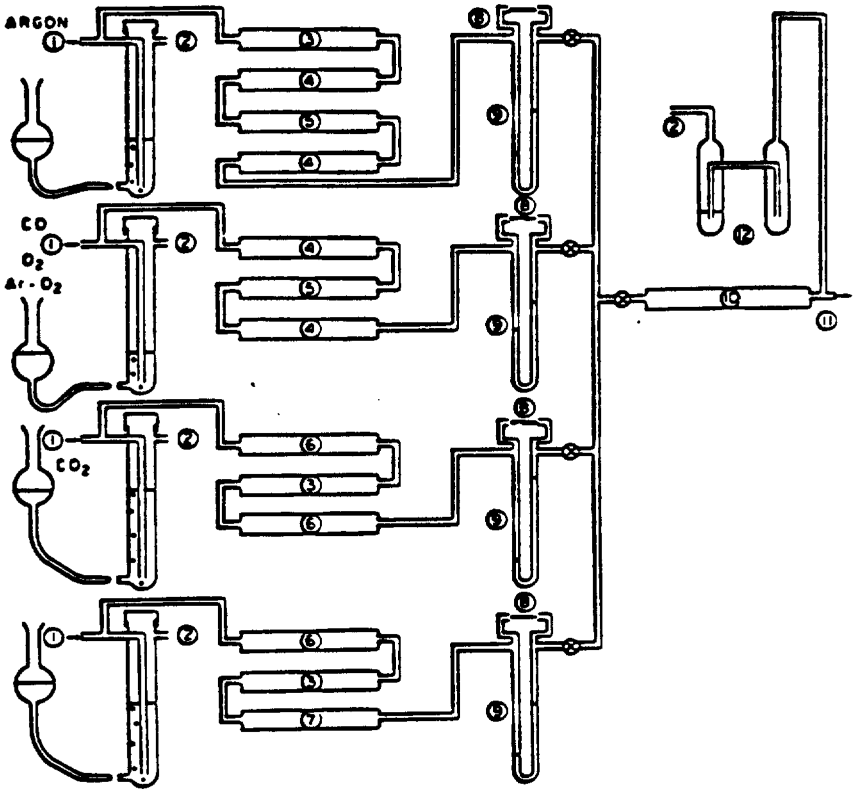

Figure.4.1: SCHEMATIC DIAGRAM OF THE GAS TRAIN

$$CO_2 = CO + \frac{1}{2}O_2 \tag{4.1}$$

The equilibrium constant for this reaction can be expressed as :

$$K_{4.1} = \frac{P_{CO}P_{O_2}^{\frac{1}{2}}}{P_{CO_2}} = \exp(-\frac{\Delta G^0_{4.1}}{RT}) \tag{4.2}$$

Hence,

$$P_{O_2} = \left[\frac{P_{CO_2}}{P_{CO}}\right]^2 exp(-\frac{2\Delta G^0_{4.1}}{RT}) = \left[\frac{P_{CO_2}}{P_{CO}}\right]^2 K_{4.1}^2 \tag{4.3}$$

$\Delta G^0_{4.1}$, the free energy of this reaction as a function of temperature can be obtained from the standard free energies for formation of CO and CO_2 and the values of $K_{4.1}$ as a function of temperature can be obtained from equation (4.2). Hence, the values of P_{O_2} can then be calculated for various CO/CO_2 ratios as functions of temperature from equation (4.3).

Darken and Gurry (71) have shown that thermal diffusion in a CO/CO_2 mixture may change the ratio of these gases in a heated, vertical tube. It was determined that at 1373 K, a flow velocity of more than 0.6 cm/sec would insure an error of less than 0.25% in the CO/CO_2 ratio as a result of thermal diffusion. A flow rate of twice this value, 1.2 cm/sec, introduced an error in temperature measurement. Consequently, a flow rate of 0.9 cm/sec was recommended. Accordingly, in this study, all experiments were performed at a linear flow rate of 0.9 cm/sec.

The control of P_{O_2} with the aid of reaction (4.1) was no longer possible if the desired P_{O_2} value is equal to or less than the equilibrium P_{O_2} value of the reaction:

$$CO_2 = C + O_2 \tag{4.4}$$

For this case, deposition of carbon occurred. In this study, the actual pressures used were higher than the equilibrium P_{O_2} value of reaction (4.4). In all cases, it was assumed that the gases behaved ideally, that is, their respective partial pressures were equal to their volume fractions in the flowing gas stream.

4.3 X-ray Diffraction

For x-ray analysis, powders prepared by the liquid mix method were heated at 1623 K for 24 hrs. to decompose organic solvents and residual carbonates and then further ground to 600 mesh size. X-ray fluorescence analysis were carried out using a Debye-Scherrer powder camera (57.3 mm. diameter) in a Siemens Kristalloflex-2 diffraction unit, using $CuK\alpha$ radiation and Ni-filter. The linear diffraction length of reflections were measured to an accuracy of 0.005 mm. X-ray diffractometry was also performed using a Norelco diffractometer and Geiger counter, again with $CuK\alpha$ radiation and Ni-filter. The diffractometer unit had computerized output capabilities for plotting intensity curves and also to print out angle intensity and d-spacing data.

4.4 Electrical Conductivity Measurements

Powder samples prepared by the liquid mix technique were compacted into thin circular discs (15 mm. diameter, 1.5 mm. thick) under an applied load of 40 Ksi and then sintered in air for 40 hrs. at 1698 K. For conductivity experiments, rectangular shaped specimens were cut from these discs using an airbrasive alumina cutter, with small notches on the sides to hold the platinum lead wires, as described elsewhere (10,72). A four probe direct current technique was utilized for conductivity measurements, wherein the potential drop between two fixed points on the sample (the two inner-most platinum wires) was measured using a high impedance ($> 10^{10}$ ohms) digital voltmeter (Keithley 191 digital multimeter), under a known current flow, supplied between the two outer leads, generated by a constant current source (Keithley 225 current source). From the cross-sectional area to length ratio (a/l) and the potential drop across this length , conductivity was calculated. The potential drop was measured under both forward and reverse polarity modes and conductivity was evaluated from the mean. Current was varied from 0.1 to 10 μA and no change in conductivity was noted. Recrystallized high purity alumina insulators were used to insulate the platinum lead wires. These wires exited through capillary tubes, sealed vacuum tight to a standard taper pyrex joint at the top of the furnace tube. Conductivity measurements were made only when the sample was in complete thermodynamic and thermal equilibrium with the surrounding gas environment at a given temperature. The furnace tube (alumina) employed in this investigation was heated using Kanthal-A1 heating elements accurate to ± 2 K. The temperature was measured using platinum-platinum 10% rhodium thermocouple. Conductivity experiments were performed over a temperature range of 1173-1373 K and P_{O_2} range of 10^0-10^{-19} atm. The desired P_{O_2} pressures were obtained to within ± 0.05 %, by flowing metered amounts of precision mixed argon-oxygen and carbon monoxide-carbon dioxide gas mixtures, using conventional manometer flow meters.

4.5 Thermogravimetric Measurements

Sintered discs (as in the case of conductivity experiments) were used for thermogravimetric analysis. These discs were suspended in a vertical tube furnace maintained at 1323 K using a platinum mesh basket. The samples were equilibrated in oxygen (for oxidized state at $P_{O_2} = 10^0$ atm.) or carbon dioxide-carbon monoxide mixtures (for reduced state at $P_{O_2} = 10^{-15}$ atm.) and then quenched to ambient gas by quickly raising the platinum basket to the cooler part of the furnace tube assembly. Gravimetric measurements were made at room temperature on at least duplicate samples on a Cahn Model 4100 microbalance. The average of at least six oxidation - reduction cycles was taken as the reversible weight change. The pure samples were light purple in the oxidized state and gray in the reduced state, whereas the doped samples were light yellow in the oxidized state and dark in the reduced state.

4.6 Diffusion Measurements

For diffusion studies, $SrZrO_3$ and $BaZrO_3$ discs (15 mm. diameter, 3 mm. thick) were separately prepared from the powder samples by compaction at an applied load of 40 Ksi. The $SrZrO_3$ discs were next sintered in air at 1798 K for 15 hrs. and the $BaZrO_3$ discs at 1823 K for 15 hrs. This small difference in the sintering temperature was necessary to obtain the same density for these discs. The surfaces of these discs were then polished using 600 grit SiC paper and diffusion couples were prepared by pressing the polished surfaces of the discs together at a sufficiently high pressure. In some cases, $BaZrO_3$ (or $SrZrO_3$) pastes were made by mixing the respective powders in an organic binder and applying a thin layer on the sintered $SrZrO_3$ (or $BaZrO_3$) discs through a silk-screen. The results obtained by this method were identical to the diffusion couple method. The diffusion couples were then annealed in a tube furnace at desired combinations of temperatures and times at which diffusion measurements were to be performed. After the diffusion anneal, the discs were sectioned in the middle (to eliminate surface effects) and the concentration of the diffusing species in each disc was measured as a function of distance from the interface in the direction of diffusion. An EDAX PV 9100 energy dispersive analysis unit attached to a cambridge Stereo Scan 250 (w/microspec) scanning electron microscope was used for composition analysis.

4.7 Raman Spectral Measurements

Powders prepared by the liquid mix method were heated at 1623 K for 24 hrs. These were then ground and the 600 mesh fraction was collected and placed in capillary tubes and supported by a sample holder for the back scattering geometry. A Spectra - Physics Model 164-05 Ar-ion laser with an excitation wavelengths of 4880 A and 5145 A was used in this study. This laser provided a well focussed, monochromatic light source. A Jarrell-Ash 25-300 Raman Spectrophotometer equipped with an RCA C31034 (Ga-As) photomultiplier and an ORTEC (Model 9302) amplifier/discriminator was used to analyze the scattered light. Photon counting was carried out with a Computer Automation LSI/2 computer having 32K core memory. The Raman spectra were recorded in the range of 100-1100 cm^{-1}. The incident power of the laser beam was approximately 90 mW and this beam was focussed using a condensing lens to a spot size of < 1 mm. on the specimen. The scattered radiation was collected by a Nikkor-S f 1.0 objective lens with a focal length of 55 mm. and focussed onto the entrance slit of a double monochromator. A Tektronix model 4010-1 interactive graphics terminal provided rapid and accurate spectral analysis. Rapid corrections for spectral background near the laser line were possible with the improved electronic system of the Raman Spectrophotometer. In this study, a scan rate of 2 cm^{-1}/sec and a spectral slit width of 5 cm^{-1} were used. Each sample was scanned at least twice and the summed spectra were recorded. To obtain spectra at 277 K and 77 K, the capillary tubes containing the powder samples were immersed in a cold finger Dewar containing either ice or liquid nitrogen, respectively (126,127).

4.8 Electron Microscopy

Sintered specimens were examined in a JEOL JSM-35 scanning electron microscope at a secondary electron accelerating voltage of 25 kV and at various magnifications. A thin film (200 A°) of gold was deposited on these discs by plasma splattering in a Hummer coater at a pressure of about 10^{-4} mm. of Hg, to render the surface of examination conductive. When necessary, the composition of the discs was also analyzed using the Ortec EEDS II energy dispersive analysis detector attached to the scanning electron microscope.

For transmission electron microscopy, the powders prepared by the liquid mix technique, were used as such, after heating at 1623 K for 24 hrs. Small amounts of 600 mesh fraction of these powders were spread on a double walled copper grid specimen holder and then examined in a Hitachi HU-11B transmission electron microscope under an accelerating voltage of 100 kV and at various magnifications.

5. RESULTS AND DISCUSSION

5.1 Solubility Limit of La in $SrZrO_3$

The addition of La has been shown to have pronounced effects on both the electrical conductivity and the dielectric properties of $SrO-TiO_2$ (24), $PbO-TiO_2$ (26), $BaO-TiO_2$ (73) and $Pb(Zr,Ti)O_3$ (20), which are systems similar in structure to $SrZrO_3$. By analogy, it is possible to envisage similar effects when La is added to $SrZrO_3$ (wherein La has been substituted on part of the A sites). The creation of A-site vacancies can be achieved through an ordered structural accomodation (22,74). The existence of a perovskite phase of composition $Sr_{1-3x/2}La_xTiO_3$ in the ternary system $SrO-TiO_2-La_2O_3$ has been reported by Tien and Hummel (24). In all their samples, the large-cation to small-cation ratio was less than unity. Similar results were found in La-substituted lead titanate (27), in which perovskite phases of the composition $Pb_{1-3x/2}La_xTiO_3$ were produced. The perovskite phases in $(La,Sr)ZrO_3$ can be analogously considered as a series of mixed - crystals of $SrZrO_3-La_{2/3}\square_{1/3}ZrO_3$, where $\square$ represents a vacant La site. In this investigation, x-ray fluorescence, diffraction and scanning electron microscopy techniques were used to determine the range of existence of the homogeneous perovskite phase, $SrO-La_2O_3-ZrO_2$, in the quasi-ternary system. The changes in the microstructure effected by La addition were also studied through transmission electron microscopy and dark field imaging was carried out to identify any second phase precipitation.

The microstructure of pure $SrZrO_3$, as revealed in the scanning electron microscope, is shown in Figure 5.1(a). With increasing La concentration, up to 6 at.%, there was no significant change in this structure (Figure 5.1(b)). When the amount of La reached 7 at.%, long, needle-shaped precipitates started appearing (Figure 5.1(c)) and at 10 at.%, these acicular precipitates were even more copious and readily visible (Figure 5.1(d)). These precipitates were on an average

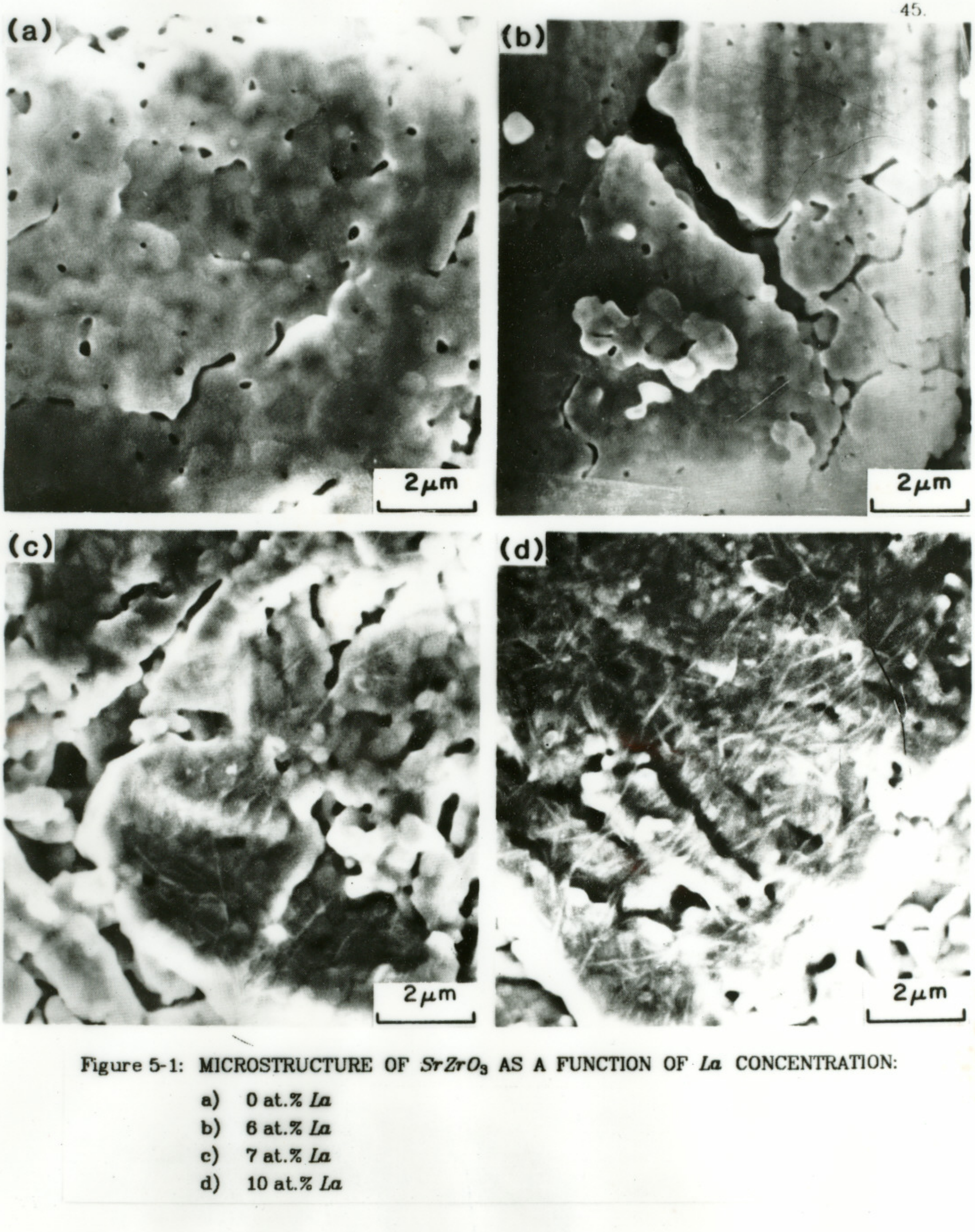

Figure 5-1: MICROSTRUCTURE OF $SrZrO_3$ AS A FUNCTION OF *La* CONCENTRATION:

a) 0 at.% *La*
b) 6 at.% *La*
c) 7 at.% *La*
d) 10 at.% *La*

1000 nm long and 100 nm thick. Energy dispersive x-ray analysis revealed virtually no Sr counts from these precipitates, although the La and Zr counts remained high. Similar needle-shaped precipitates in La-doped $PbTiO_3$ (26) and La-doped $SrTiO_3$ (25) have been reported and these precipitates were identified as $La_2Ti_2O_7$, in both systems.

X-ray powder diffraction patterns, from the pure $SrZrO_3$ compound, exhibited strong (020,112), (220, 004), (024,132,312) and (224,400) reflections in addition to several weaker reflections. The value of the lattice constants determined for this orthorhombic structure were: a = 0.58028 nm, b = 0.58296 nm, and c = 0.82048 nm, which agree well with those determined elsewhere (75,76). No extra lines were observed with La additions up to 6 at.%. However, the lattice parameter decrease was consistent with the lower ionic size of La, compared to Sr. At 7 at.% La, extra lines appeared with strong (222), (400), (440) and (622) reflections. These lines were assignable to the cubic $La_2Zr_2O_7$ structure. With further additions of La, the extra lines increased in intensity, indicating a greater volume fraction of the second phase. The lattice parameter, however, remained unchanged.

The diffractometer data were also consistent with the above results. Pure $SrZrO_3$ exhibited an intensity pattern as shown in Figure 5.2(a) with primary peaks corresponding to (020,112), (220,004), (024,132,312) and (224,400). This pattern was unchanged up to 6 at.% La (Figure 5.2(b)). Extra peaks started appearing when the La concentration reached 7 at.%. These are indicated in Figure 5.2(c) and correspond to (222), (400), (440), and (622) reflections of $La_2Zr_2O_7$. The intensity of these peaks increased at higher amounts of La (Figure 5.2(d)). A standard parametric method was also used for determining the solubility limit of La in $SrZrO_3$. For this, the lattice parameter 'a' of $SrZrO_3$ was obtained by measuring diffraction lines and extrapolating by the method of

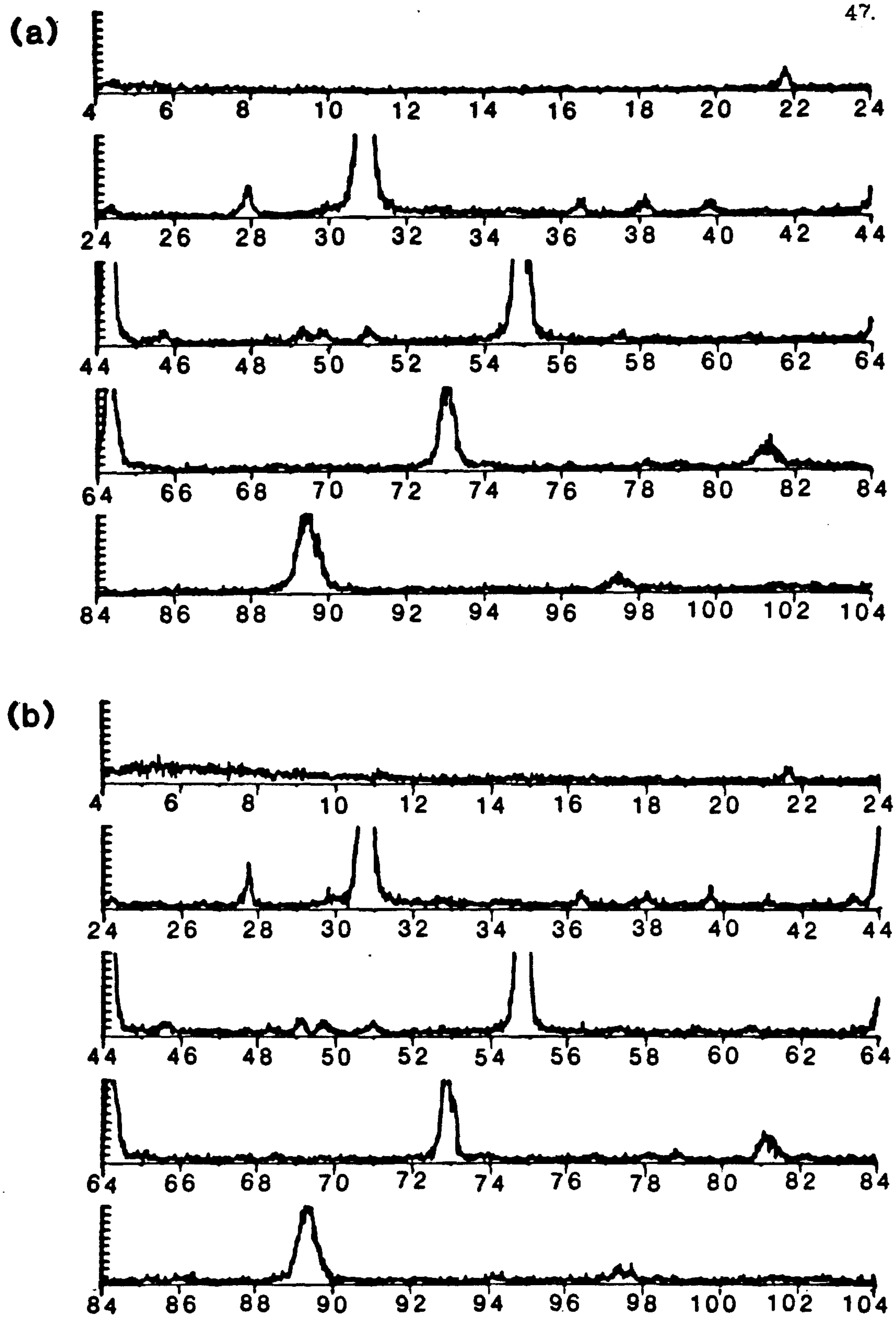

Figure 5-2: DIFFRACTION PATTERNS (INTENSITY VS. BRAGG ANGLE) OF $SrZrO_3$ AS A FUNCTION OF *La* CONCENTRATION:

a) 0 at.% *La*

b) 6 at.% *La*

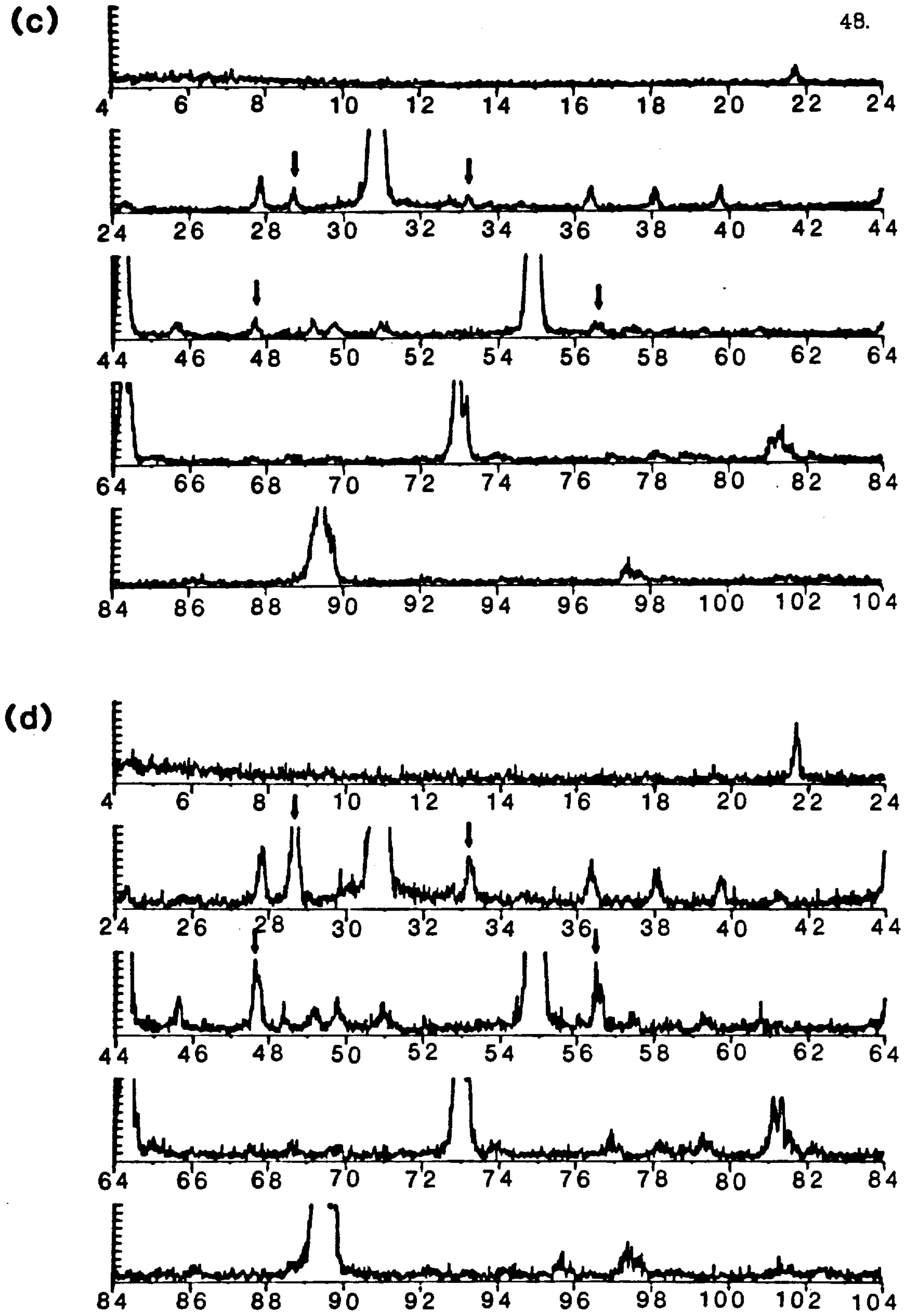

Figure 5-2: DIFFRACTION PATTERNS (INTENSITY VS. BRAGG ANGLE) OF $SrZrO_3$
(cont.) AS A FUNCTION OF *La* CONCENTRATION:

c) 7 at.% *La*

d) 10 at.% *La*

Nelson and Riley (77). The lattice constant of $SrZrO_3$, thus determined, was plotted as a function of La concentration (Figure 5.3). The resulting curve exhibited a change in slope at approximately 6 at.% La. Up to 6 at.% La, there was a linear relationship between lattice parameter and at.% La, consistent with a Vegard's law dependence. Above 6 at.% La, the lattice constant did not change, due to the precipitation of a second phase.

Bright field transmission electron micrographs, indicating the microstructure of pure $SrZrO_3$, are presented in Figure 5.4. The corresponding selected area diffraction patterns obtained from these regions are those of typical polycrystalline specimens, with no evidence of any extra reflections, besides those due to the orthorhombic structure of $SrZrO_3$. The observed reflections are indexed in Table 5.1. The lattice constants of pure $SrZrO_3$ were then calculated by selecting any three (hkl) values and the corresponding d_{hkl} values and using the relationship:

$$\frac{1}{d^2} = \frac{h^2}{a^2} + \frac{k^2}{b^2} + \frac{l^2}{c^2} \tag{5.1}$$

for orthorhombic structure. These values were found to be 0.5768 nm, 0.5804 nm and 0.8154 nm for a, b and c respectively and are consistent with those reported elsewhere (75,76). Figure 5.5 indicates transmission electron micrographs obtained from the 6 at.% La-doped $SrZrO_3$ samples. Again no difference was noted either in the bright field structures or in the diffraction patterns, the patterns still exhibiting an absence of extra reflections assignable to second phases. This indicates that upto this concentration, La forms a homogeneous solid solution in $SrZrO_3$ and no phase separation occurs. When the concentration of La was increased to 7 at.%, the microstructure exhibited needle like precipitates, about 30 nm long (Figures 5.6 and 5.7). Using the spots circled in the diffraction pattern (Figures 5.6(c) and 5.7(c)), dark field images of these

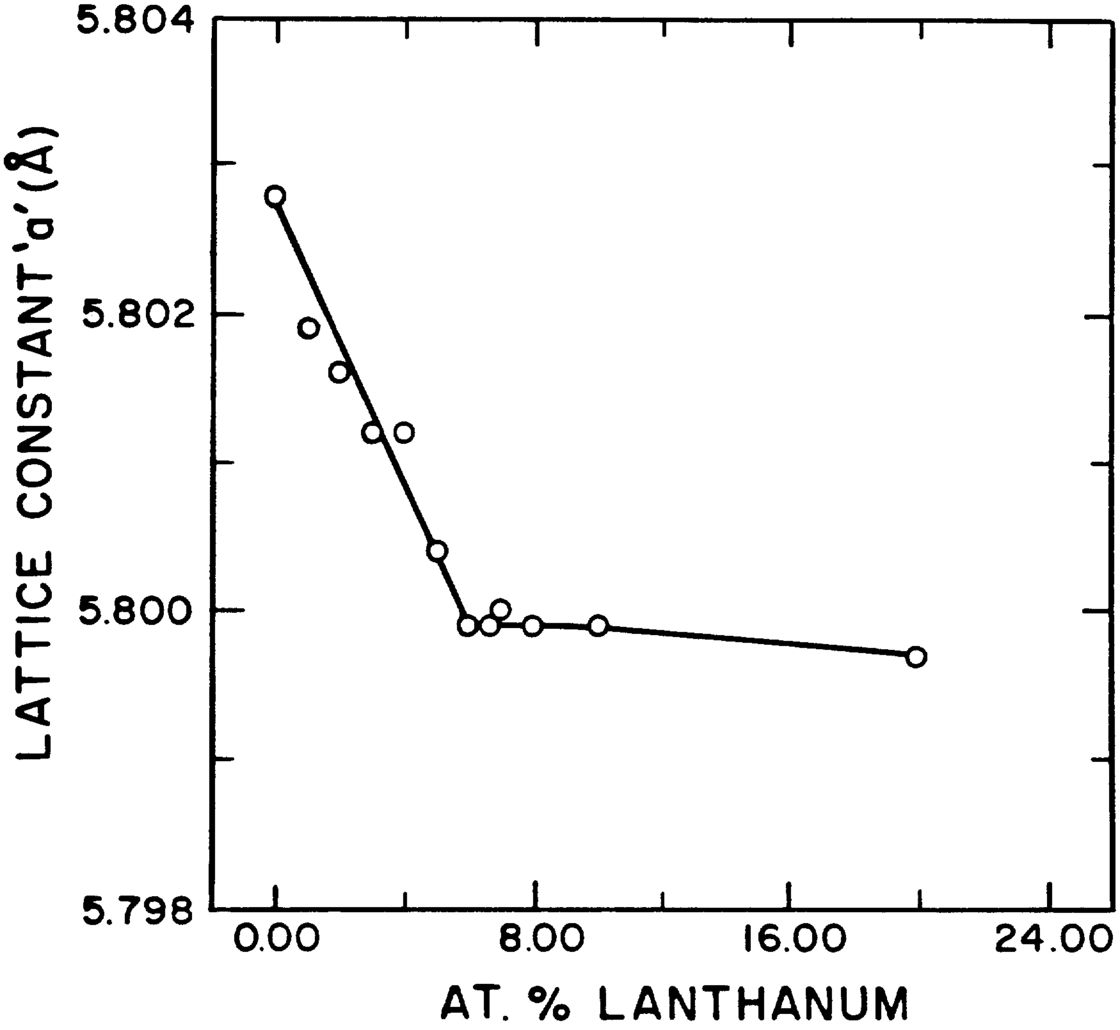

Figure 5-3: LATTICE CONSTANT OF $SrZrO_3$ AS A FUNCTION OF *La* CONCENTRATION

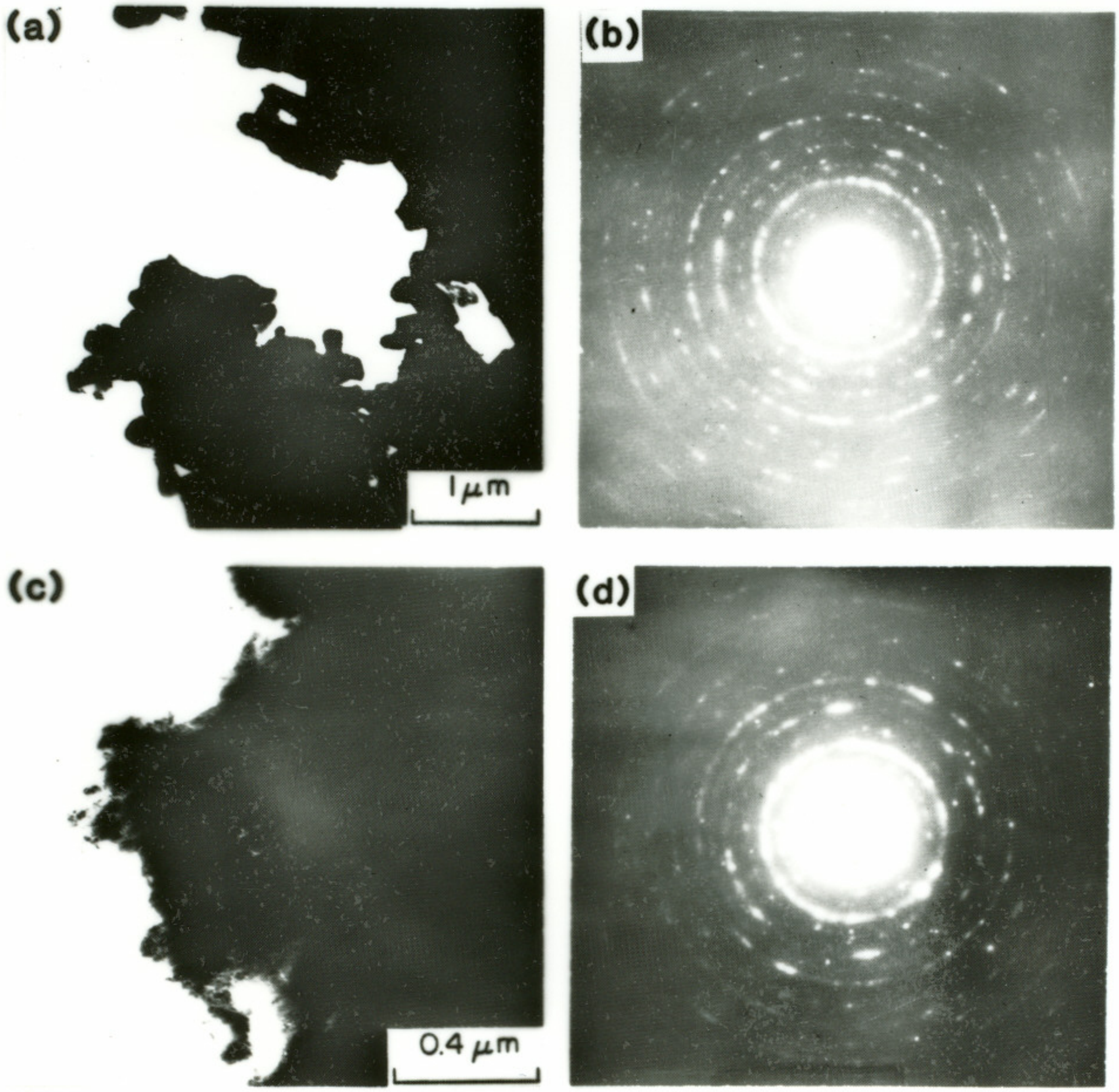

Figure 5-4: T.E.M. MICROGRAPHS OBTAINED FROM PURE $SrZrO_3$:

a) Bright field image
b) S.A.D. pattern from (a)
c) Bright field image
d) S.A.D. pattern from (c)

Table 5.1

CALCULATED REFLECTIONS IN $SrZrO_3$, OBTAINED FROM FIGURE 5.4

R (mm)	Intensity	d_{hkl}	hkl
9.075	weak	4.077	002
10.600	weak	3.49	111
12.750	very strong	2.902	020,112
15.665	weak	2.362	202
18.210	strong	2.032	220,004
20.650	weak	1.792	311
22.225	strong	1.665	312,132,024
25.650	weak	1.442	242,400

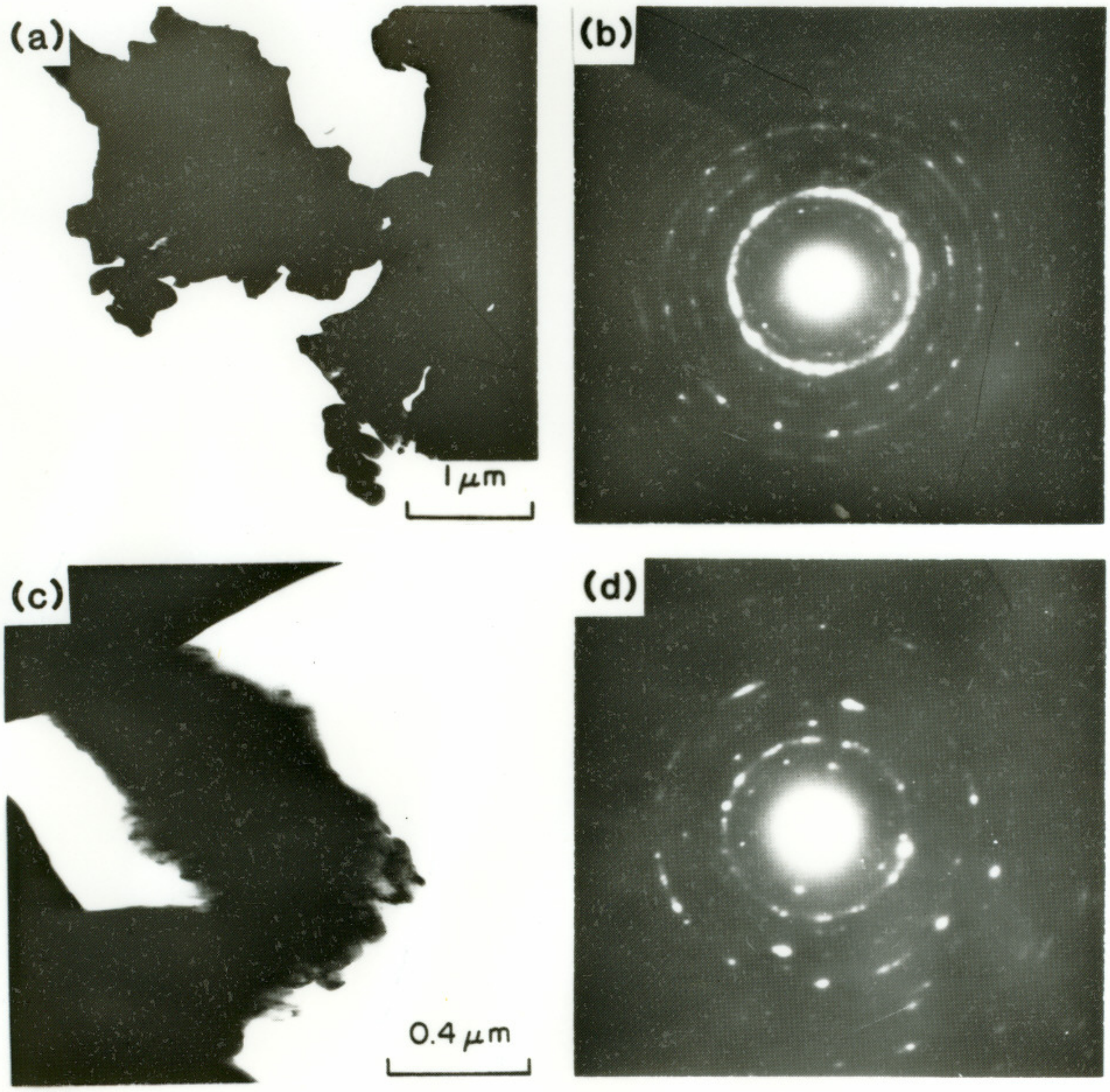

Figure 5-5: T.E.M. MICROGRAPHS OBTAINED FROM 6 AT.% *La*-DOPED $SrZrO_3$:

- a) Bright field image
- b) S.A.D. pattern from (a)
- c) Bright field image
- d) S.A.D. pattern from (c)

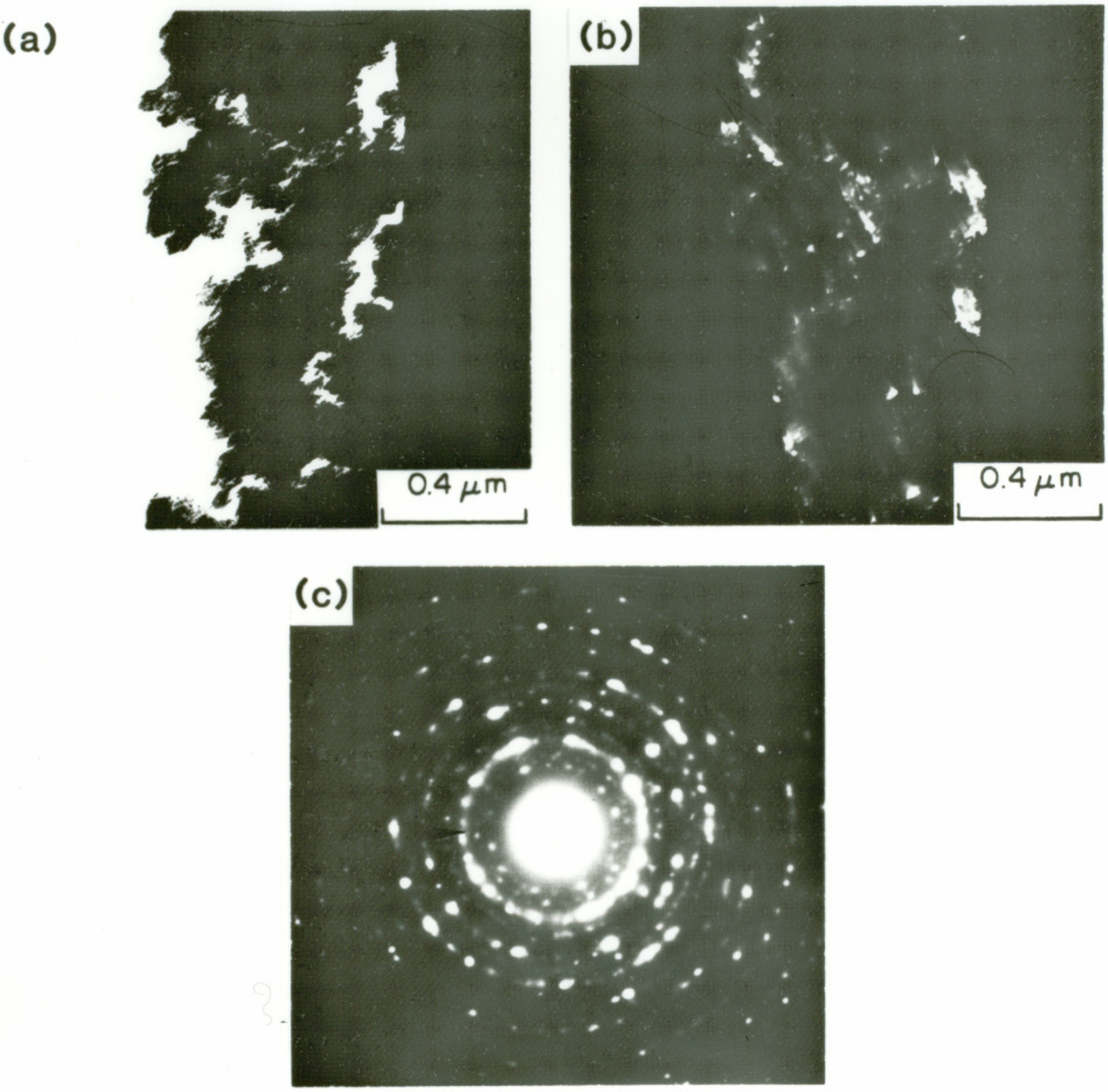

Figure 5-6: T.E.M. MICROGRAPHS OBTAINED FROM 7 AT.% La- DOPED $SrZrO_3$:

a) Bright field image

b) Dark field image using (222) $La_2Zr_2O_7$ (marked spot)

c) S.A.D. pattern from (a)

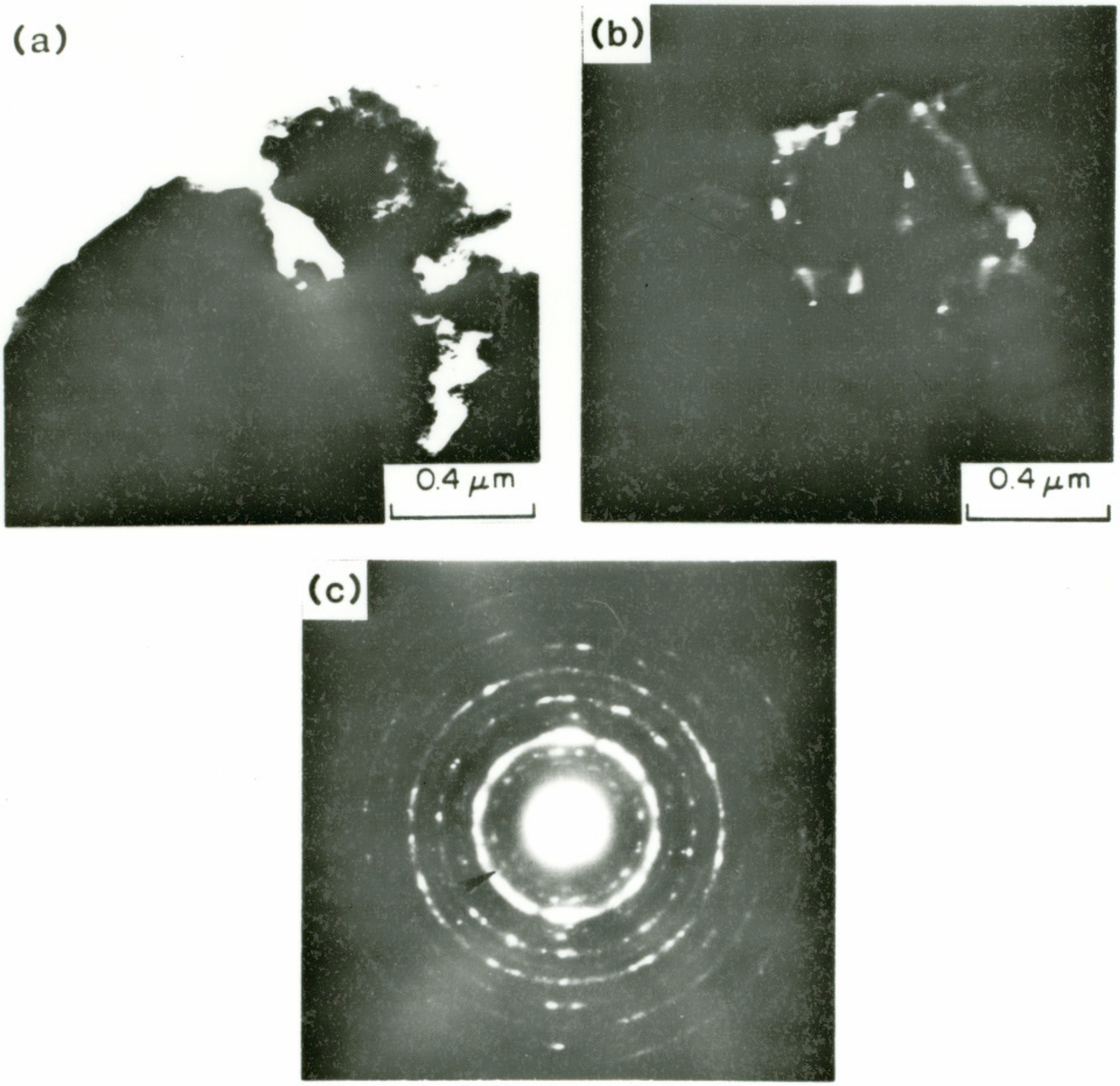

Figure 5-7: T.E.M. MICROGRAPHS OBTAINED FROM 7 AT.% La- DOPED $SrZrO_3$:

a) Bright field image

b) Dark field image using (222) $La_2Zr_2O_7$ (marked spot)

c) S.A.D. pattern from (a)

precipitates were obtained (Figures 5.6(b) and 5.7(b)). The precipitates were highlighted well in the dark field mode. The circled reciprocal lattice spots were assignable to (222) $La_2Zr_2O_7$. Besides these, additional reflections were also obtained from {400}, {440}, and {622} planes as indexed in Table 5.2. Transmission electron microscopy images were also obtained at a higher level of La (10 at.%). As seen in Figures 5.8 and 5.9, the precipitates exhibited considerable coarsening. The dark field images were again obtained from (222) $La_2Zr_2O_7$ reflections, as indicated in the diffraction patterns and the precipitate size was measured to be approximately 30 nm.

Figures 5.10 and 5.11 represent the proposed equilibrium diagram for $SrO-ZrO_2$ (75) and $ZrO_2-La_2O_3$ (78). The partial ternary system $SrO-La_2O_3-ZrO_2$, that was generated by considering the isothermal section at 1623 K in Figures 5.10 and 5.11, is given in Figure 5.12. From this ternary diagram, the range of existence of the perovskite phase can be inferred to be small. This prediction is in agreement with the experimental results.

5.2 Thermogravimetric Measurements

The results of thermogravimetric measurements, performed at 1323 K for pure $SrZrO_3$ and upto 6 at.% La-doped $SrZrO_3$, are given in Figure 5.13. The solid line represents the calculated amount of oxygen necessary to compensate for the added La^{+3} ions, assuming that each oxygen ion neutralizes two La^{+3} dopant ions. The horizontal line indicates the maximum oxygen non-stoichiometry in undoped $SrZrO_3$. These gravimetric measurements show that the reversible change of oxygen content, between specified states of oxidation and reduction, is proportional to the dopant concentration. As can be seen, there is good agreement between the calculated amount of oxygen necessary to compensate for the La^{+3} ions and the measured reversible oxygen weight change between the

Table.5.2

CALCULATED $La_2Zr_2O_7$ REFLECTIONS IN 7 AT.% La-DOPED $SrZrO_3$ OBTAINED FROM FIGURES 5.6 AND 5.7

R (mm)	d_{hkl}	hkl	comments
11.890	3.111	222	from $La_2Zr_2O_7$
14.175	2.610	400	from $La_2Zr_2O_7$
19.400	1.907	440	from $La_2Zr_2O_7$
22.910	1.615	622	from $La_2Zr_2O_7$

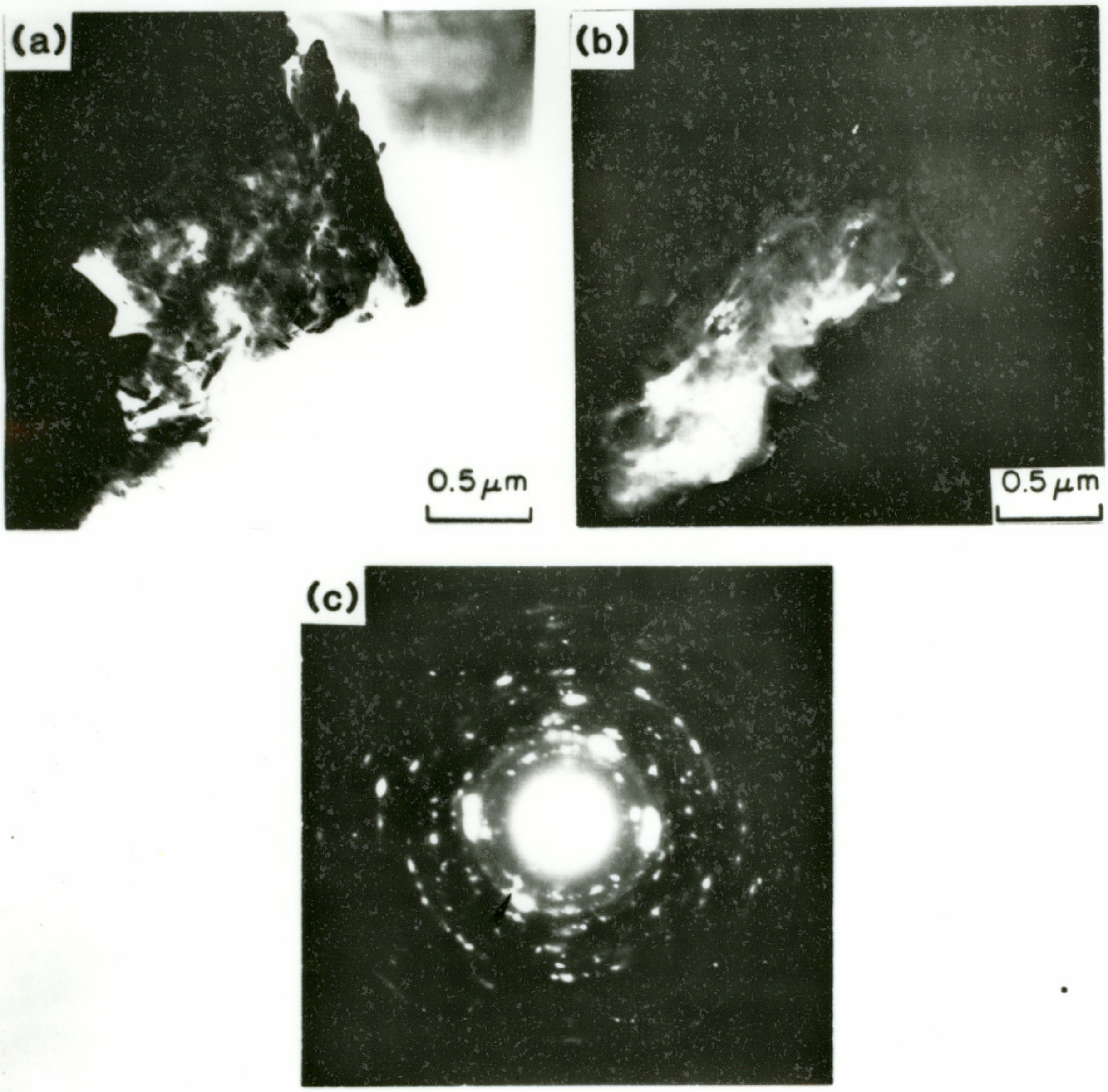

Figure 5-8: T.E.M. MICROGRAPHS OBTAINED FROM 10 AT.% *La* - DOPED $SrZrO_3$:

- a) Bright field image
- b) Dark field image using (222) $La_2Zr_2O_7$ (marked spot)
- c) S.A.D. pattern from (a)

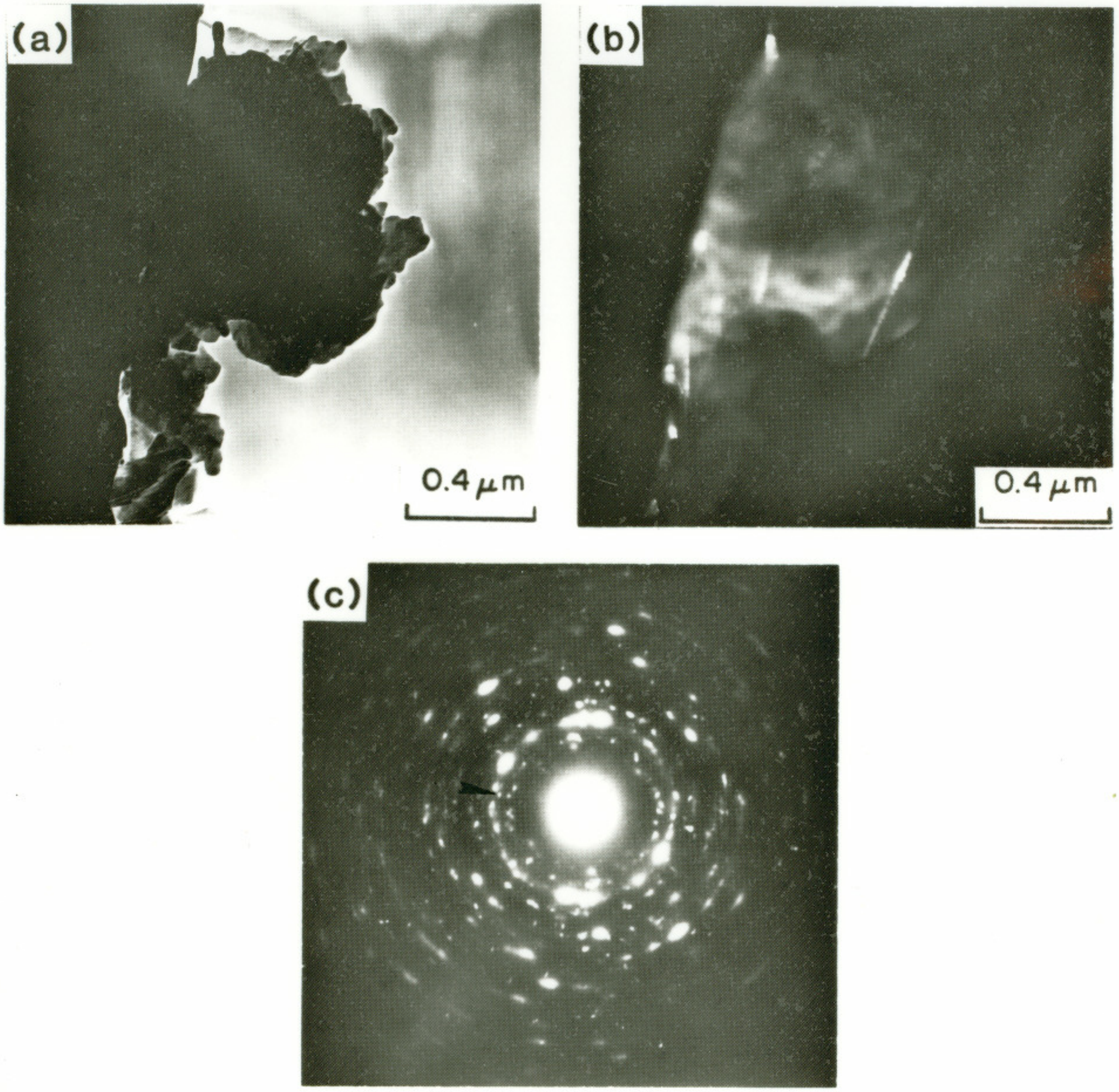

Figure 5-9: T.E.M. MICROGRAPHS OBTAINED FROM 10 AT.% La - DOPED $SrZrO_3$:

a) Bright field image

b) Dark field image using (222) $La_2Zr_2O_7$ (marked spot)

c) S.A.D. pattern from (a)

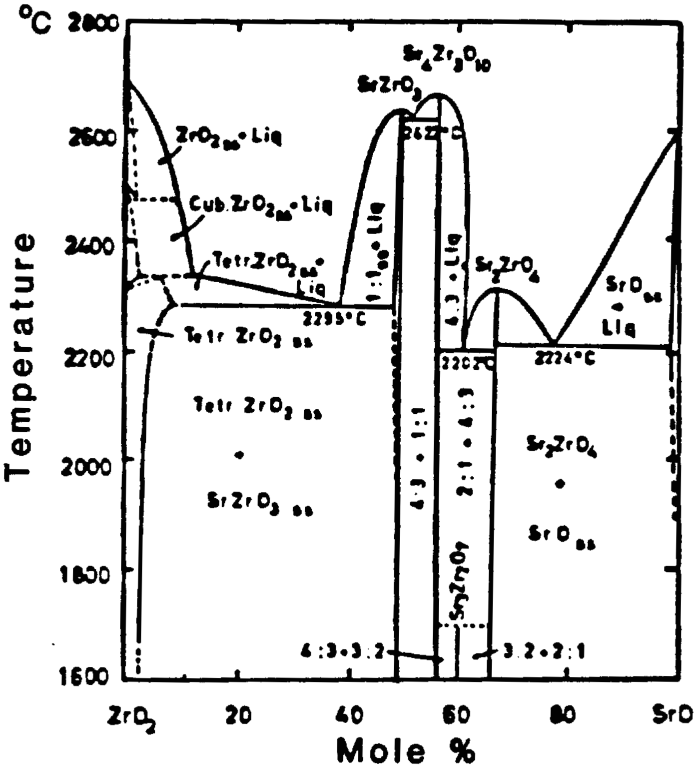

Figure 5-10: TENTATIVE PHASE DIAGRAM OF ZrO_2–SrO SYSTEM [75]

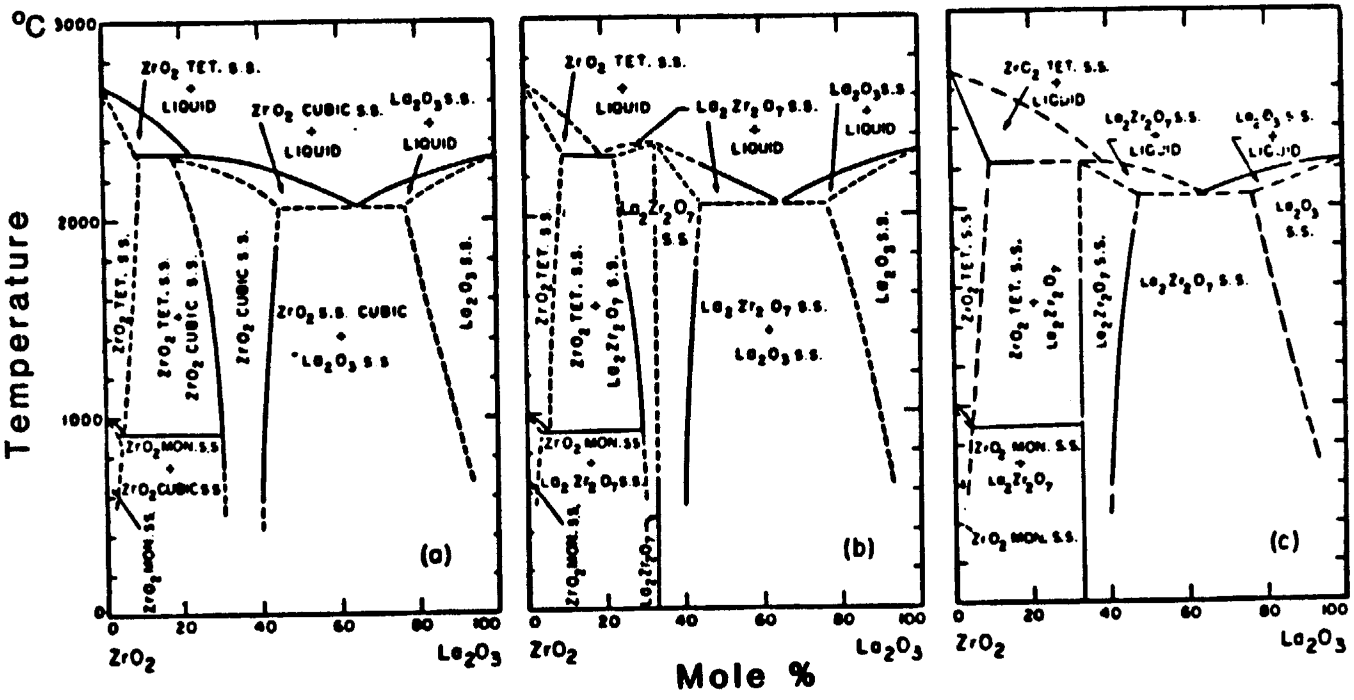

Figure 5-11: POSSIBLE PHASE EQUILIBRIA IN ZrO_2–La_2O_3 SYSTEM [78]

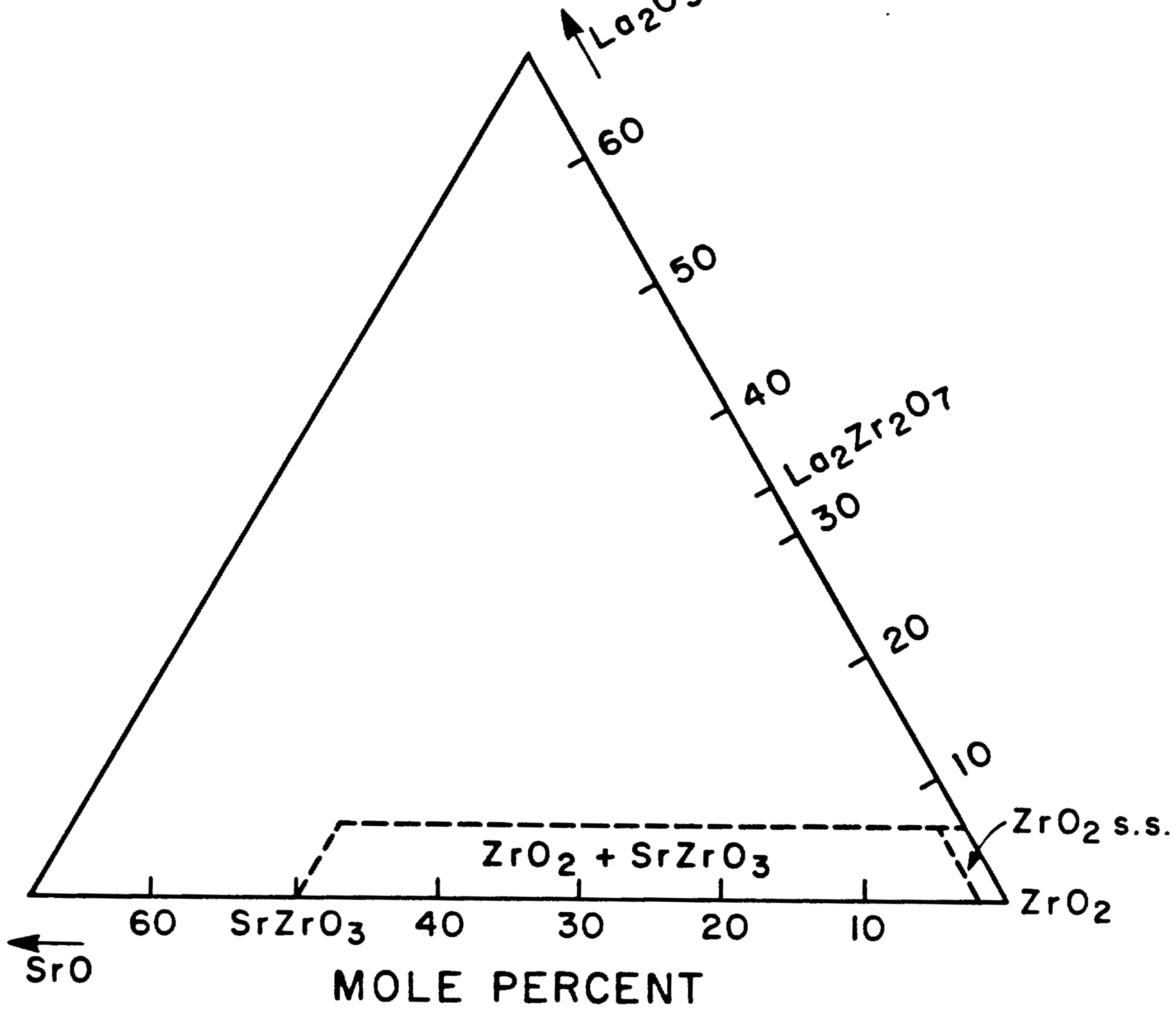

Figure 5-12: CALCULATED PARTIAL TERNARY PHASE DIAGRAM OF $SrO-ZrO_2-La_2O_3$ SYSTEM

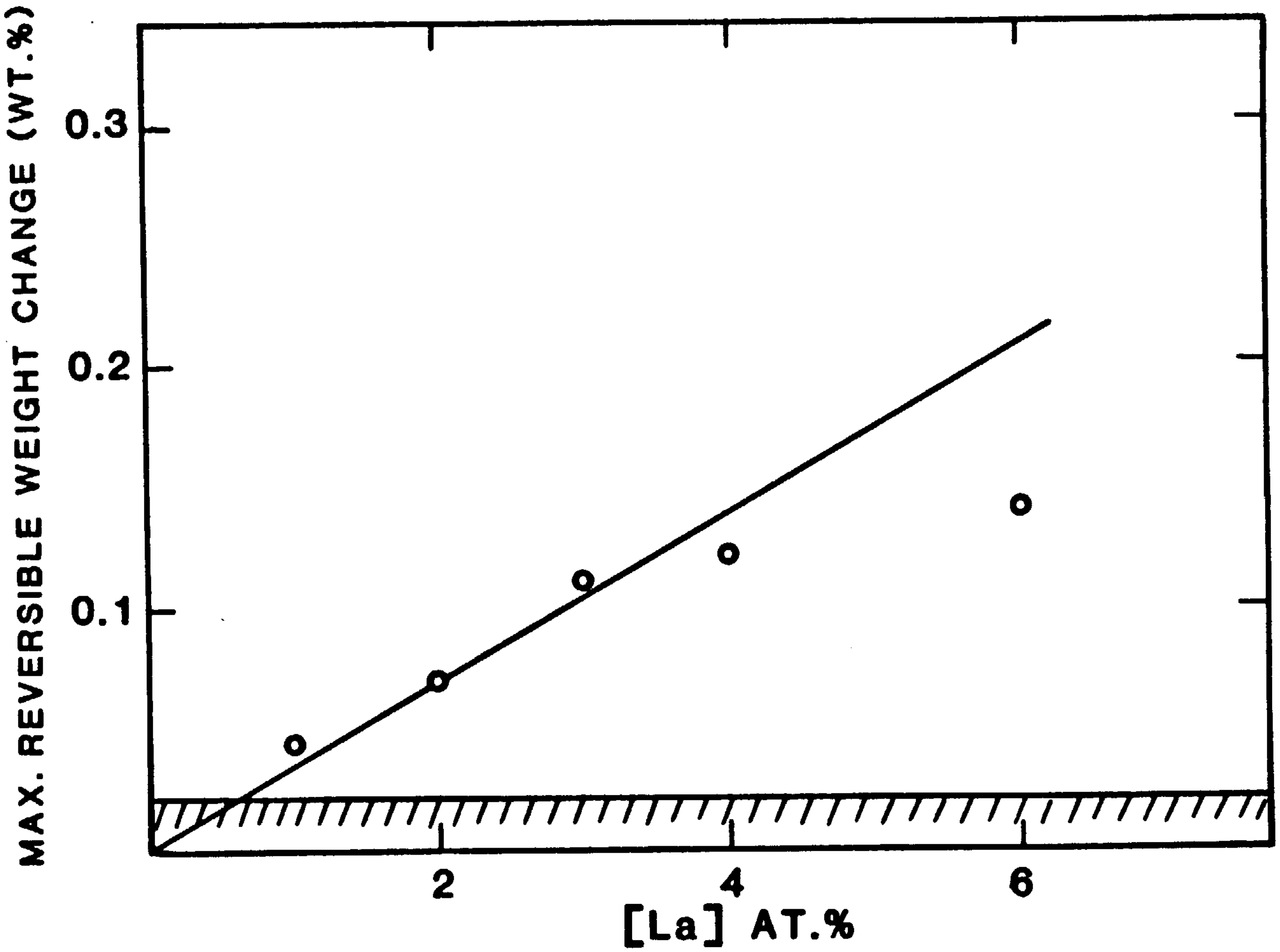

Figure 5-13: MAXIMUM REVERSIBLE WEIGHT CHANGE OF $SrZrO_3$ AS A FUNCTION OF *La* CONCENTRATION.

oxidized state at atmospheric oxygen pressure and the reduced state established in CO/CO_2 mixtures. However, at high La dopant levels ($\geq$ 4 at.% La concentration, which is near the solubility limit of La in $SrZrO_3$, as demonstrated in Section 5.1), the extremely slow oxidation kinetics rendered obtaining quantitative results difficult. Nevertheless, even at these high concentrations, there is self-compensation.

In the oxidized state, the undoped $SrZrO_3$ samples were light purple in color and all the doped samples were light yellow. However, in the reduced state, all undoped and doped samples looked dark, with the undoped and lightly doped samples appearing dark gray and the more heavily doped samples appearing darker. No thermogravimetric data on the self compensation of $SrZrO_3$ are available elsewhere in the literature. Nevertheless, based on the work of Eror and Smyth (22), the observation of oxygen stoichiometric compensation can be explained as follows:

Case 1 : The addition of oxygen on oxygen sites, creating both strontium and zirconium vacancies, although the latter is unlikely structurally. More work is needed before disclaiming this case, especially in the light of recent evidences which indicate the formation of B site cation vacancies in similar perovskite compounds (124,125).

Case 2 : A shift of the cation site, occupied by the donor-dopant species, when the samples are oxidized. The possibility of a change in cation site seems unlikely, because of the low probability for creating zirconium vacancies in the perovskite structure. However, careful x-ray diffraction measurements is necessary before completely discounting this possibility, as well as the case 1 possibility.

Case 3 : A reversible change from a classic, randomly- distributed, point defect model in the reduced state, to a compensated structure, with ordered defects in the oxidized state. Accordingly, under the sample preparation conditions (during calcination, these samples need an oxidizing atmosphere to complete the process), or in the oxidizing state of equilibration, the system absorbs an amount of oxygen from the atmosphere and compensates for the extra charge of La by the formation of strontium vacancies, as follows:

$$2La_{Sr}^{\cdot}+Sr_{Sr}+\frac{1}{2}O_2 = SrO+2La_{Sr}^{\cdot}+V_{Sr}^{''}+2p \tag{5.2}$$

The above models propose that the compensation of donor-doped $SrZrO_3$ occurs by the creation of strontium vacancies. However, since a ternary oxide is involved, the additional strontium atoms that result from the strontium vacancies, combine with oxygen atoms accounting for the gravimetric observation. This SrO does not represent a separate phase, but, rather a structural accomodation in an ordered fashion. This concept has also been utilized to explain the formation of $SrTi_2O_3$ and $Sr_4Ti_3O_{10}$ phases through the incorporation of ordered layers of SrO between the perovskite $SrTiO_3$ unit cells in other studies (79).

5.3 Electrical Conductivity of Undoped $SrZrO_3$

The few prior investigations on the electrical conductivity measurements of pure $SrZrO_3$ were limited to ambient P_{O_2} (28,29) or pressure ranging over only six decades of P_{O_2} (30,32,34) and involved specimen preparation in the solid state, wherein homogenization over a few parts per million (<10 ppm) is not achievable as in the liquid mix method (22,64). Further, some inconsistencies exist in the reported values of conductivity and activation enthalpy for the conduction process. Hence, in this study, the conductivity of $SrZrO_3$, prepared by the liquid mix technique, was evaluated over a temperature range of 1173 - 1373 K and P_{O_2} values varying between 10^0 - 10^{-15} atm. (Figures 5.14 and 5.15). No data points were obtained in the P_{O_2} range of 10^{-5} - 10^{-6} atm. due to the non-

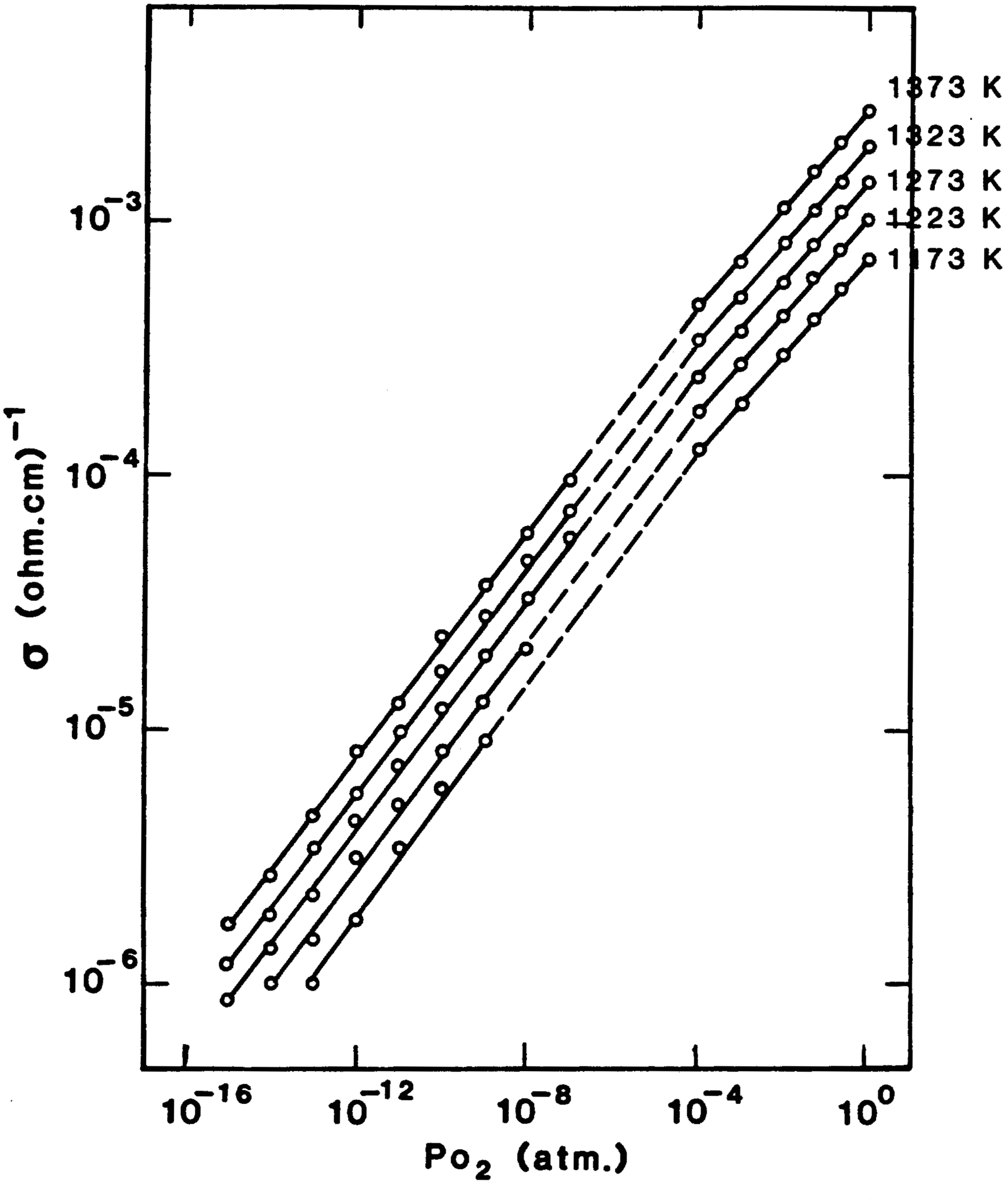

Figure 5-14: ELECTRICAL CONDUCTIVITY OF $SrZrO_3$ AS A FUNCTION OF P_{O_2} (CASE 1)

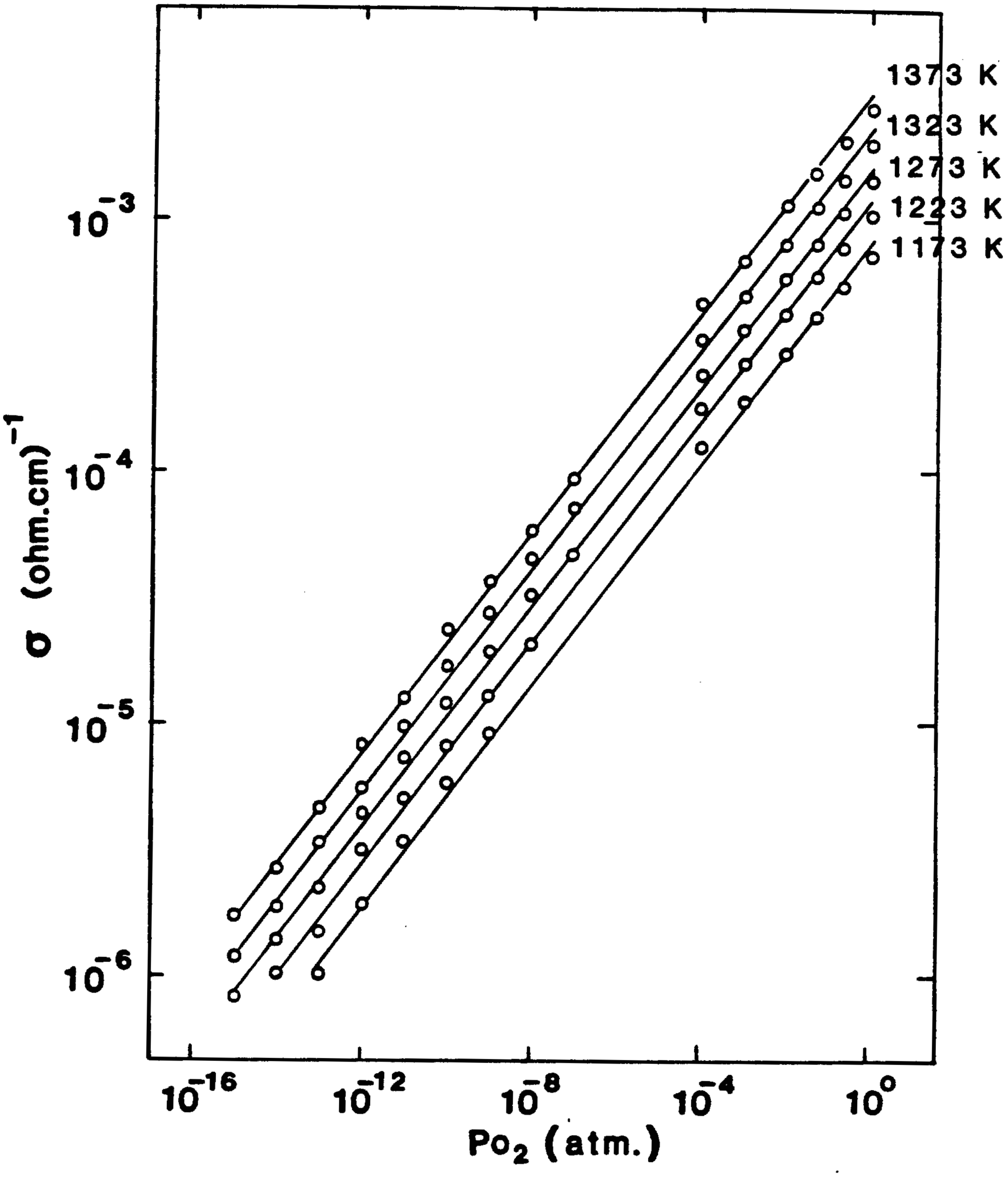

Figure 5-15: ELECTRICAL CONDUCTIVITY OF $SrZrO_3$ AS A FUNCTION OF P_{O_2} (CASE 2)

availability of a suitable gas mixture. As noted by Schmalzried (66), in ternary systems, the chemical potential of two of the three components must be specified in order to determine the equilibrium thermodynamic state for each of the components on given lattice sites and each of the point defects. In this study, the Sr and Zr activities were not independently fixed, but, instead, the Sr/Zr ratio was fixed as unity. If volatilization of these cations is insignificant, the variation of defect concentrations with change in oxygen activity is defined (80). As seen in Figures 5.14 and 5.15, $SrZrO_3$ exhibited a p-type behavior throughout the P_{O_2} range of study (10^0 - 10^{-15} atm.).

The results can be interpreted two ways:

The P_{O_2} range can be subdivided into two regions (10^0 -10^{-4} atm. and 10^{-7} - 10^{-15} atm.) and each region analysed separately for conductivity behavior (Case 1, Figure 5.14). Alternatively, the entire P_{O_2} range can be treated as a single region within which conductivity behavior is uniform (Case 2, Figure 5.15).

Case 1 (Figure 5.14): In the high P_{O_2} region (10^0 - 10^{-4} atm.), conductivity decreased linearly as the 3/16 power of P_{O_2} at all temperatures. The actual values of the slopes of these lines are listed in Table 5.3 and varied from 1/5.242 to 1/5.276.

As already explained in Section 1.2, for a pure ABO_3 compound, with an A/B ratio of 1, a theoretical defect concentration vs. P_{O_2} diagram can be generated (1) as shown in Figures 1.1 and 1.2. In addition to electrons and holes, the major point defects are fully ionized vacancies of oxygen and cations A and B. The electrical neutrality equation, viz.,

$$[p]+2[V_O^{\cdot\cdot}]=[n]+2[V_A^{''}]+4[V_B^{''''}] \qquad (1.35)$$

can be further simplified into three conditions for low, intermediate and high P_{O_2} region (equations 1.36-1.39). The slopes of the various defect curves in the

Table.5.3

P_{O_2} DEPENDENCE OF CONDUCTIVITY IN THE REGION 10^0-10^{-4} ATM.

Temperature (K)	m for $\sigma_p \alpha P_{O_2}{}^{1/m}$
1173	5.276
1223	5.276
1273	5.242
1323	5.274
1373	5.263

high P_{O_2} region can be obtained from Table 1.3 by considering the simplified neutrality condition (equation 1.37) for this region, viz.,

$$[p]=2[V_A'']+4[V_B''''] \tag{1.37}$$

Electrical conductivity is a function of both n and p type conduction and can be expressed as:

$$\sigma = \sigma_n + \sigma_p \tag{5.3}$$

where,

$$\sigma_n = e^- \mu_n [n] \tag{5.4}$$

and,

$$\sigma_p = e^+ \mu_p [p] \tag{5.5}$$

The values of conductivity are thus proportional to the concentration of either electrons or holes, whichever is dominant. If the conductivity vs. P_{O_2} curve is incorporated in Figure 1.1 or 1.2 it would be parallel to the [n] or [p] curve, depending upon their relative positions, and the slope of the conductivity curve would be the same as that of the dominant [n] or [p] defect curve. The experimental values for conductivity varied as the 3/16 power of P_{O_2} in the high P_{O_2} region and examination of the slopes of the conductivity curve in Table 1.3 indicates that the experimental values are consistent with the Schottky reaction for which the simplified neutrality condition is given by equation 1.37. The variation of electrical conductivity with P_{O_2} in this region can be explained in terms of an oxidation reaction, which creates ionized vacancies of A and B sites, by incorporating oxygen from the gas phase into the lattice, making six holes available for conduction in the process. This oxidation reaction can be expressed as:

$$\frac{3}{2}O_2 = 3O_O + V_A'' + V_B'''' + 6p \tag{5.6}$$

The equilibrium constant $K_{5.6}$ for this reaction is given by:

$$K_{5.6} = \frac{[V_A'']^2[p]^6}{P_{O_2}^{\frac{3}{2}}} = \exp(\frac{-\Delta G_{5.4}}{RT}) \tag{5.7}$$

where, G is the Gibbs standard free energy change (assuming that the defects exist in dilute solution and do not interact). Combining the above equation with equation 1.37 (simplified neutrality condition for this region) and splitting the free energy change into the entropy and enthalpy components yields:

$$p = 6^{\frac{1}{4}} P_{O_2}^{\frac{3}{16}} \exp(\frac{\Delta S_{5.6}}{8R} - \frac{\Delta H_{5.6}}{8RT}) \tag{5.8}$$

where, ΔS and ΔH are the entropy and enthalpy changes respectively. For conduction due to holes (the predominant charge carriers), combining equations (5.5) and (5.8) yields:

$$\sigma = 6^{\frac{1}{4}} P_{O_2}^{\frac{3}{16}} e^{+} \mu_p \exp(\frac{\Delta S_{5.6}}{8R} - \frac{\Delta H_{5.6}}{8RT}) \tag{5.9}$$

At any temperature, assuming mobility to be independent of the change in the concentration of ionized cation vacancies, conductivity should vary as the 3/16 power of P_{O_2}, which is in agreement with the experimental data in this region.

The enthalpy of the above oxidation reaction can also be calculated from the Arrhenius plot of conductivity vs. the reciprocal of absolute temperature. Figure 5.16 is such a plot, which shows the temperature dependence of conductivity for six P_{O_2} values. The slopes of these lines equal $\frac{-\Delta H_{5.6}}{8R}$ (Table 5.4) and hence, the activation enthalpies can be evaluated as listed in Table 5.5. These values ranged from 165.64 Kcal/mole to 168.58 Kcal/mole and remained essentially unchanged with P_{O_2}, consistent with the linear relationship between conductivity and P_{O_2} in this region. These activation enthalpy values have not been

Table 5.4

SLOPES OF ARRHENIUS PLOTS IN THE HIGH P_{O_2} REGION

P_{O_2} (atm.)	$-\dfrac{\Delta \ln\sigma}{\Delta(10^{-3}/T)}$
10^{0}	10.567
2.1×10^{-1}	10.605
5×10^{-2}	10.476
10^{-2}	10.475
10^{-3}	10.420
10^{-4}	10.513

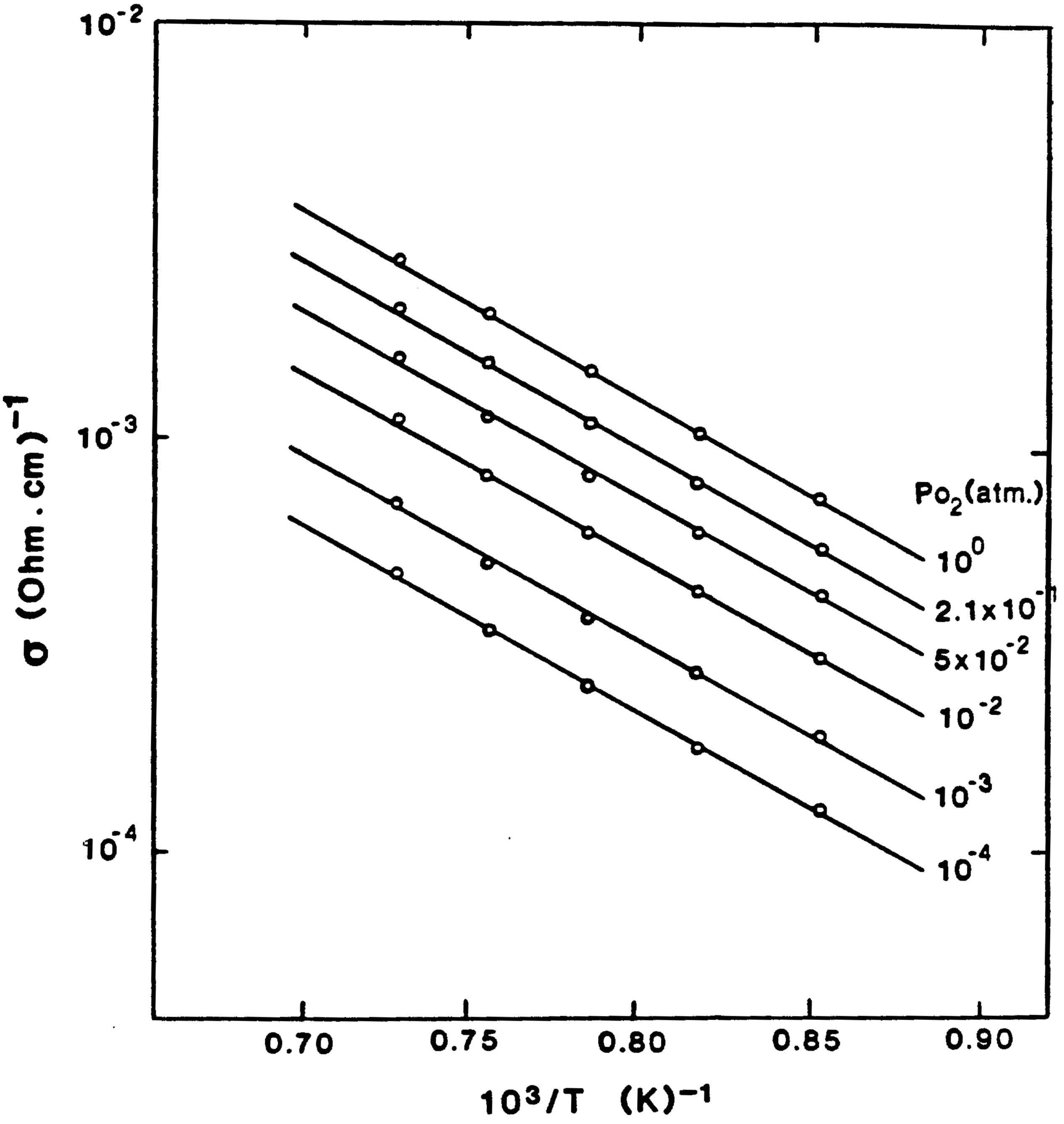

Figure 5-16: TEMPERATURE DEPENDENCE OF CONDUCTIVITY OF $SrZrO_3$ IN THE P_{O_2} REGION 10^0-10^{-4} ATM.

Table 5.5

ACTIVATION ENTHALPIES FOR CONDUCTION IN THE HIGH P_{O_2} REGION

P_{O_2} (atm.)	Activation Enthalpies (Kcal/mole)
10^0	167.98
2.1×10^{-1}	168.58
5×10^{-2}	166.53
10^{-2}	166.51
10^{-3}	165.64
10^{-4}	167.12

corrected for any temperature effect on the mobility of the charge carriers, since mobility- temperature relationships were not noted in this investigation and no other published data is available on the temperature dependency of mobility of the charge carriers in this system, over the temperature range of interest.

In the intermediate P_{O_2} region (10^{-7}–10^{-15} atm.), conductivity again decreased with decreasing P_{O_2} and temperature. It decreased linearly as the 1/4 power of P_{O_2} at all temperatures. The actual values of the slopes of these lines are listed in Table 5.6 and varied from 1/4.17 to 1/4.47. In this region, the electrical neutrality condition (equation 1.35) can be simplified into either the condition represented by equation (1.38), viz., $[n] \approx [p]$ or the condition represented by equation (1.39), viz., $[V_O^{\cdot\cdot}] = [V_A^{''}]+[V_B^{''''}]$, depending upon whether the ionization reaction involving electrons and holes or the Schottky reaction which generates vacancies in oxygen and cation sites is operative, as indicated by the higher equilibrium constant for the dominant reaction. Comparing the experimental results with Figure 1.2 and Table 1.3, it can be concluded that the simplified neutrality condition for this region is the one given by equation (1.39), corresponding to the Schottky reaction. However, the simultaneous existence of vacancies of oxygen and both cation sites is highly unlikely. Further, the oxidation reaction that is applicable in this intermediate P_{O_2} region is:

$$V_O^{\cdot\cdot}+\frac{1}{2}O_2 = O_O+2p \tag{5.10}$$

The above reaction indicates that any residual vacant oxygen sites in the lattice would be neutralized by the incorporation of oxygen from the atmosphere. However, the presence of oxygen vacancies can be accounted for if an alternative explanation is considered as in similar investigations involving undoped $BaTiO_3$

Table 5.6

P_{O_2} DEPENDENCE OF CONDUCTIVITY IN THE REGION 10^{-7}–10^{-15} ATM.

Temperature (K)	m for $\sigma_p \alpha P_{O_2}{}^{1/m}$
1173	4.17
1223	4.30
1273	4.25
1323	4.47
1373	4.38

and $SrTiO_3$ systems (81-83). In these studies, a defect model which emphasized the role of impurities was suggested, based on the fact that for currently available purities, there is invariably a net excess of acceptor - type impurities, in amounts that exceed the concentrations of defects resulting from any type of intrinsic ionic or electronic disorder. Acceptor impurities are substitutional metallic species that have a lower ionic charge than the ions which they replace and are compensated by a corresponding number of oxygen vacancies. The impurity content is generally dominated by acceptors, because they have much greater natural elemental abundances than the more highly charged species which behave as donors. It is possible that the $SrZrO_3$ samples in this study also contain some acceptor impurities (probably Al or Fe from experimental equipment contamination) which are singly ionized. The theoretical treatment would then correspond to the one given in Section 1.3 for acceptor impurities. Comparison of experimental results with Figure 1.4 and Table 1.5 indicates that the variation of conductivity as the 1/4 power of P_{O_2} in this region can be accounted for if the corresponding simplified neutrality condition is :

$$2[V_O^{\cdot\cdot}] = A' \tag{5.11}$$

For the oxidation reaction in this region (equation 5.10), the equilibrium constant is :

$$K_{5.10} = [p]^2/[V_O^{\cdot\cdot}]P_{O_2}^{\frac{1}{2}} = \exp(\frac{-\Delta G_{5.10}}{RT}) \tag{5.12}$$

Combining the above equation with the simplified neutrality condition (equation 5.11), and resolving the free energy term into the entropy and enthalpy components,

$$p = [V_O^{\cdot\cdot}]^{\frac{1}{2}}P_{O_2}^{\frac{1}{4}}\exp(\frac{\Delta S_{5.10}}{2R} - \frac{\Delta H_{5.10}}{2RT}) \tag{5.13}$$

Again, for the case where holes are the predominant charge cariers, combining equation (5.13) and (5.5) conductivity can be expressed as :

$$\sigma = [V_O^{\cdot\cdot}]^{\frac{1}{2}} P_{O_2}^{\frac{1}{4}} e^{+} \mu_P \exp(\frac{\Delta S_{5.10}}{2R}) \exp(\frac{-\Delta H_{5.10}}{2RT}) \tag{5.14}$$

The above reaction predicts that conductivity varies as the 1/4 power of P_{O_2}, consistent with the experimental results. Also, these results are similar to those obtained for $BaTiO_3$ (81,82,84), $SrTiO_3$ (83) and $LaFeO_3$ (85) samples subjected to a high P_{O_2} environment. The Arrhenius plots (Figure 5.17) of log conductivity vs. the reciprocal of absolute temperature at nine P_{O_2} values were used to calculate the activation enthalpies, as before, for the conduction reaction. The slopes of the lines $(= -\frac{\Delta H_{5.10}}{2R})$, listed in Table 5.7 were nearly consistent, yielding enthalpy values of 39.24 Kcal/mole to 50.34 Kcal/mole (Table 5.8). These values are lower than those listed in Table 5.5. However, the actual slopes of the lines in Figure 5.17 are very nearly the same as those in Figure 5.16, that is, $\frac{\Delta H_{5.8}}{8R} \approx \frac{\Delta H_{5.10}}{2R}$.

Before the above explanation is accepted for the conductivity behavior of $SrZrO_3$ in this study, the discrepancies involved should be examined. Examination of Figure 1.4 reveals a region, corresponding to a neutrality condition of $[I_m'] = [p]$, where conductivity is invariant.This region lies between the high P_{O_2} region where conductivity varies as the 3/16 power of P_{O_2} and the intermediate P_{O_2} region where it varies as the 1/4 power of P_{O_2}. However, this conductivity invariant region was not observed in this study. Hence, although the above explanation, based on an acceptor impurity effect, can account for the presence of oxygen vacancies, the treatment of the P_{O_2} range as two separate regions (10^{0}–10^{-4} atm. and 10^{-7}–10^{-15} atm.) may not be valid.

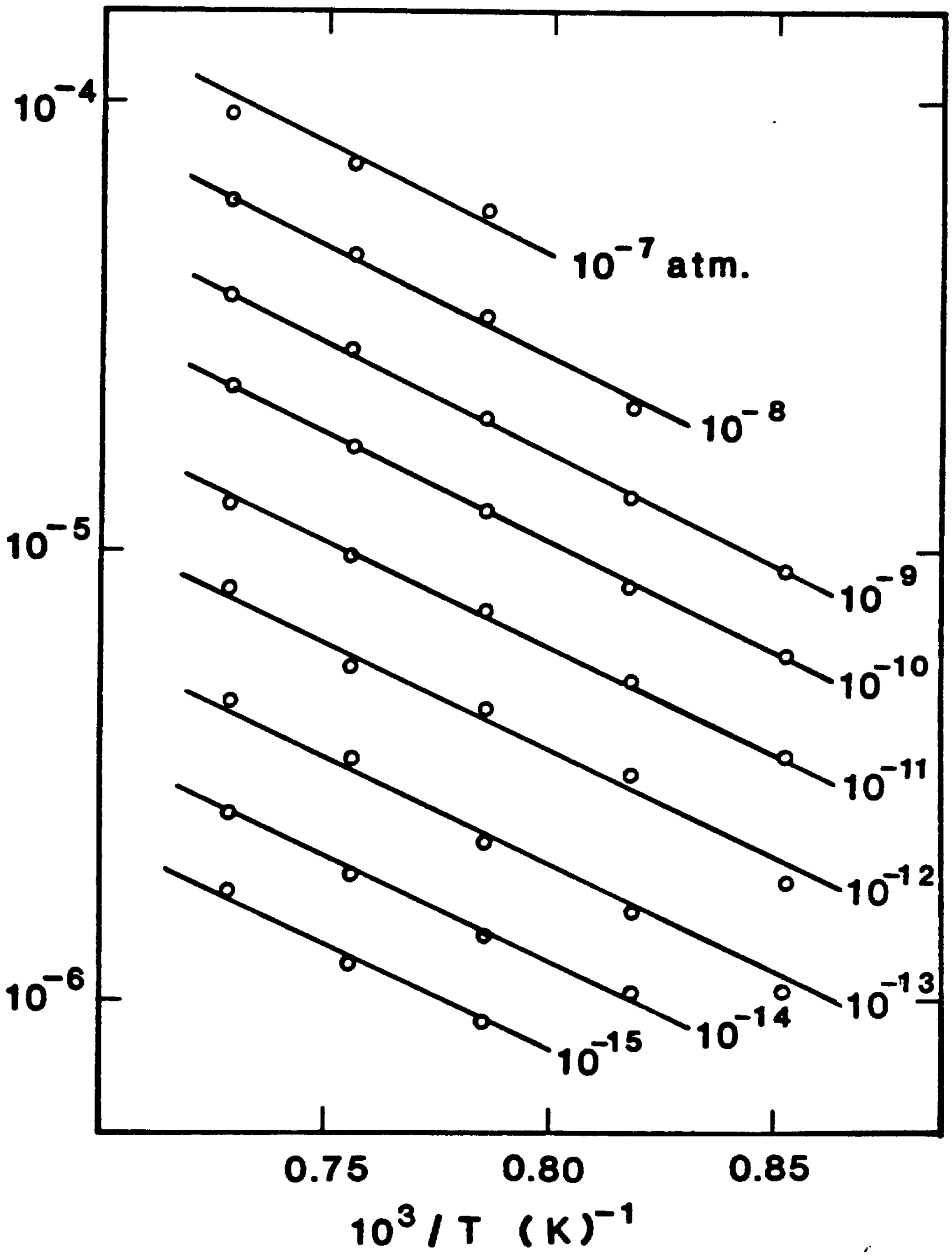

Figure 5-17: TEMPERATURE DEPENDENCE OF CONDUCTIVITY OF $SrZrO_3$ IN THE P_{O_2} REGION 10^{-7}–10^{-15} ATM.

Table 5.7

SLOPES OF ARRHENIUS PLOTS IN THE P_{O_2} REGION 10^{-7}–10^{-15} ATM.

P_{O_2} (atm.)	$-\frac{\Delta \ln \sigma}{\Delta(10^{-3}/T)}$
10^{-7}	11.177
10^{-8}	10.432
10^{-9}	12.667
10^{-10}	11.660
10^{-11}	11.363
10^{-12}	9.873
10^{-13}	10.059
10^{-14}	10.246
10^{-15}	11.363

Table 5.8

ACTIVATION ENTHALPIES FOR CONDUCTION IN THE P_{O_2} REGION 10^{-7}–10^{-15} ATM.

P_{O_2} (atm.)	Activation Enthalpies (Kcal/mole)
10^{-7}	44.42
10^{-8}	41.46
10^{-9}	50.34
10^{-10}	46.34
10^{-11}	45.16
10^{-12}	39.24
10^{-13}	39.98
10^{-14}	40.72
10^{-15}	45.16

Case 2 (Figure 5.15): Straight lines in Figure 5.15 were drawn through the experimental points, treating the entire P_{O_2} range as a single region (the scatter in the data points were within experimental errors involved in measurement). The slopes of these lines (listed in Table 5.9) were very nearly 1/4. As in case 1, an acceptor impurity effect is invoked to explain the pressure of oxygen vacancies, which, in turn, accounts for the conductivity variation. As before, the oxidation reaction involving oxygen atoms from gas phase occupying the oxygen vacancies (equation 5.10), together with the simplified neutrality condition (equation 5.11) yield the ultimate result :

$$\sigma = [V_O^{\cdot\cdot}]^{\frac{1}{2}} P_{O_2}{}^{\frac{1}{4}} e^{+} \mu_p exp(\frac{\Delta S_{5.10}}{2R}) \exp(\frac{\Delta H_{5.10}}{2RT}) \qquad (5.14)$$

The above condition predicts that conductivity varies as the 1/4 power of P_{O_2}, which is in good agreement with the experimental results, although towards higher P_{O_2} values, the slopes were closer to 3/16. As described earlier, the activation enthalpies for the above reaction were calculated through Arrhenius plots (Figure 5.18). The values, as indicated in Table 5.10 range from 40.99 Kcal/mole to 45.29 Kcal/mole.

As mentioned in the beginning of this section, there are few published references on the electrical conductivity of pure $SrZrO_3$ in the temperature and pressure ranges of interest. Pivovar and Tolstaya-Belik (28) studied the conductivity of this system at higher temperatures and in air. Examination of their curves at the lower end of temperature of investigation (about 1273 - 1373 K), indicates conductivity values in the range of 5×10^{-8} (ohm. cm)$^{-1}$, which are considerably lower than the values obtained in this investigation and elsewhere (29-32,34). Anthony and Foex (33) also studied this system at higher temperatures and in air and compared the conductivities of pure and commercial grades of $SrZrO_3$. At 1373 K, the lower end of investigation, the conductivity values

Table 5.9

P_{O_2} DEPENDENCE OF CONDUCTIVITY IN THE REGION 10^0-10^{-15} ATM.

Temperature (K)	m for $\sigma_p \alpha P_{O_2}{}^{1/m}$
1173	4.54
1223	4.53
1273	4.56
1323	4.53
1373	4.57

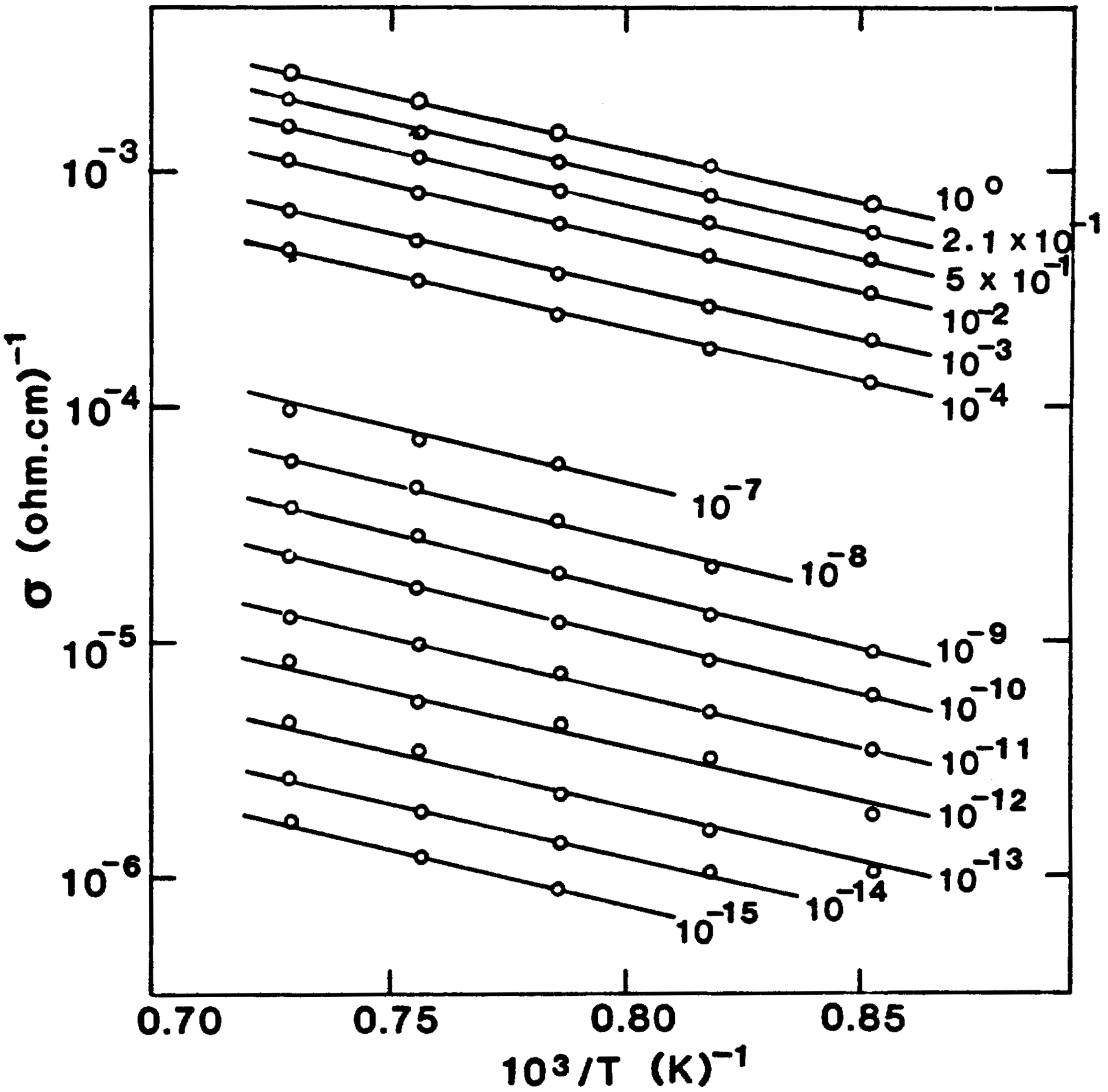

Figure 5-18: TEMPERATURE DEPENDENCE OF CONDUCTIVITY OF $SrZrO_3$ IN THE P_{O_2} REGION 10^0-10^{-15} ATM.

Table 5.10

ACTIVATION ENTHALPIES FOR CONDUCTION IN THE P_{O_2} REGION 10^0–10^{-15} ATM.

P_{O_2} (atm.)	Activation Enthalpies (Kcal/mole)
10^0	41.63
2.1×10^{-1}	42.27
5×10^{-2}	42.00
10^{-2}	41.54
10^{-3}	40.99
10^{-4}	41.27
10^{-7}	44.19
10^{-8}	44.47
10^{-9}	45.02
10^{-10}	45.29
10^{-11}	43.74
10^{-12}	42.18
10^{-13}	42.55
10^{-14}	42.10
10^{-15}	43.83

reported for the pure sample were about $5\times10^{-5}(ohm.\ cm)^{-1}$, a value close to that observed by Anthony et al (29). The data of Longo et al (30,32,34) shows a consistent half order of magnitude difference from the conductivity values obtained in this study, in the temperature range of 1173 - 1373 K and P_{O_2} range of $10^0-5\times10^{-6}$ atm. Although slope values have not been calculated, examination of their data shows very good agreement with the results obtained in this study for these temperature and pressure ranges. The higher conductivity values observed in this investigation may be due to the specimen preparation method. In the liquid mix method that was used in this study, better homogenization and thorough mixing (on an atomic scale) of the constituent elements are possible when compared with the mechanical mixing involved in the other studies. With regards to activation enthalpies, Anthony et al (29) reported a value of 36 Kcal/mole in the temperature range of 1273 - 1673 K and at a P_{O_2} value of 2.1×10^{-1} atm. Pivovar and Tolstaya-Belik (28) reported a value of 44 Kcal/mole at a P_{O_2} value of 2.1×10^{-1} atm. and over a temperature range of 1373 - 1973 K, with a small increase in the enthalpy value, with an increase in porosity. They hypothesized that the conductivity in this compound was, probably, purely intrinsic. Comparison with the present work suggests that this value could also be associated with the oxidation reaction, represented by equation (5.10). Anthony and Foex (33) measured conductivity above 1723 K and in air. Extrapolation of their data to lower temperatures yields a value of 33 Kcal/mole for the activation enthalpy, using the oxidation reaction in equation (5.10). Longo et al (30,32,34) investigated the variation of conductivity of $SrZrO_3$ over a temperature range of 1073 - 1473 K and observed a linear relationship. At a P_{O_2} value of 2.1×10^{-1} atm., they calculated the activation energy to be 2.64 eV (61.4 Kcal/mole) using equation (5.10). The agreement between all the above investigations and the present work, is generally good.

5.4 Electrical Conductivity of La-doped $SrZrO_3$

The effect of La addition, as a donor impurity, upon the equilibrium electrical conductivity of polycrystalline $SrZrO_3$, was also determined in this study. Electrical conductivity values of La-doped $SrZrO_3$, as a function of P_{O_2} ($10^{-19} \leq P_{O_2} \leq 10^0$ atm.) and temperature (1173 - 1373 K) are shown in Figures 5.19 and 5.20 for La concentrations of 0.05 at.% and 0.1 at.%, respectively.

For the 0.05 at.% La-doped sample, a conductivity minimum was observed in these curves. In the high P_{O_2} region, conductivity of this doped compound increased with increasing P_{O_2}, suggesting that p-type electronic conduction is predominant. In the lower P_{O_2} region, conductivity decreased with increasing P_{O_2}, indicating that the electronic conduction is essentially n-type. The slopes of the curves are listed in Tables 5.11 and 5.12.

To explain the variation of conductivity in the high P_{O_2} region, the following reaction is considered :

$$2La_{Sr}^{\cdot} + Sr_{Sr} + \frac{1}{2}O_2 = SrO + 2La_{Sr}^{\cdot} + V_{Sr}'' + 2p \qquad (5.2)$$

As explained in Section 5.2, the extra charge of lanthanum can be compensated by a lattice defect. The main compensation mechanism considered here is the strontium vacancy model. The additional strontium atoms that result from the strontium vacancies, combine with oxygen to form SrO layers, which can be built into the lattice in an ordered fashion.

Applying the quasi-chemical mass action relation to equation (5.2), the equilibrium constant can be expressed as:

$$K_{5.2} = \frac{[V_{Sr}''][p]^2}{P_{O_2}^{\frac{1}{2}}} \qquad (5.15)$$

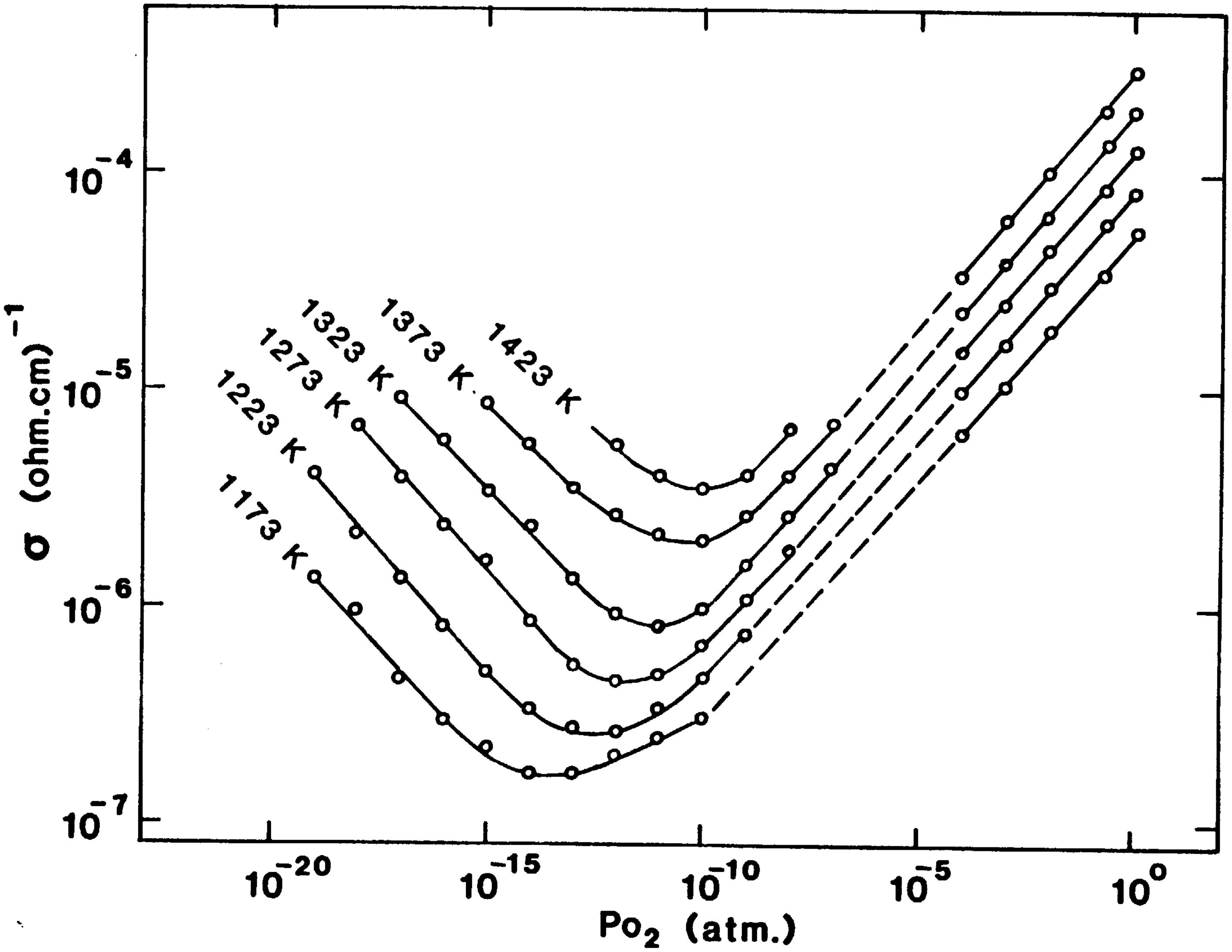

Figure 5-19: ELECTRICAL CONDUCTIVITY OF 0.05 AT.% *La*- DOPED $SrZrO_3$ AS A FUNCTION OF P_{O_2}

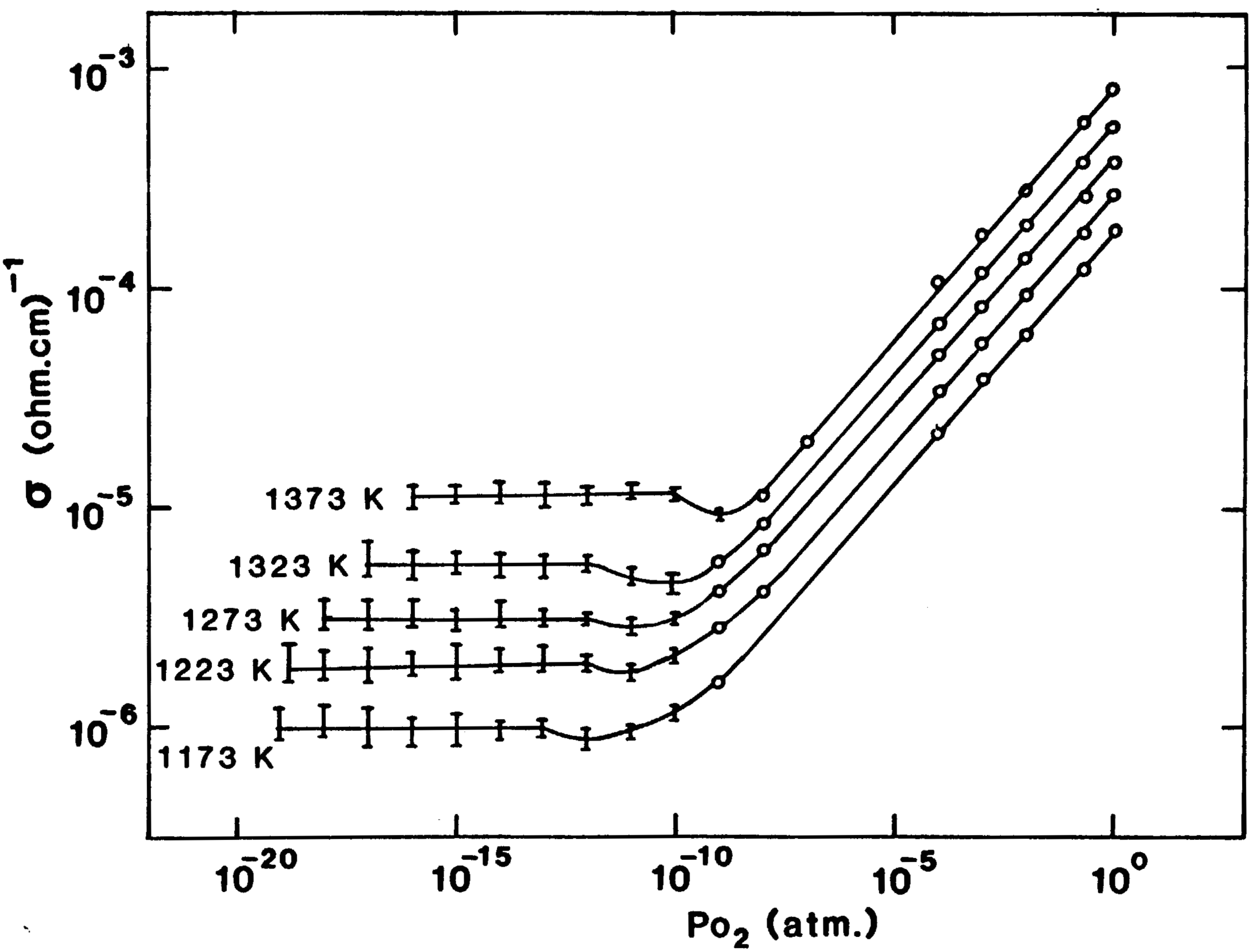

Figure 5-20: ELECTRICAL CONDUCTIVITY OF 0.10 AT.% *La*-DOPED $SrZrO_3$ AS A FUNCTION OF P_{O_2}

Table 5.11

P_{O_2} DEPENDENCE OF CONDUCTIVITY IN THE REGION 10^0–10^{-7} ATM. FOR 0.05 AT.% *La*-DOPED $SrZrO_3$

Temperature (K)	m for $\sigma_p \alpha P_{O_2}{}^{1/m}$
1173	4.25
1223	4.35
1273	4.28
1323	4.26
1373	4.30

Table 5.12

P_{O_2} DEPENDENCE OF CONDUCTIVITY IN THE REGION 10^{-13}–10^{-18} ATM. FOR 0.05 AT.% *La*-DOPED $SrZrO_3$

Temperature (K)	m for $\sigma_n \alpha P_{O_2}{}^{1/m}$
1173	- 4.54
1223	- 4.44
1273	- 4.49
1323	- 4.84
1373	- 4.98

The donor dopant is compensated ionically by metal deficiency (22,86) at high oxygen activities. This means that,

$$[La^{\cdot}] = 2[V_{Sr}''] = constant \tag{5.16}$$

Combining the above equations,

$$p \; \alpha \; P_{O_2}^{\frac{1}{4}} \tag{5.17}$$

and thus,

$$\sigma \; \alpha \; P_{O_2}^{\frac{1}{4}} \tag{5.18}$$

The n-type behavior in the low P_{O_2} region can be explained by considering the same oxidation reaction and neutrality condition as in the high P_{O_2} region. However, in this region, the ionization is such that the concentration of electrons is higher than that of holes, accounting for the conductivity variation as -1/4 power of P_{O_2}.

These results are consistent with the experimental results, and explain well the observed P_{O_2} dependency of conductivity.

From the minima in the conductivity at n - p transition, the band gap energy (E_g^0) of the compound can also be obtained following the method of Becker and Frederikse (87). The Arrhenius plot of conductivity minima vs. the reciprocal of absolute temperature is shown in Figure 5.21. Assuming band - conduction for both electrons and holes, the full expression for the Arrhenius plot is given by:

$$\frac{\partial \ln \sigma_{min}}{\partial (RT)^{-1}} = \frac{\partial}{\partial (RT)^{-1}}\left[\frac{\ln \mu_n \mu_p}{2} + \ln N_c \ln N_v\right] - \frac{E^0_g}{2} \tag{5.19}$$

where μ_n and μ_p are the mobilities of eletrons and holes and N_c and N_v are the densities of states near the band edges for conduction band and valence band

Table.5.13

P_{O_2} DEPENDENCE OF CONDUCTIVITY IN THE REGION 10^0-10^{-8} ATM. FOR 0.1 AT.% La-DOPED $SrZrO_3$

Temperature (K)	m for $\sigma_p \alpha P_{O_2}{}^{1/m}$
1173	4.39
1223	4.53
1273	4.59
1323	4.61
1373	4.54

respectively. The Arrhenius slope is directly proportional to the band gap energy, because, mobilities vary proportional to $T^{-3/2}$ and densities of states vary proportional to $T^{+3/2}$, and thus these two terms cancel each other.

The actual value of the band gap energy, calculated from the slope of the Arrhenius curve in Figure 5.21 was about 3.4 eV. This result is consistent with the value of about 3 eV., obtained by Budim and Kozyreva (38), using the method of diffusion reflection spectra. An interesting observation here is the fact that, when the band gap energy of these zirconate samples are compared with the more readily available data for titanates (88-90), the actual values are remarkably similar. This is because the absorption limit is mainly due to deformation of a similar type of octahedra (ZrO_3 or TiO_3), that is, due to transitions of electrons from filled oxygen states to free 4d states of zirconium or 3d states of titanium (91). The zirconate and titanate samples have approximately equal degrees of band covalence and identical crystal structures. The small differences in the band gap energy are due to the fact that the the forbidden zone width varies with such properties as interatomic distance, elasticity constant, melting point and Debye temperature (92-93) and these properties are slightly different for these samples. Also the activation energy for conduction is a function of crystalline structure and deviation from ideality and modification of the structure may lead to a change in the band gap, by introducing distortion in the material (31). Similar to the results of this study, Longo and Ricciardiello (31) also found the process of conduction to be dependent upon the major tetravalent cation.

For the 0.1 at.% La-doped samples, the plot of log conductivity vs. log P_{O_2} is shown in Figure 5.20. Error bars are also indicated in the low P_{O_2} region and the average conductivity at each P_{O_2} value was computed from at least six measurements. As before, p-type behavior was observed in the high P_{O_2} region. At low

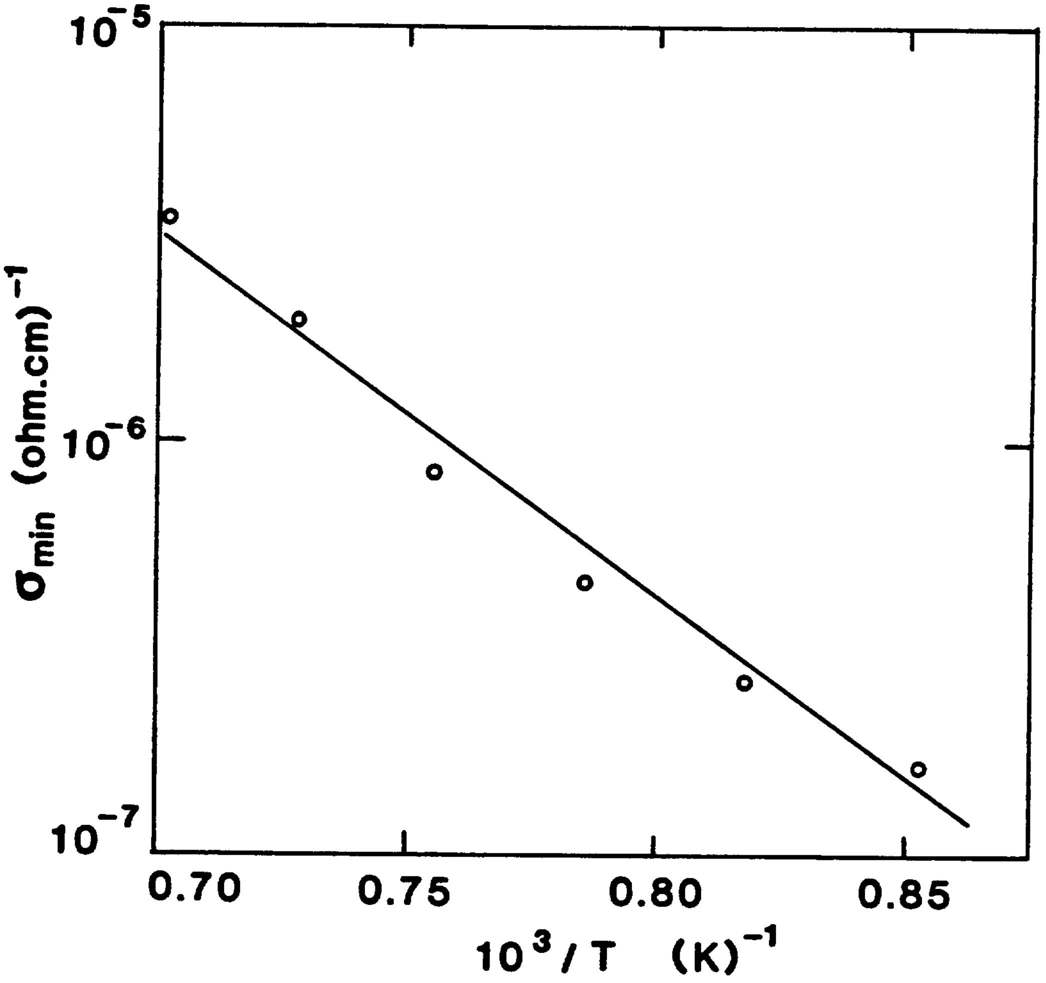

Figure 5-21: TEMPERATURE DEPENDENCE OF THE CONDUCTIVITY MINIMA OF 0.05 AT.% *La*-DOPED $SrZrO_3$

P_{O_2} values, conductivity was independent of P_{O_2}. The absolute value of conductivity in the p-type region was lower when compared with undoped $SrZrO_3$. The calculated slopes in the high P_{O_2} region is listed in Table 5.13.

The variation of conductivity in the high P_{O_2} region can be explained in the same way as for the 0.05 at.% La-doped samples. In the low P_{O_2} region, the following reaction is considered:

$$La_2O_3 = 2La^{\cdot}_{Sr} + 2n + 2O_O + \frac{1}{2}O_2 \tag{5.20}$$

Charge compensation by an extra electron is expected according to this equation. The equilibrium constant $K_{5.20}$ for this reaction is given by:

$$K_{5.20} = [La_{Sr}^{\cdot}]^2[n]^2 P_{O_2}^{\frac{1}{2}} \tag{5.21}$$

The neutrality condition in this region is:

$$[La^{\cdot}] = [n] = constant \tag{5.22}$$

This implies that conductivity is also independent of P_{O_2}.

The above explanations (for both the 0.05 at.% and 0.1 at.% La-doped samples) are, in general, consistent with the theoretical considerations in Section 1.3 for an ABO_3 compound, containing donor impurities (Figure 1.3). However, in the 0.1 at.% La-doped samples, the n-type region between the p-type and the conductivity invariant regions is not readily apparent. It is possible that at higher donor concentrations, this region exists over narrower P_{O_2} ranges. In fact a very small n-type region can be discerned upon closer examination. A similar effect was observed in $LaFeO_3$ system by Mizusaki et al (85). Also, as seen from the error bars in Figure 5.20 (0.1 at.% curve), measurement of conductivity at lower P_{O_2} values at this La concentration is difficult (due to stability problems) and often inconsistent readings are obtained.

Although in both the 0.05 at.% and 0.1 at.% La-doped samples, the absolute values of conductivity in the p-type region were lower than the corresponding values for undoped $SrZrO_3$, when compared with each other, the 0.1 at.% La-doped samples exhibited a half order of magnitude higher values. Since donor (La) impurity should lower the concentration of holes, the above result seems to be inconsistent with theory. This discrepancy may be due to a grain size effect. The grain size, as a function of La concentration, is shown in Figures 5.22 and 5.23. Grain size increased consistently with increasing amount of La, that is, the grain boundary area decreased with increasing La. The reason for the higher conductivity values for the 0.1 at.% La-doped sample is thus probably due to the domination of this grain size effect (94,95). Other investigators have also observed a similar effect and ascribed this to the existence of a high resistivity or blocking layer in the grain boundary regions (96-99). Even in the absence of such a layer, this effect has been identified, as in the case of β-alumina, which is an alkali-ion conductor (100,101).

An attempt was made in this study to obtain conductivity data for 1.0 at.% La-doped samples. At this La concentration, the conductivity values in the p-type region were considerably lower than for either the 0.05 or 0.1 at.% La-doped samples, indicating that the grain boundary effect was no longer dominant. Thus, this effect can be considered only when small amounts of dopant are present, that is, when variation in the La concentration between the samples are small. Similar conclusions were drawn by Wang and Nowick (102) who observed this effect to a significant extent only at low dopant concentrations. They also found higher activation enthalpy for conduction at grain boundaries (when compared with the bulk and also that the grain boundary conductivity was more susceptible to reduction than the lattice. They explained these effects on the basis that the grain boundaries were regions of high purity (with respect to the

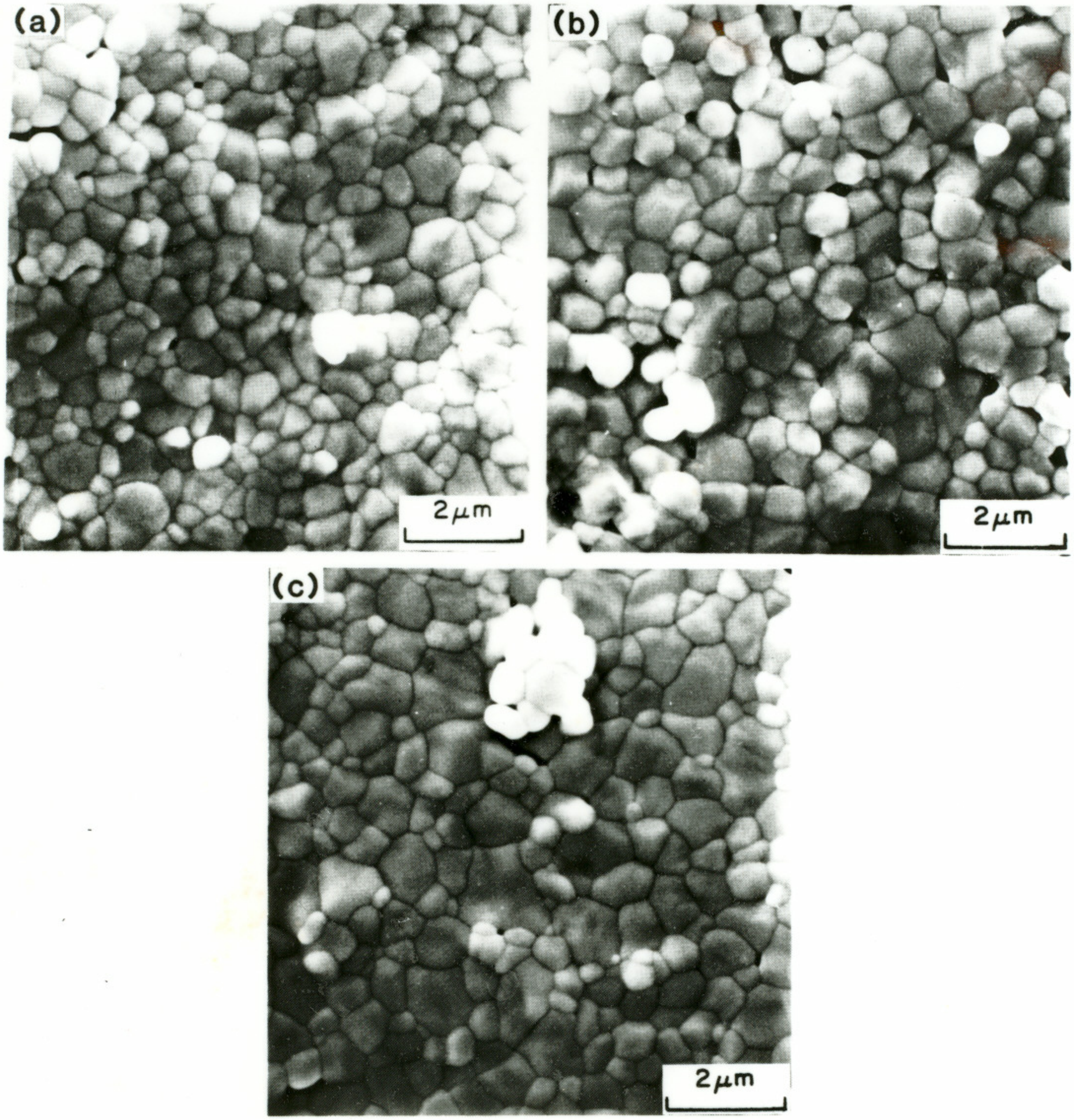

Figure 5-22: GRAIN SIZE OF $SrZrO_3$ AS A FUNCTION OF *La* CONCENTRATION:

a) 0 at.% *La*

b) 0.05 at.% *La*

c) 0.10 at.% *La*

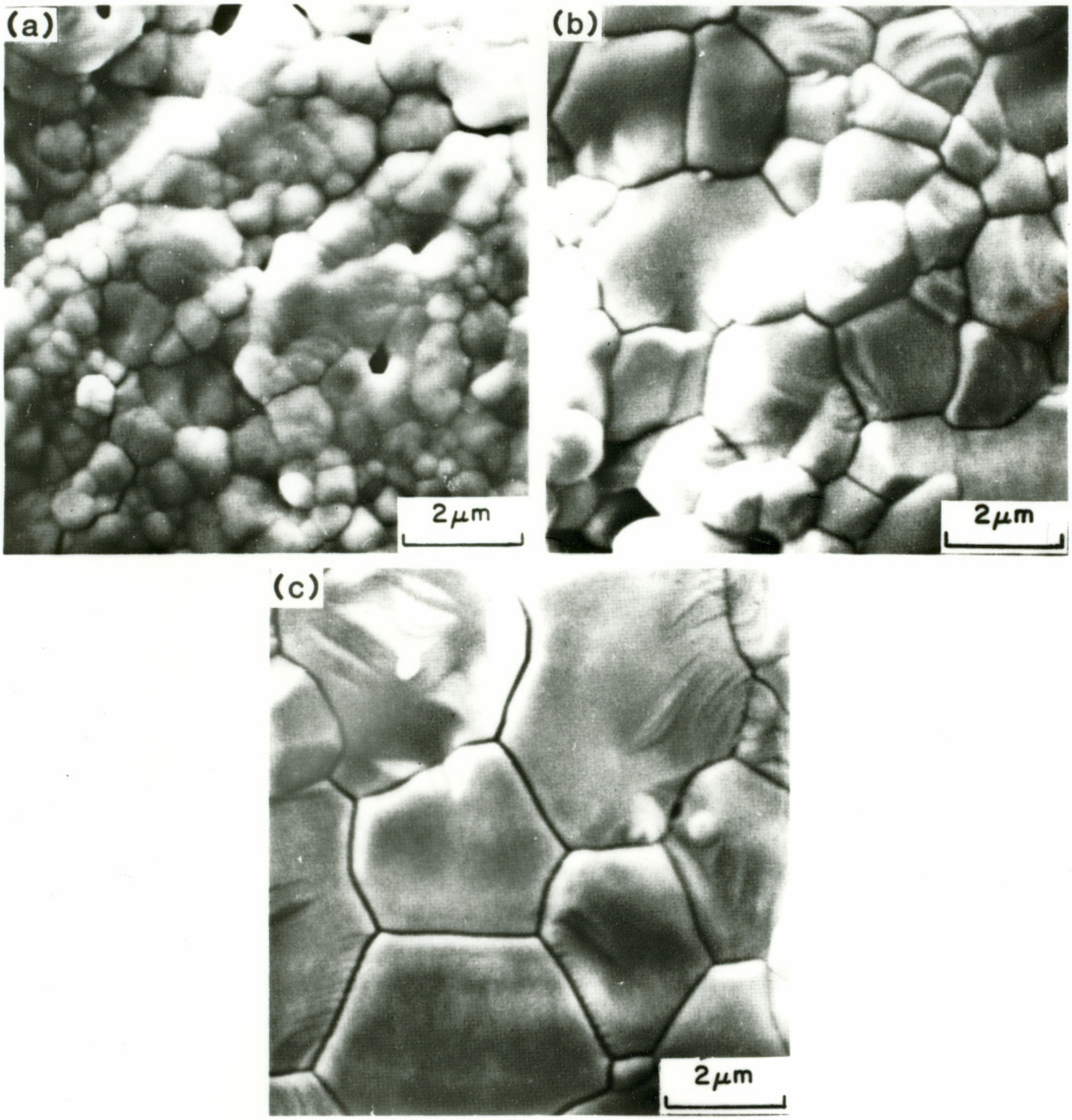

Figure 5-23: GRAIN SIZE OF $SrZrO_3$ AS A FUNCTION OF La CONCENTRATION:

a) 2 at.% La
b) 4 at.% La
c) 6 at.% La

dopant) than the lattice due to the scavenging action of the dopant in these regions by impurities (like naturally present acceptor type impurities), rather than due to the presence of any second phases at the grain boundaries. Since in the case of 1.0 at.% La-doped samples only erratic reading were obtained and repeatability was poor, the conductivity data are not reported here. In addition, associated with the grain size effect is the effect of density which increases with increasing La concentration due to a reduction in the grain boundary area. This, in turn, would lead to a higher value for the 0.1 at.% La-doped samples when compared with the 0.05 at.% La-doped samples.

For both the 0.05 at.% and 0.1 at.% La-doped samples, the activation enthalpies for the conduction reaction in the p-type region were calculated from the Arrhenius plots of log conductivity vs. reciprocal of absolute temperature (Figures 5.24 - 5.26) and the values are listed in Tables 5.14-5.16.

5.5 Chemical Diffusion Coefficient in Undoped $SrZrO_3$

Figure 5.27 shows representative transient electrical conductivity data (log σ vs. t) obtained at 1323 K. The sample was initially equilibrated at a P_{O_2} value of 10^{-4} atm. The P_{O_2} value was then changed and the conductivity increased to the new equilibrium value. Subsequently, the original P_{O_2} value of 10^{-4} atm. was re-established over the sample and the conductivity decreased to the original value. As shown in the figure, the four intermittent P_{O_2} values were 10^{-3} atm., 10^{-2} atm., 5×10^{-2} atm. and 2.1×10^{-1} atm. respectively. The equilibrium value of conductivity increased with an increase in the P_{O_2} value. Similar plots were obtained at other temperatures, as shown in Figures 5.28-5.30. However, the conductivity values were lower and the equilibrium conductivity values were achieved at longer times at lower temperatures for a given P_{O_2} value. To

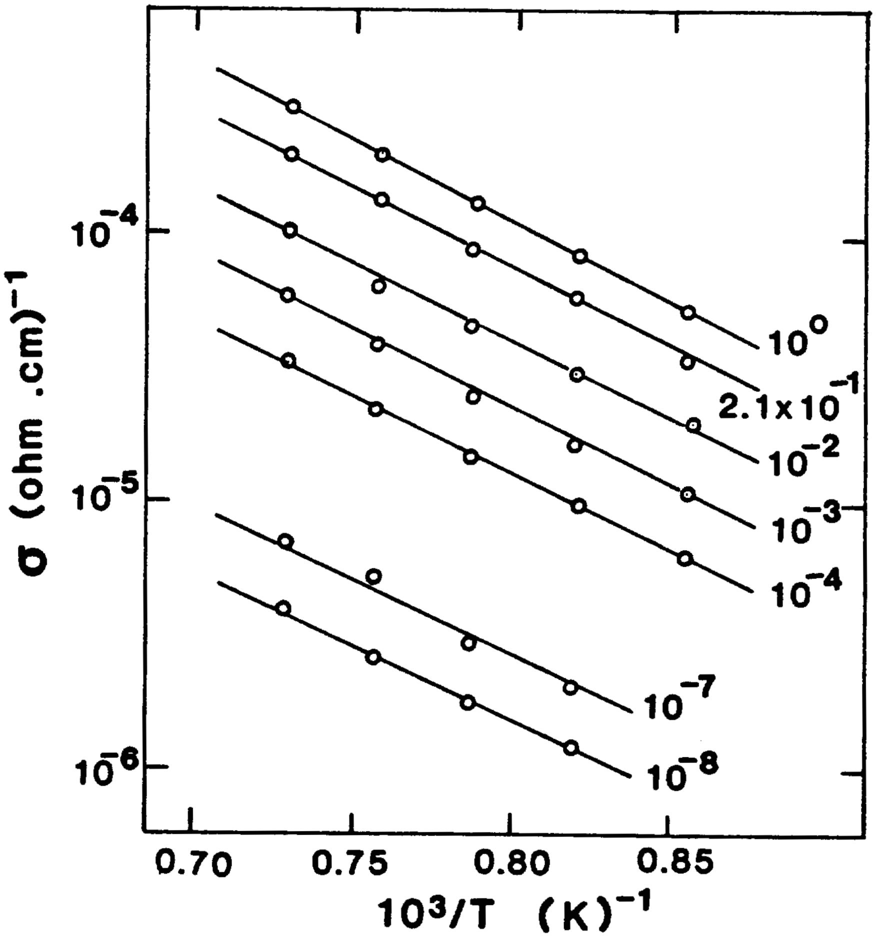

Figure 5-24: TEMPERATURE DEPENDENCE OF CONDUCTIVITY OF 0.05 AT.% *La*-DOPED $SrZrO_3$ IN THE P_{O_2} REGION 10^0-10^{-8} ATM.

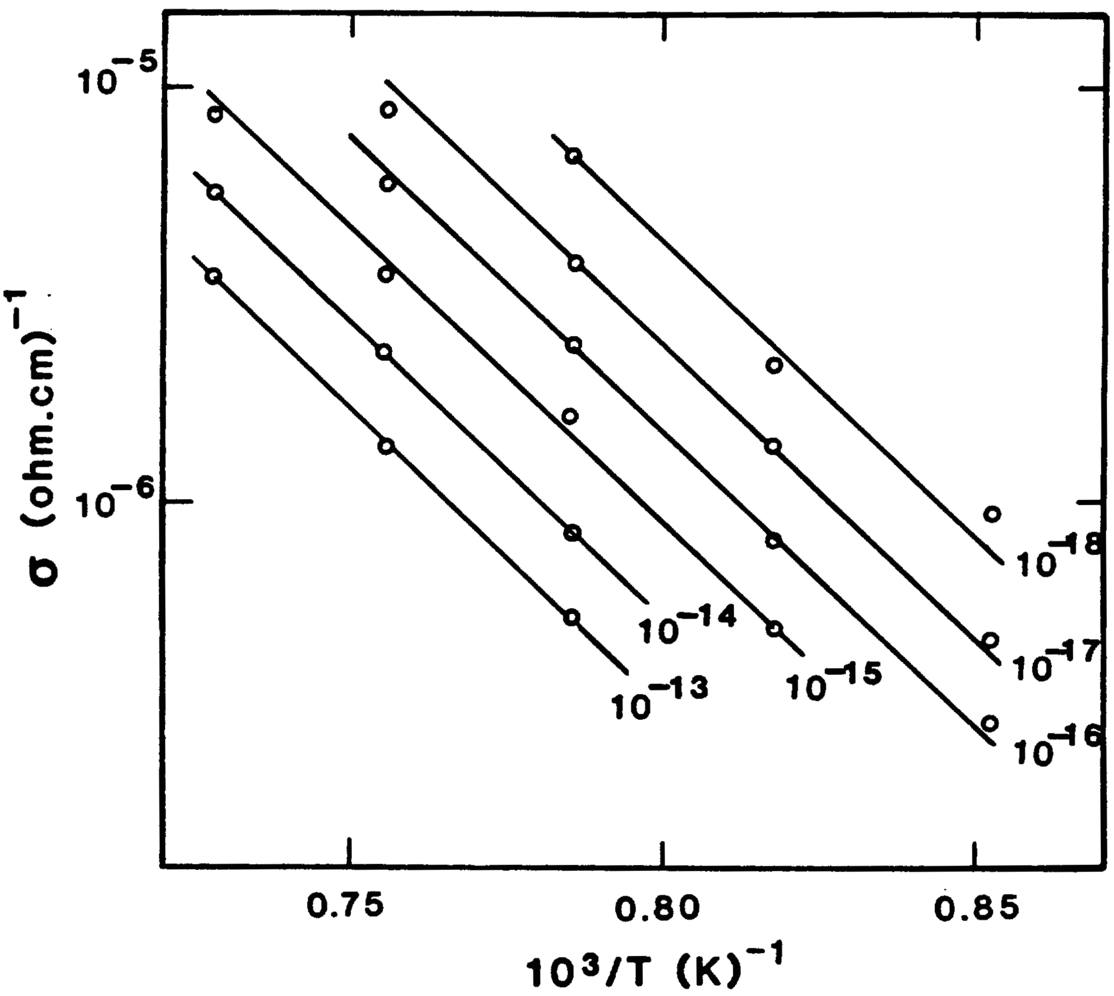

Figure 5-25: TEMPERATURE DEPENDENCE OF CONDUCTIVITY OF 0.05 AT.% *La*-DOPED $SrZrO_3$ IN THE P_{O_2} REGION 10^{-13}–10^{-18} ATM.

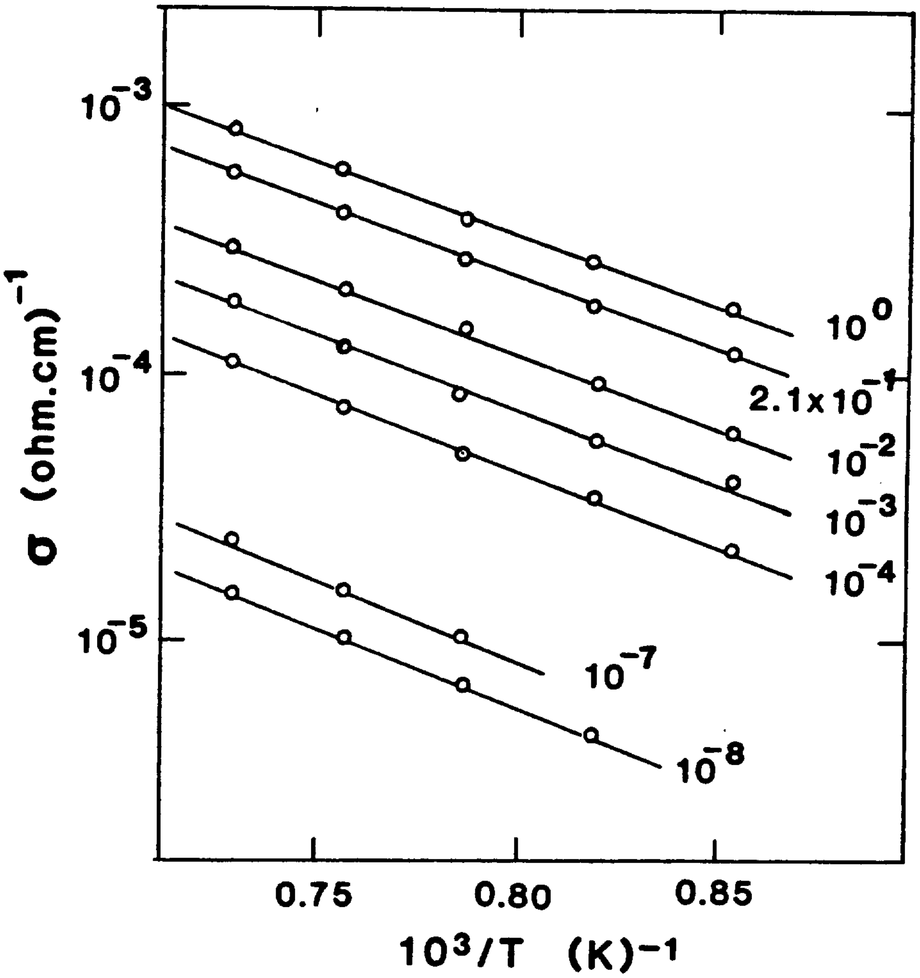

Figure 5-26: TEMPERATURE DEPENDENCE OF CONDUCTIVITY OF 0.10 AT.% *La*-DOPED $SrZrO_3$ IN THE P_{O_2} REGION 10^0-10^{-8} ATM.

Table 5.14

ACTIVATION ENTHALPIES FOR CONDUCTION IN THE HIGH P_{O_2} REGION FOR 0.05 AT.% *LA*-DOPED $SrZrO_3$

P_{O_2} (atm.)	Activation Enthalpies (Kcal/mole)
10^0	55.26
2.1×10^{-1}	56.02
10^{-2}	52.31
10^{-3}	56.73
10^{-4}	51.20
10^{-7}	54.76
10^{-8}	53.22

Table 5.15

ACTIVATION ENTHALPIES FOR CONDUCTION IN THE LOW P_{O_2} REGION FOR 0.05 AT.% La-DOPED $SrZrO_3$

P_{O_2} (atm.)	Activation Enthalpies (Kcal/mole)
10^{-13}	131.628
10^{-14}	130.564
10^{-15}	129 010
10^{-16}	132.021
10^{-17}	129.918
10^{-18}	129.664

Table 5.16

ACTIVATION ENTHALPIES FOR CONDUCTION IN THE HIGH P_{O_2} REGION FOR 0.10 AT.% *La*-DOPED $SrZrO_3$

P_{O_2} (atm.)	Activation Enthalpies (Kcal/mole)
10^{0}	48.62
2.1×10^{-1}	50.10
10^{-2}	48.65
10^{-3}	49.01
10^{-4}	50.83
10^{-7}	51.99
10^{-8}	53.22

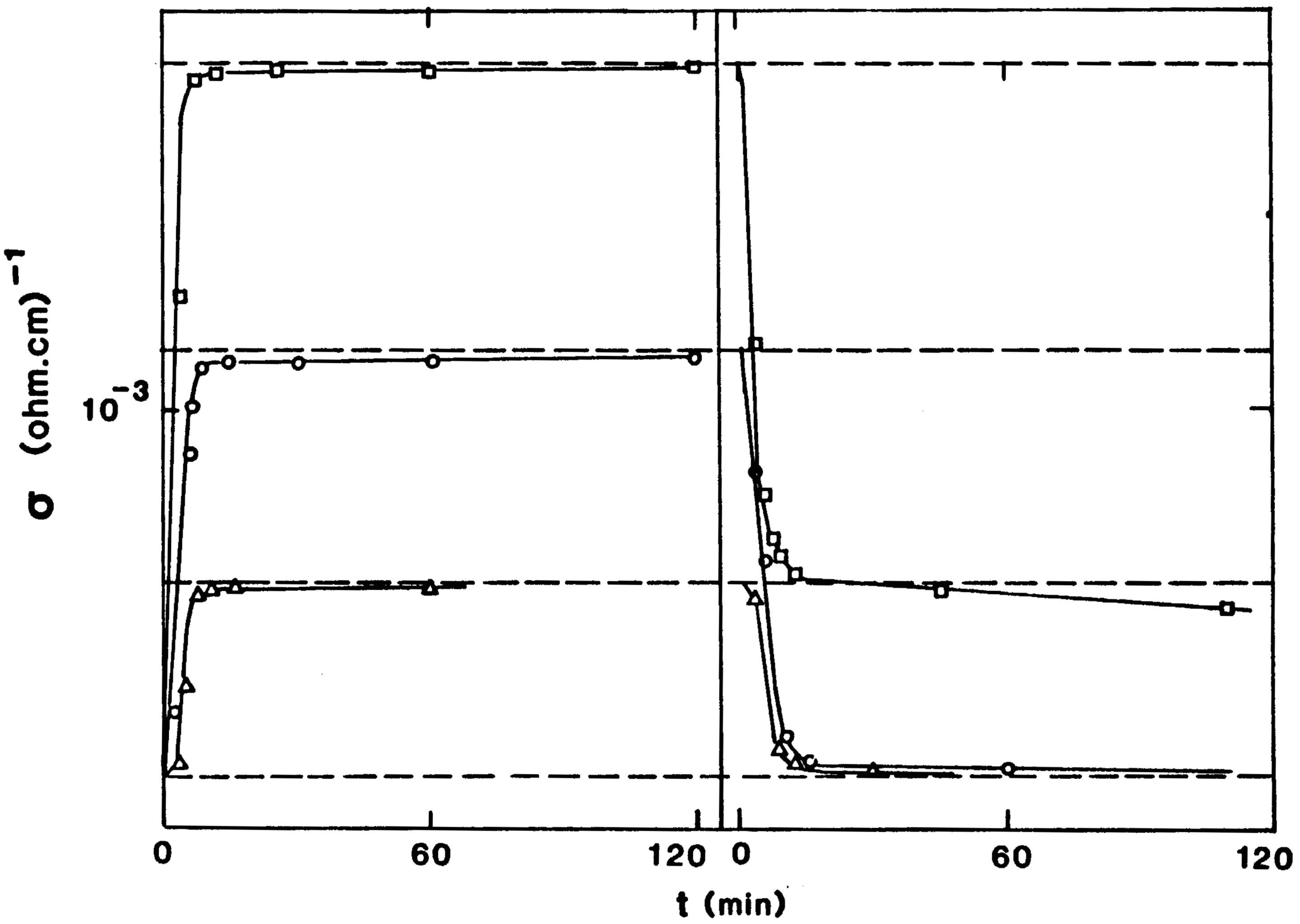

Figure 5-27: TRANSIENT CONDUCTIVITY AS A FUNCTION OF TIME AND P_{O_2} AT 1323 K:

△ 10^{-4}–10^{-3} atm. ○ 10^{-4}–10^{-2} atm. □ 10^{-4}–2.1×10^{-1} atm.

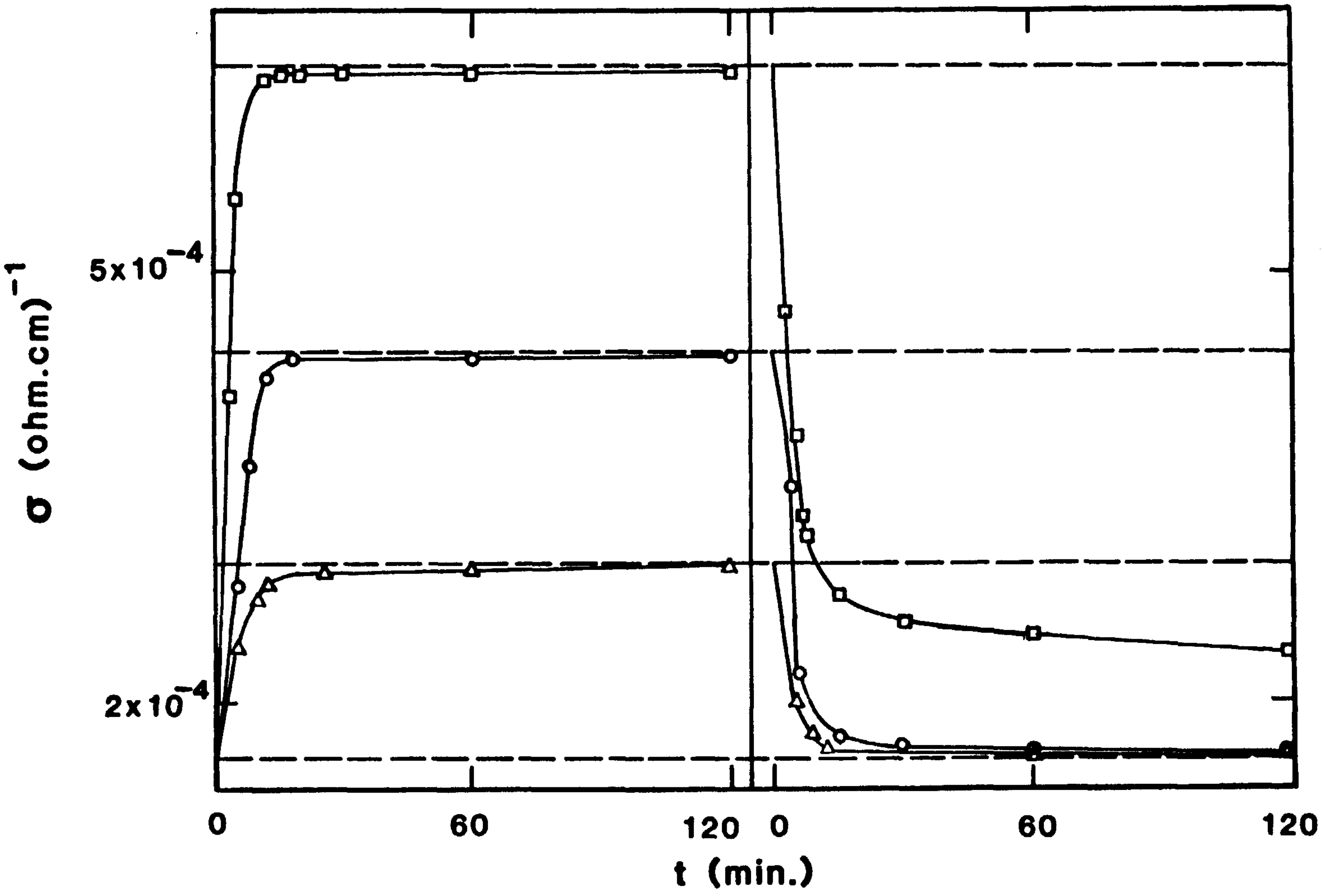

Figure 5-28: TRANSIENT CONDUCTIVITY AS A FUNCTION OF TIME AND P_{O_2} AT 1223 K:

△ $10^{-4}-10^{-3}$ atm. ○ $10^{-4}-10^{-2}$ atm. □ $10^{-4}-2.1\times10^{-1}$ atm.

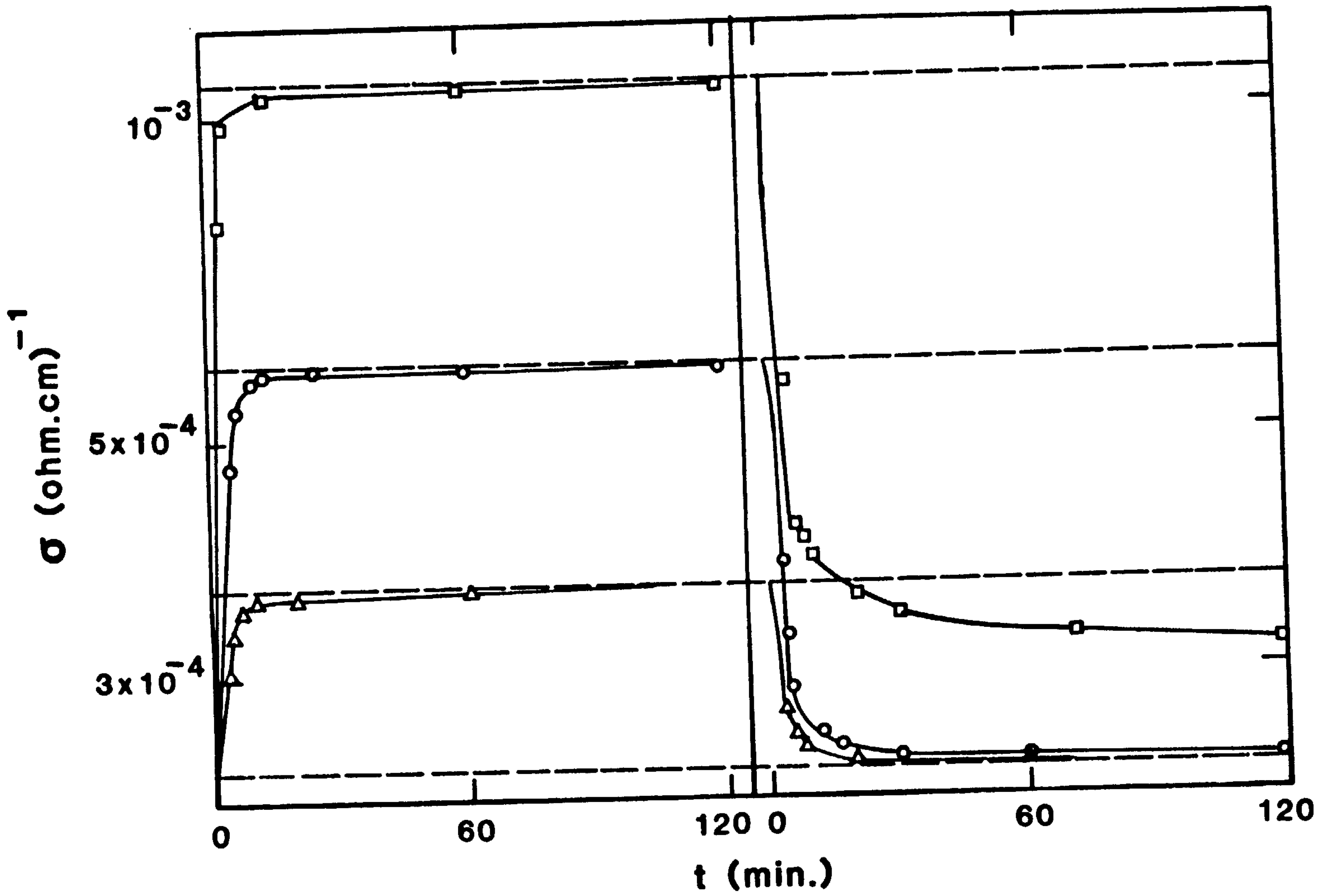

Figure 5-29: TRANSIENT CONDUCTIVITY AS A FUNCTION OF TIME AND P_{O_2} AT 1273 K:

△ $10^{-4}-10^{-3}$ atm. ○ $10^{-4}-10^{-2}$ atm. □ $10^{-4}-2.1\times10^{-1}$ atm.

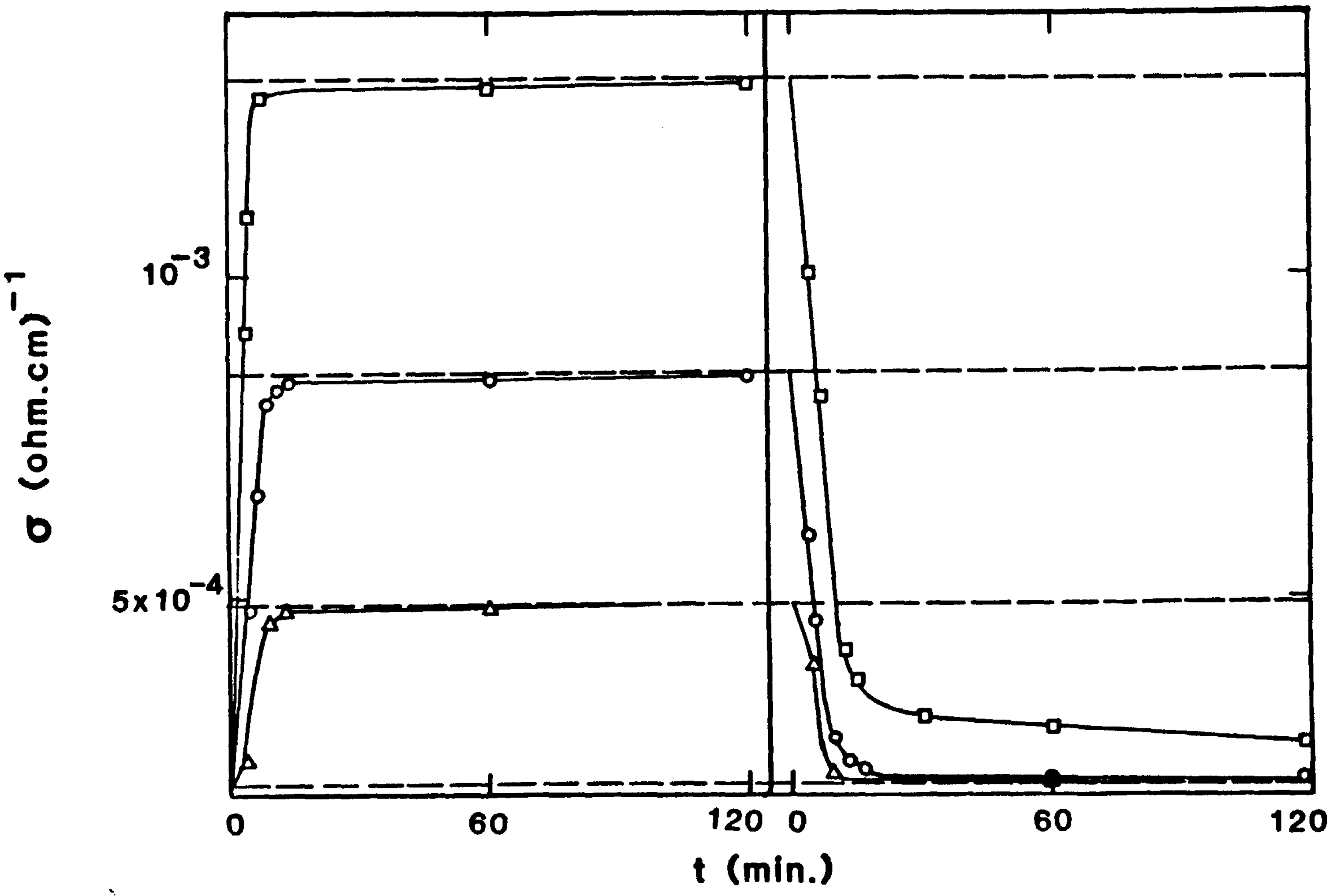

Figure 5-30: TRANSIENT CONDUCTIVITY AS A FUNCTION OF TIME AND P_{O_2} AT 1373 K:

△ $10^{-4}-10^{-3}$ atm. ○ $10^{-4}-10^{-2}$ atm. □ $10^{-4}-2.1\times10^{-1}$ atm.

observe the dependence of the diffusion coefficient on P_{O_2}, conductivity experiments were also performed for several small steps in P_{O_2} values. These results are shown in Figure 5.31.

In all cases, the electrical conductivity was measured on brick-shaped samples. As explained in Section 1.5, for a brick-shaped sample of dimensions -a<x<a, -b<y<b and -c<z<c, in equilibrium with a gas phase of known composition (fixed P_{O_2} value), diffusion flow in 3-dimensions can be expressed by the relationship:

$$\frac{\partial C}{\partial t} = D\left(\frac{\partial^2 C}{\partial x^2} + \frac{\partial^2 C}{\partial y^2} + \frac{\partial^2 C}{\partial z^2}\right) \qquad (1.46)$$

The solution for the above equation is given by the Fourier series: (equation 1.50)

$$\frac{C-C_1}{C_0-C_1} = (seriesA)(SeriesB)(SeriesC) \qquad (1.50)$$

where,

$$SeriesA = \frac{4}{\pi}\left[\left(\frac{\pi x}{2a}\right)\exp\left(-Dt\left(\frac{\pi}{2a}\right)^2\right) - \frac{1}{3}\cos\left(\frac{3\pi x}{2a}\right)\exp\left(-9Dt\left(\frac{\pi}{2a}\right)^2\right) + \ldots..\right] \qquad (1.47)$$

Series B and C are identical to Series A except that y and z are substituted for x and 2b and 2c for 2a, respectively. In the above equations, C is the excess concentration of the diffusing species (oxygen) as a function of position (x,y,z) and time (t), C_0 is the initial uniform excess concentration and C_1 is the final uniform excess concentration. D is assumed to be independent of concentration (10-12). The boundary conditions are C(x,y,z,0) = C_0 and C(0,0,0,t) = C_1. The total change in oxygen concentration, $\sum$, in terms of weight change, can be obtained by integrating C(x,y,z,t) with respect to x, y and z as follows (10):

$$\sum = 1 - \frac{\Delta w_t}{\Delta w_\infty} \qquad (5.23)$$

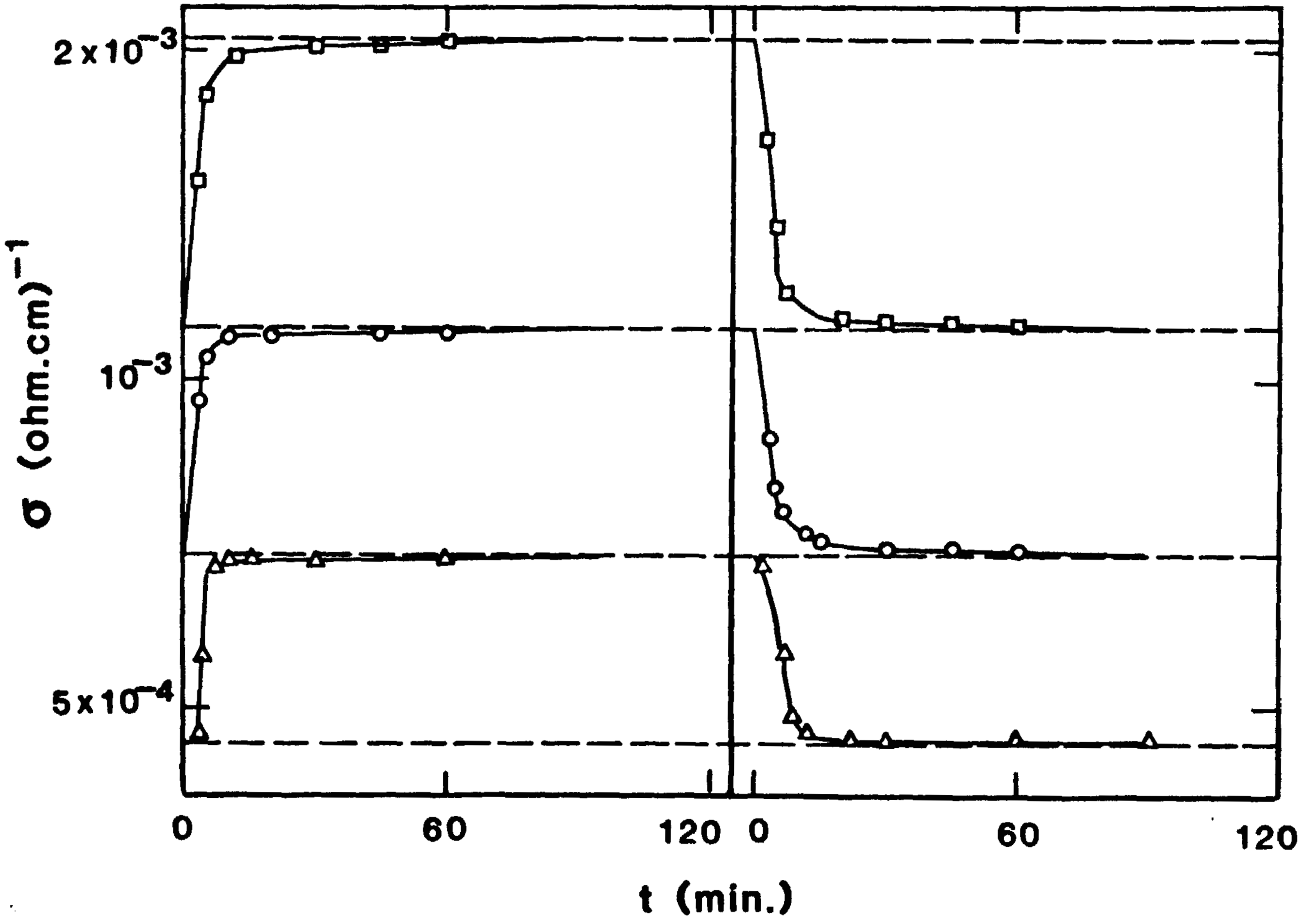

Figure 5-31: TRANSIENT CONDUCTIVITY AS A FUNCTION OF TIME FOR SMALL STEP CHANGES IN P_{O_2}:

△ 10^{-4}–10^{-3} atm. ○ 10^{-3}–10^{-2} atm. □ 10^{-2}–2.1×10^{-1} atm.

Hence,

$$\sum = \frac{1}{abc}\int_0^a \int_0^b \int_0^c \frac{C-C_1}{C_0-C_1}dx\ dy\ dz \tag{5.24}$$

From equations (1.50) and (5.24),

$$\sum = \frac{8.8.8}{\pi^6}(exp[-Dt(\frac{\pi}{2c})^2-\ldots])(exp[-Dt(\frac{\pi}{2b})^2-\ldots])(exp[-Dt(\frac{\pi}{2c})^2-\ldots]) \tag{5.25}$$

where Δw_t is the weight change at time t and Δw_∞ is the total weight change measured between the initial and final equilibrium states. When $\sum<0.5$, the first term in each series is large compared to the following terms, giving:

$$1-\frac{\Delta w_t}{\Delta w_\infty} = \frac{8.8.8}{\pi^6}[-\frac{D}{4}(\frac{1}{a^2}+\frac{1}{b^2}+\frac{1}{c^2})] \tag{5.26}$$

From the above equation, the diffusion coefficient can be obtained as:

$$D = \frac{0.934}{t(\frac{1}{a^2}+\frac{1}{b^2}+\frac{1}{c^2})}\log\left[\frac{0.533}{1-\frac{\Delta w_t}{\Delta w_\infty}}\right] \tag{5.27}$$

When the weight changes involved are very small, it is more convenient to measure electronic conductivity. The thermogravimetric and conductivity methods of measuring the defect-diffusion coefficients are based on the measurement of changes in physical properties which are directly proportional to the volume average of the defect concentrations. Since concentration of the electronic carrier changes linearly with the concentration of the lattice defect (Figure 5.15), the two techniques should yield the same result. As explained in Section 5.3, in the temperature range of 1173 - 1373 K and P_{O_2} range of 10^0-10^{-4} atm., the diffusion controlled reaction which occurs when the oxygen pressure over $SrZrO_3$ is changed, incorporates oxygen into the lattice according to the reaction:

$$V_O^{\cdot\cdot} + \frac{1}{2}O_2 = O_O + 2p \tag{5.10}$$

where O_O is an excess oxygen atom on a regular oxygen site and 'p' is a free electron hole.

When holes are the dominant charge carriers, the electrical conductivity can be expressed as (equation 5.5):

$$\sigma = e^{+}\mu_p[p] \tag{5.5}$$

where e^{+} is the charge of an electron hole and μ_p is the electron hole mobility. Combining equations (5.5) and (5.10) the change in oxygen concentration (ΔO_O), which is equal to the corresponding weight change (Δw), can be expressed as a function of the conductivity change ($\Delta\sigma$) according to:

$$\frac{\Delta w}{unit\ \ volume} = \Delta[O_O] = k\,\Delta[p] \tag{5.28}$$

where k is a constant. Substitutin for [p] from equation (5.10),

$$\frac{\Delta w}{unit\ \ volume} = k.\frac{1}{e^{+}}(\frac{\Delta\sigma}{\mu_p}) \tag{5.29}$$

Thus,

$$\frac{\Delta w_t}{\Delta w_\infty} = \frac{\Delta\sigma_t}{\Delta\sigma_\infty}.\frac{\mu_t}{\mu_\infty} \tag{5.30}$$

If the electron hole mobility is independent of oxygen pressure (10-12), the ratio $\frac{\mu_t}{\mu_\infty}$ can be set to unity. Hence,

$$\frac{\Delta w_t}{\Delta w_\infty} = \frac{\Delta\sigma_t}{\Delta\sigma_\infty} \tag{5.31}$$

Substituting for $\frac{\Delta w_t}{\Delta w_\infty}$ from equation (5.31) into equation (5.27),

$$D = \frac{0.934}{t(\frac{1}{a^2}+\frac{1}{b^2}+\frac{1}{c^2})}\log\left[\frac{0.533}{1-\frac{\Delta\sigma_t}{\Delta\sigma_\infty}}\right] \tag{5.32}$$

The values of the diffusion coefficient calculated using equation (5.32) were plotted as a function of time at five different temperatures under both oxidizing and reducing conditions and when P_{O_2} was varied over different ranges (Figures 5.32 and 5.33). In all cases, the diffusion coefficient decreased with decreasing temperature. The relationships between chemical diffusion coefficient (D) and self diffusion coefficient (D_s) can be expressed as (103-106) :

$$D = (1+z)D_s\frac{1}{x_d} \tag{5.33}$$

where z is the valency of the diffusing species and x_d is the site fraction of the dominant defects. Equation (5.33) assumes that D_s for the components involved are markedly different and that when the concentration of defects is small, the defect activities can be replaced by concentrations. The term (1+z) is related to the diffusion potential and regards the fact that ions are accelerated by the more mobile electrons, while the movement of electrons is decelerated by ions. Since,

$$D_s = x_d D_d \tag{5.34}$$

where D_d is the diffusion coefficient of defects, equation 5.33) can be written as:

$$D = (1+z)D_d \tag{5.35}$$

That is,

$$D = (1+z)D_d{}^0\exp\left(-\frac{\Delta G_m}{RT}\right) \tag{5.36}$$

The activation energy of chemical diffusion (ΔG_m) refers to the energy of motion of lattice defects (107). Splitting up ΔG_m into the entropy and enthalpy terms,

$$D = K_m\exp\left(-\frac{\Delta H_m}{RT}\right) \tag{5.37}$$

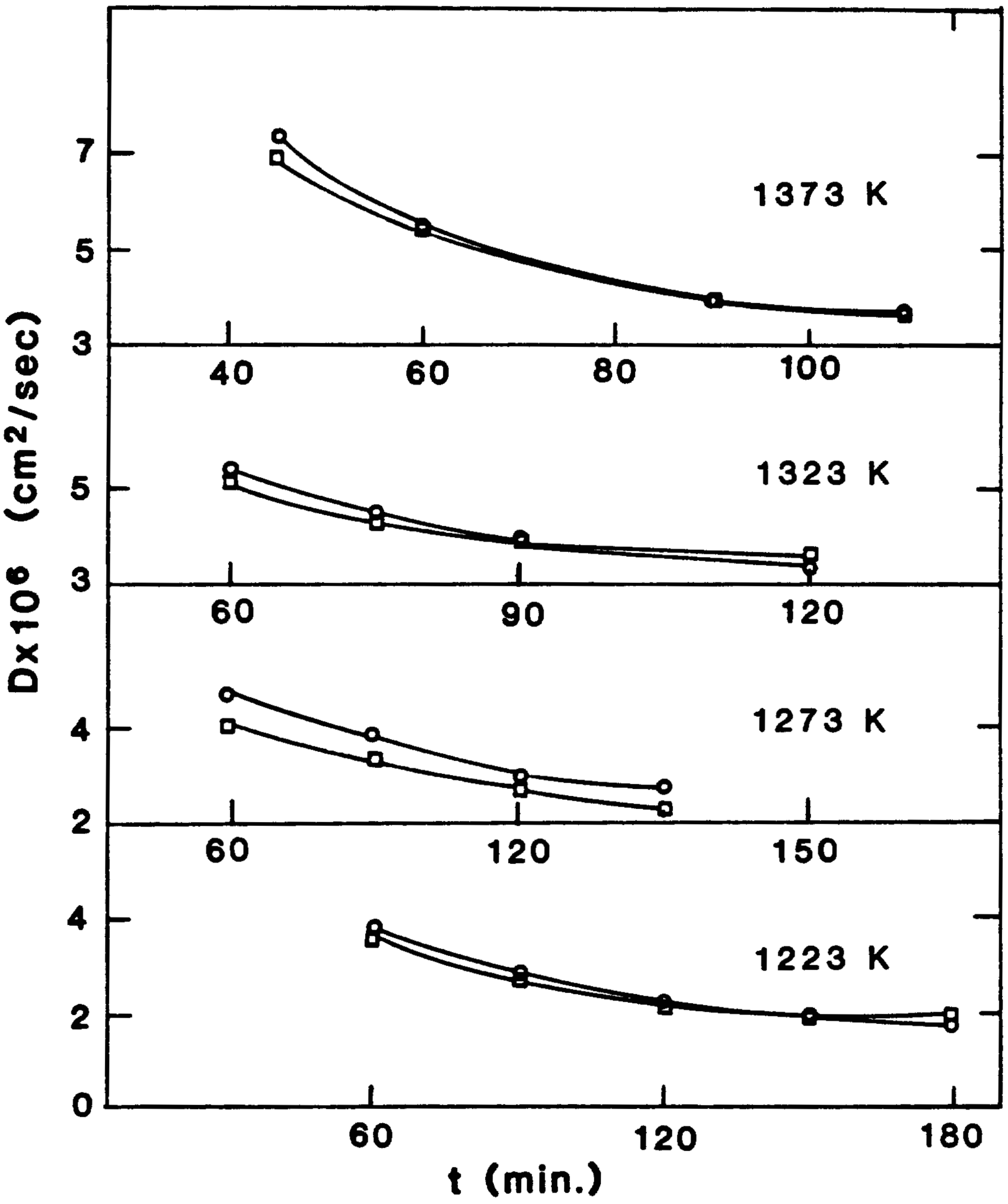

Figure 5-32: CALCULATED CHEMICAL DIFFUSION COEFFICIENT AS A FUNCTION OF TIME (10^{-4}–10^{-3} ATM.):

□ Oxidation ○ Reduction

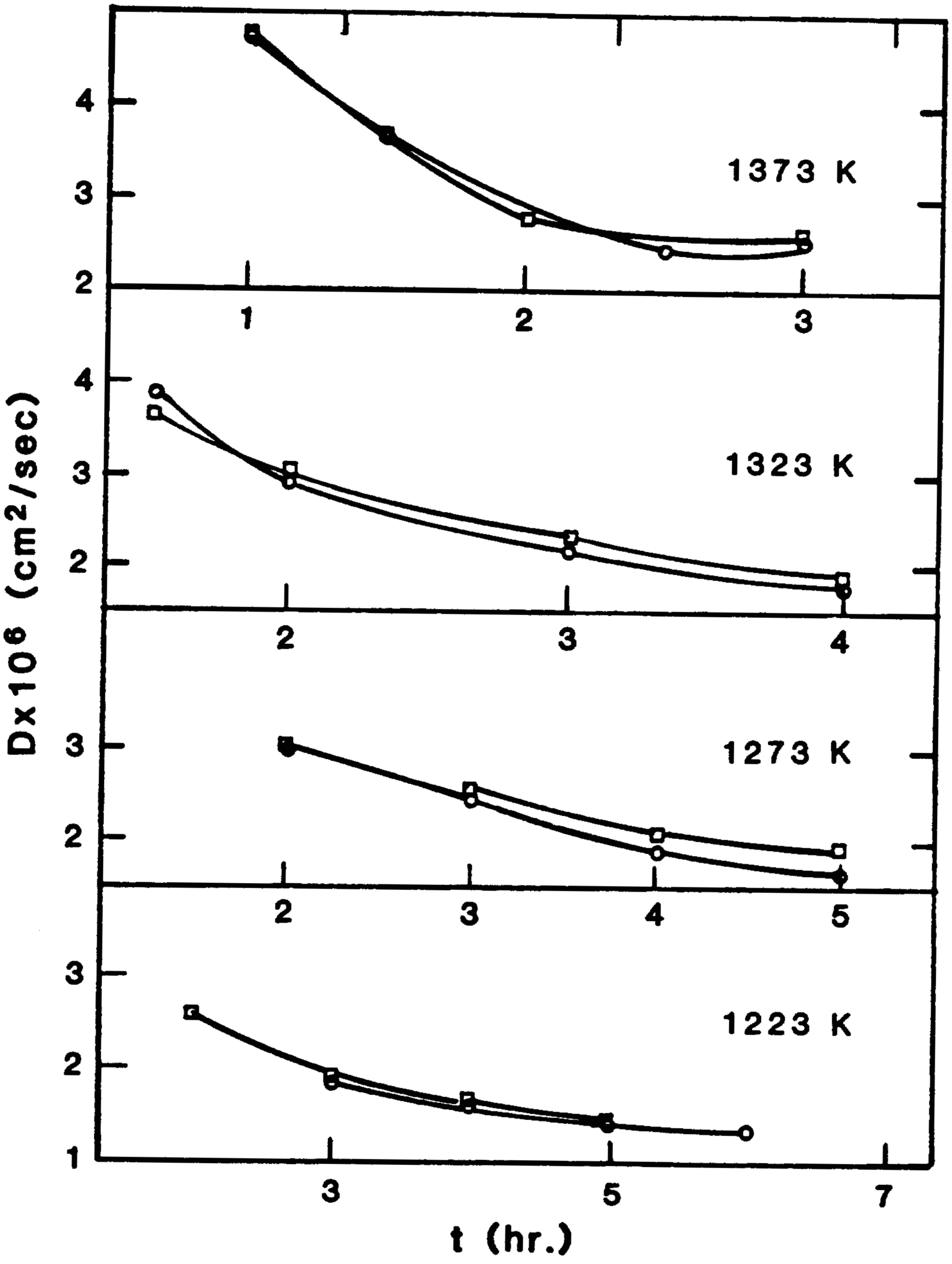

Figure 5-33: CALCULATED CHEMICAL DIFFUSION COEFFICIENT AS A FUNCTION OF TIME (10^{-4}–10^{-2} ATM.):

□ Oxidation ○ Reduction

where,

$$K_m = (1+z)D_d{}^0\exp\frac{\Delta S_m}{R} \tag{5.38}$$

From the above equation,

$$\frac{\partial(lnD)}{\partial(\frac{1}{T})} = -\frac{\Delta H_m}{R} \tag{5.39}$$

Equation (5.39) indicates that the Arrhenius plot of log D vs. 1/T will be linear with a slope equal to $\frac{-\Delta H_m}{R}$. In Figure 5.34, these plots are generated for variations of P_{O_2} between the four ranges studied in this investigation. From the slopes of the straight lines, the average activation enthalpy for the motion of defects was calculated to be 16.62 Kcal/mole. In Section 5.3, for pure $SrZrO_3$, in the same P_{O_2} range ($2.1\times10^{-1}-10^{-4}$ atm.), the variation of equilibrium electrical conductivity with P_{O_2} was explained in terms of an oxidation reaction involving vacancies of oxygen by incorporation of oxygen from gas phase into the lattice as follows: that is,

$$V_O^{\cdot\cdot} + \frac{1}{2}O_2 = O_O + 2p \tag{5.10}$$

The equilibrium constant, K, for this reaction is given by:

$$K = [p]/[V_O^{\cdot\cdot}]P_{O_2}{}^{\frac{1}{2}} = \exp-(\frac{\Delta G_a}{RT}) \tag{5.40}$$

giving,

$$[V_O^{\cdot\cdot}] = p^2P_{O_2}{}^{-\frac{1}{2}}exp-(\frac{-\Delta G_a}{RT}) \tag{5.41}$$

That is,

$$[V_O^{\cdot\cdot}] = p^2P_{O_2}{}^{-\frac{1}{2}}\exp-(\frac{\Delta G_f}{RT}) \tag{5.42}$$

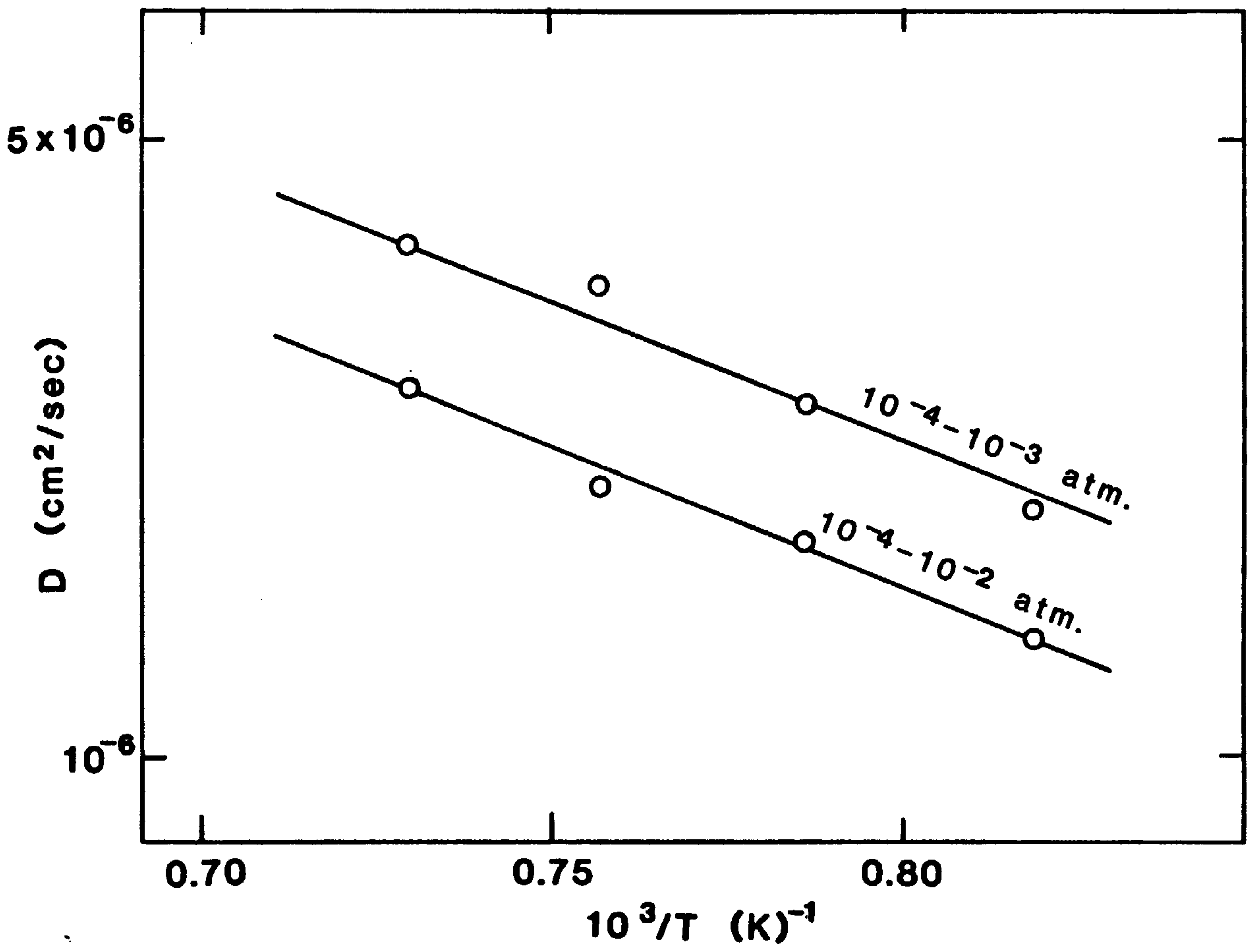

Figure 5-34: DIFFUSION COEFFICIENT VS. RECIPROCAL OF ABSOLUTE TEMPERATURE

where,

$$-\Delta G_a = \Delta G_f \tag{5.43}$$

From Section 5.3,

$$p \propto P_{O_2}^{\frac{1}{4}}$$

Hence,

$$[V_O^{\cdot\cdot}] = K_f P_{O_2}^{0} \exp -(\frac{\Delta G_f}{RT}) \tag{5.44}$$

$V_O^{\cdot\cdot}$ is the dominant lattice defect in this region. Therefore,

$$x_d = V_O^{\cdot\cdot} \tag{5.45}$$

Hence,

$$x_d = K_f P_{O_2}^{0} \exp -(\frac{\Delta H_f}{RT}) \tag{5.48}$$

In the above equation, ΔG_f, ΔS_f and ΔH_f represent the free energy, entropy and enthalpy of formation of defects. From the results of equations (5.35)-(5.38) and (5.46), equation (5.34) can be rewritten as:

$$D_s = \frac{K_f K_m}{1+z} \exp -(\frac{\Delta H_m + \Delta H_f}{RT}) \tag{5.47}$$

That is,

$$D_s = K \exp -(\frac{\Delta H_m + \Delta H_f}{RT}) \tag{5.48}$$

where,

$$K = K_f K_m / (1+z) \tag{5.49}$$

Taking ΔH_m as 16.62 Kcal/ mole and ΔH_f as 42.87 Kcal/mole, the enthalpy of the total process of self-diffusion of the ionized oxygen vacancies in $SrZrO_3$ was calculated to be about 26.25 Kcal/mole from equation (5.47). This value should be regarded as the activation enthalpy for oxygen self diffusion.

Another significant result of this study is that the value of D selected for a given experiment was one that corresponded to a long time (approximately three quaters of the total experiment time). When the gas composition is changed suddenly, the initially equilibrated concentrations near the surface will attempt to adjust towards the new equilibrium value in the sample, imposed by the new values of composition in the gas phase. Under these conditions, the bulk properties may remain essentially constant. The independence of the diffusion coefficient to small step changes in P_{O_2} values (Figure 5.31) establishes the fact that there is no observable dependence of defect diffusivity on P_{O_2}. This observation agrees with the results of Wimmer et al (108) and Chowdhry and Coble (109). The changes in P_{O_2} should be held to small values to observe its effect upon diffusivity. If the P_{O_2} variation is large (eg. 10^{-4}–2.1×10^{-1} atm.), D may vary slightly with P_{O_2} under reducing condition (Figure 5.35). This indicates that when oxygen vacancies are generated at the external surface and diffuse into the crystal, the diffusion coefficient decreases, as the concentration of vacancies increases. However, under oxidizing conditions, the diffusion coefficient was found to be fairy constant. This is probably due to vacancy annihilation at internal sinks, such as dislocations or subgrain boundaries, with considerably smaller dimensions than those of the crystal.

5.6 Interdiffusion in $BaZrO_3$–$SrZrO_3$

It is not the primary intent of this investigation to study interdiffusion in zirconates. However, this section is devoted to a limited attempt in this area since it was felt that if layers of mixed zirconate of Ba and Sr with precisely controllable composition could be formed on a passive substrate, for instance, then

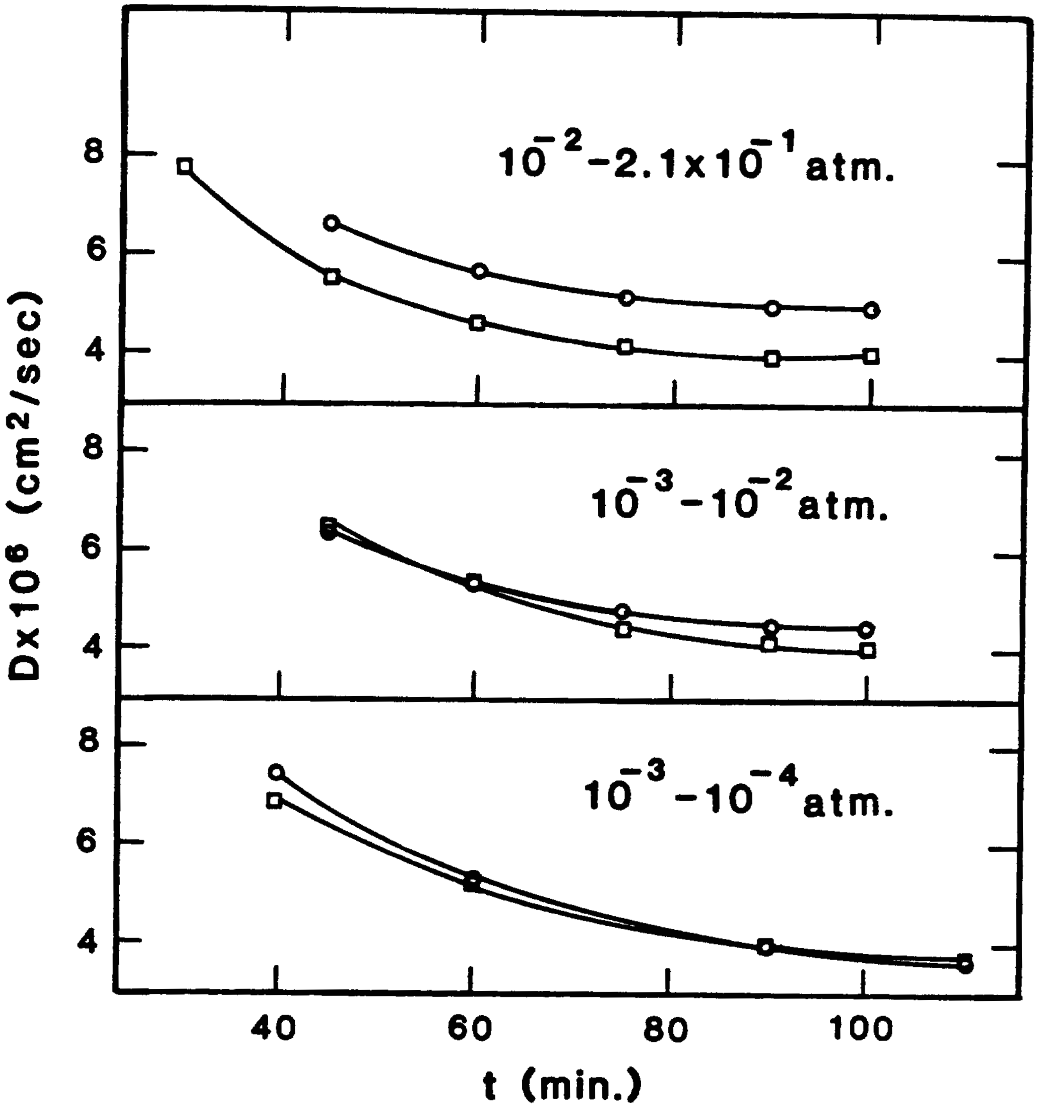

Figure 5-35: CALCULATED CHEMICAL DIFFUSION COEFFICIENT AS A FUNCTION OF TIME FOR SMALL STEP CHANGES IN P_{O_2}:

□ Oxidation ○ Reduction

there could be a number of interesting device applications for these structures such as delay lines, slow wave structures, optical modulators etc. The first step was to evaluate whether the above mixed zirconate could be formed at all and for this interdiffusion experiments were carried out.

$BaZrO_3$ and $SrZrO_3$ crystallize in the same perovskite structure. In view of the similarity of the crystal structures and ionic size, $(Ba,Sr)ZrO_3$ solid structure were expected to form by the simple interdiffusion of Ba^{+2} and Sr^{+2} ions in a relatively rigid Zr-O lattice. Such results have been reported in $(Ba,Sr)TiO_3$ (40,110,111).

The concentration profiles obtained at five temperatures are shown in Figures 5.36-5.40. Penetration curves of Sr and Ba have gentle slopes in the $BaZrO_3$ rich side but they sharply increase with Sr concentration. This means that the interdiffusivity has a large concentration dependency. Interdiffusion coefficients as a function of concentration were calculated using the Boltzman - Matano method. In this method, diffusivity is assumed to be a function of concentration, which requires the solution of Fick's second law in the form:

$$\frac{\partial N_A}{\partial t} = \frac{\partial}{\partial x} D(N_A) \frac{\partial N_A}{\partial x} \tag{5.50}$$

This mathematical operation is much more difficult than when D is constant with respect to composition and, as a consequence, the Boltzman-Matano method of determining diffusivity uses graphical integration. In the $(Ba,Sr)ZrO_3$ system, the Ba and Sr are the species that would diffuse in a relatively rigid Zr-O lattice. Thus, in this case, the Boltzman-Matano analysis was applied to the Ba concentration and the Sr concentration vs. distance curves. The concentration dependent D_I is given by (111):

$$D_I(N_A)t = [2\frac{dN_A}{dx}]^{-1} \int_{N_{A_1}}^{N_A} x dN_A \tag{5.51}$$

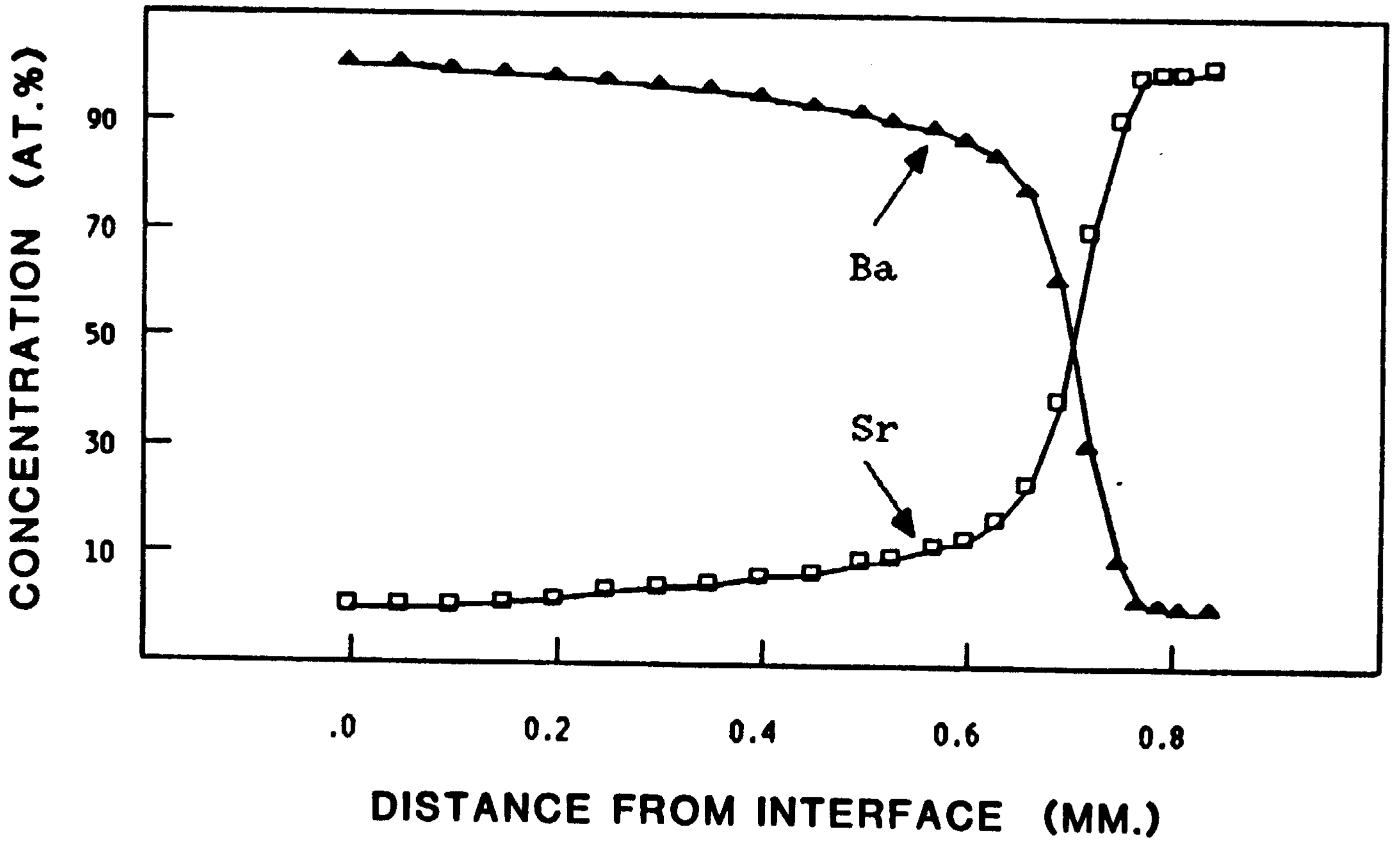

Figure 5-36: CONCENTRATION PROFILES OF *Sr* AND *Ba* IN ZIRCONATE MATRIX AT 1563 K

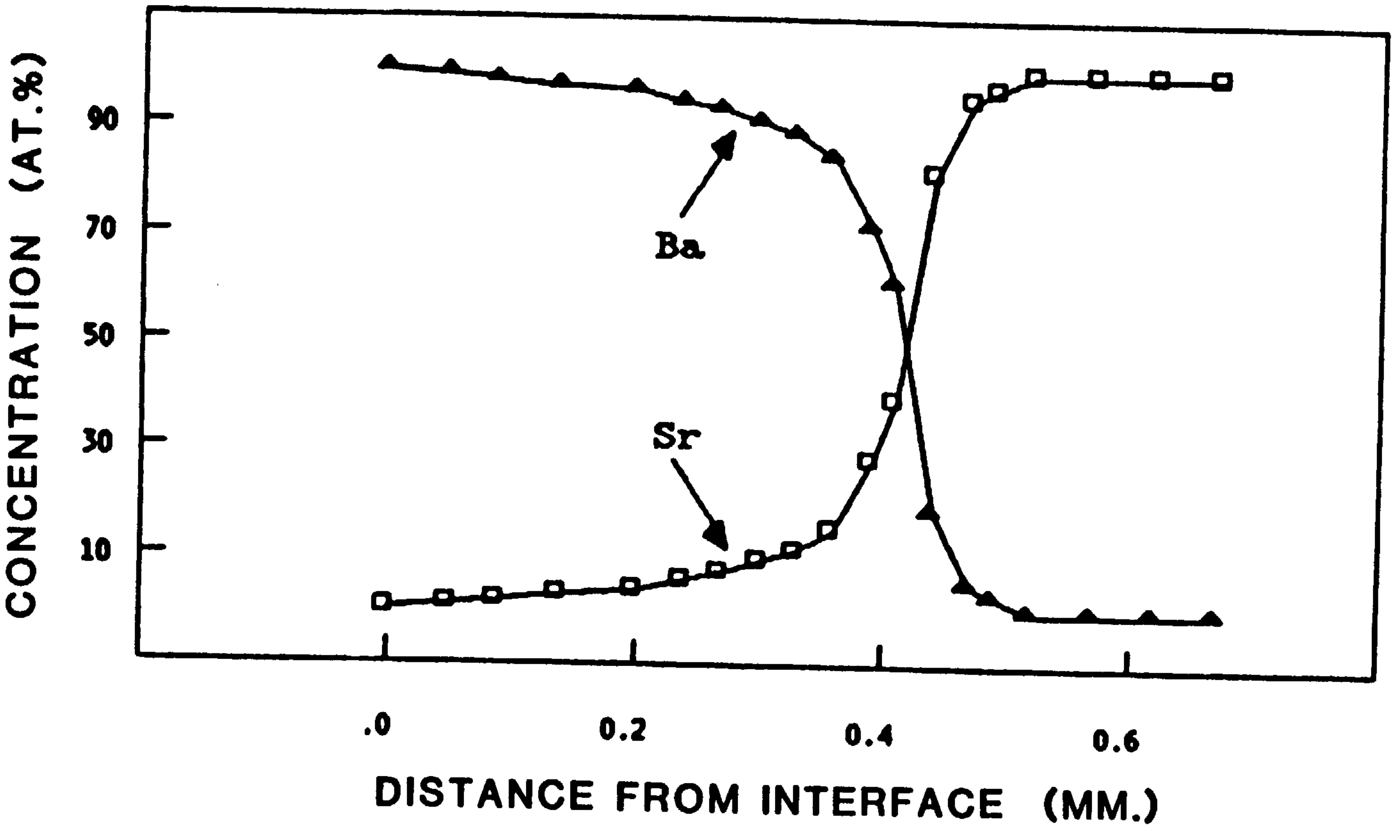

Figure 5-37: CONCENTRATION PROFILES OF *Sr* AND *Ba* IN ZIRCONATE MATRIX AT 1613 K

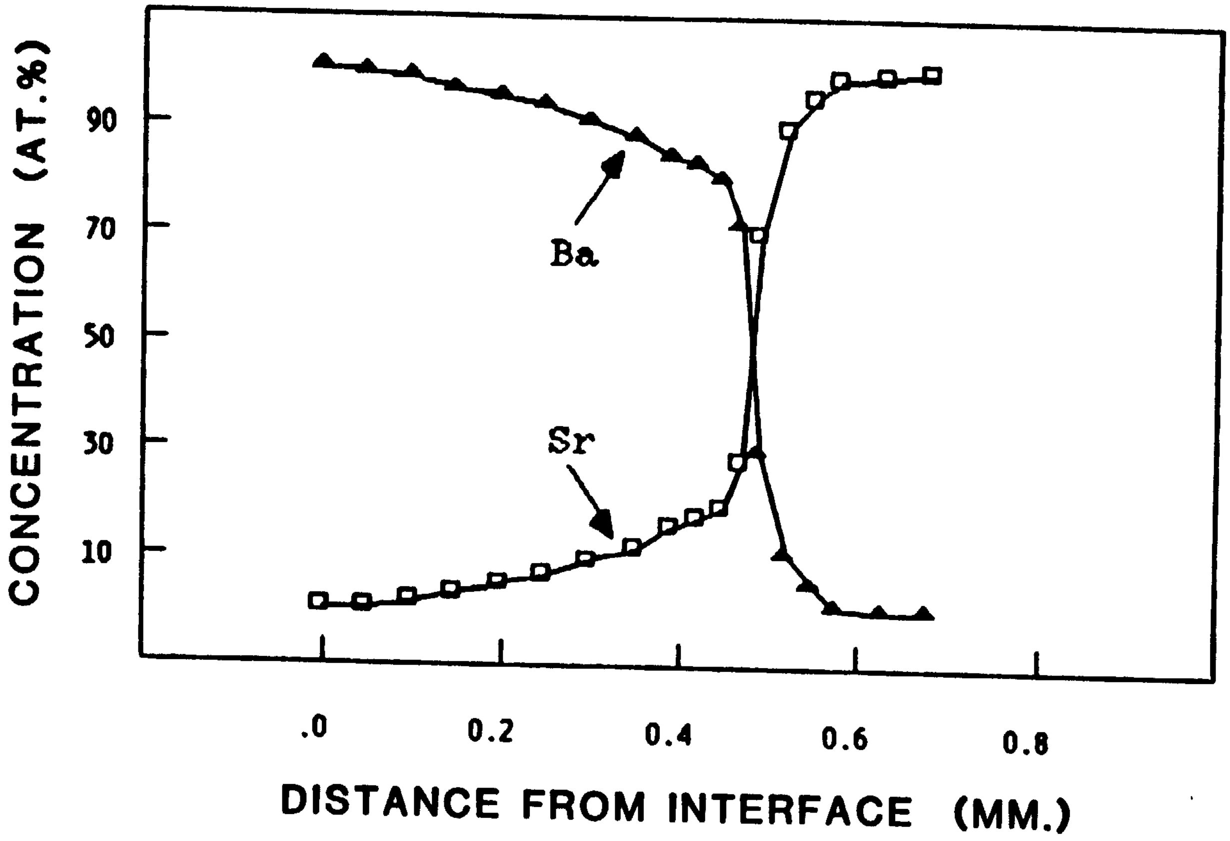

Figure 5-38: CONCENTRATION PROFILES OF *Sr* AND *Ba* IN ZIRCONATE MATRIX AT 1673 K

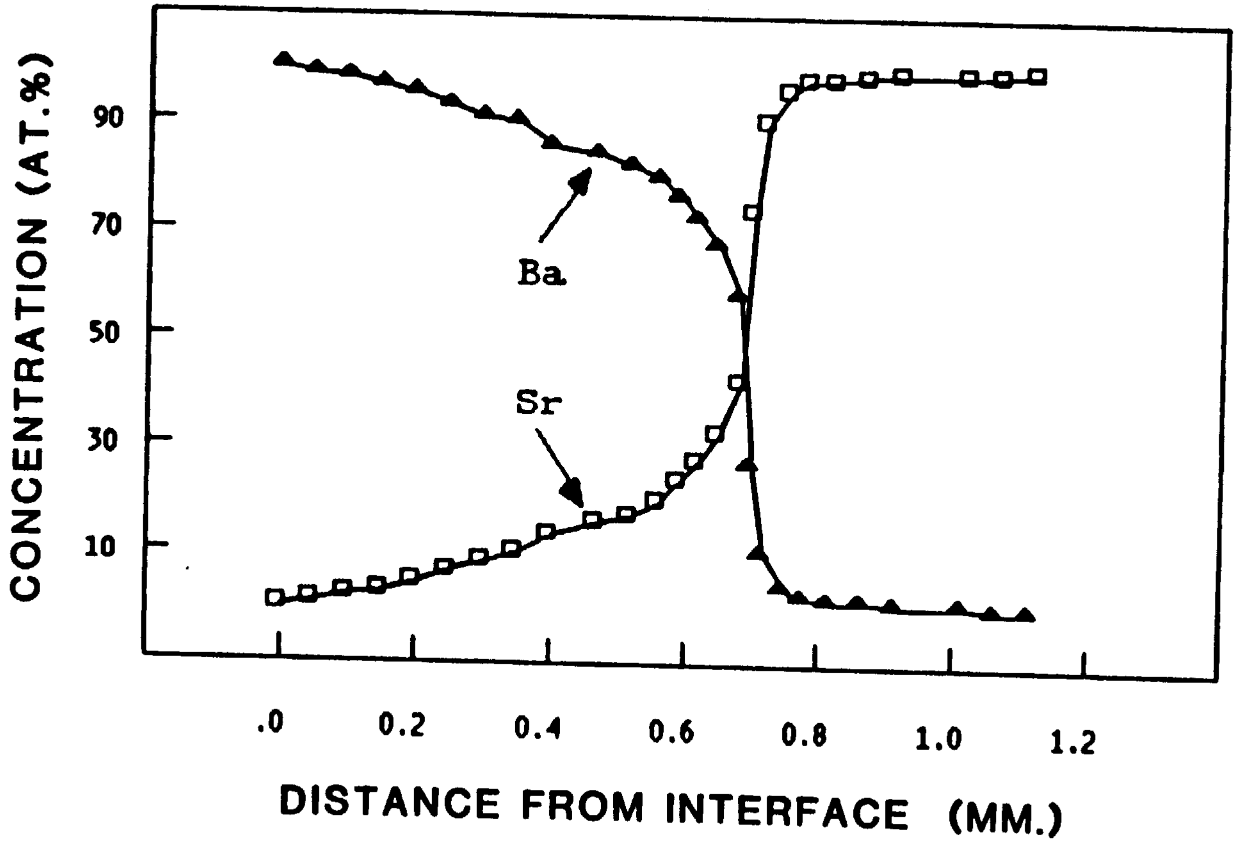

Figure 5-39: CONCENTRATION PROFILES OF *Sr* AND *Ba* IN ZIRCONATE MATRIX AT 1723 K

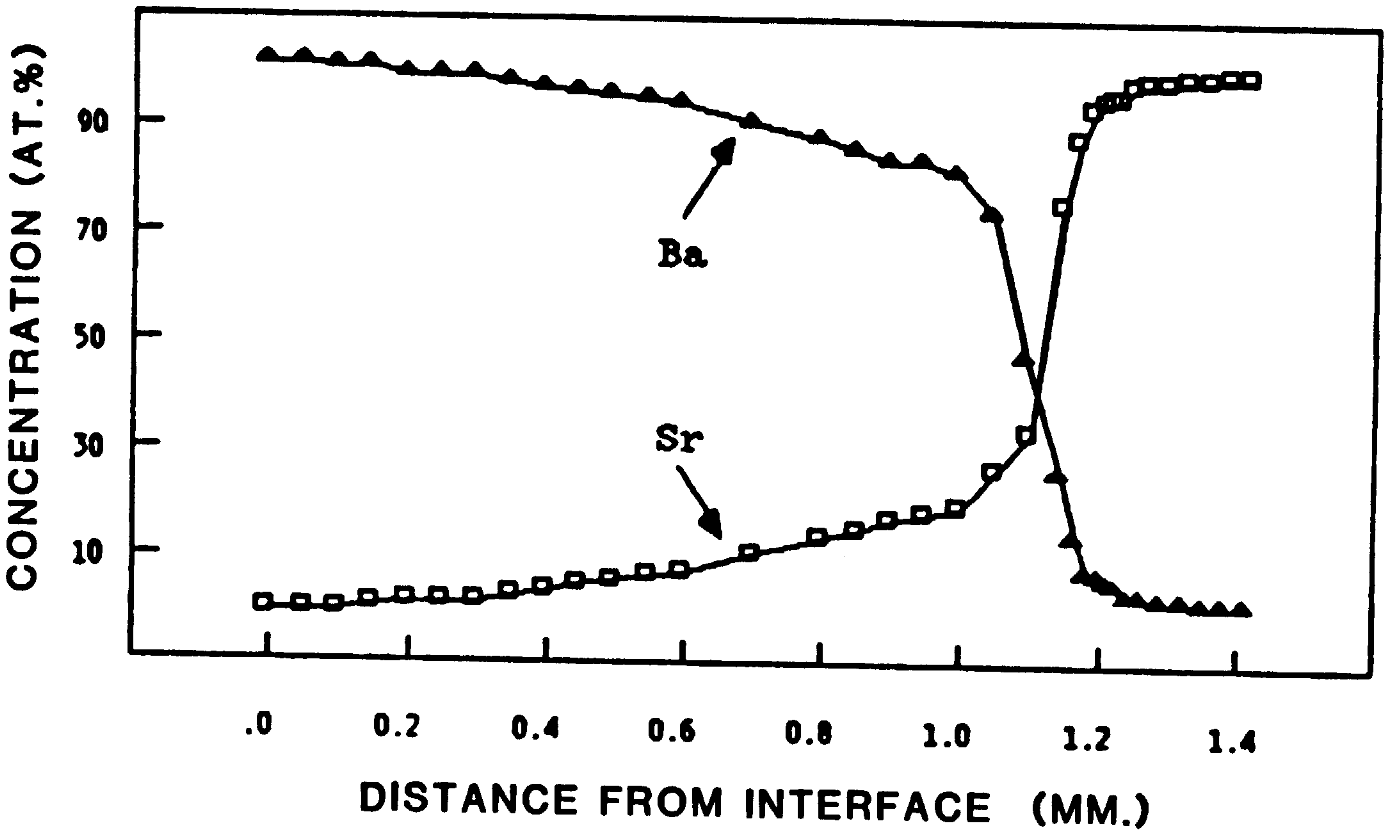

Figure 5-40: CONCENTRATION PROFILES OF *Sr* AND *Ba* IN ZIRCONATE MATRIX AT 1773 K

where N_A is the concentration in atomic units at a distance x measured from the Matano interface, and N_{A_1} is the concentration of one side of the diffusion couple at a point well removed from the interface where the composition is constant and not affected by the diffusion process and 't' is the total time of diffusion. The results of the interdiffusion coefficient calculations for the $(Ba,Sr)ZrO_3$ system are given in Tables 5.17-5.21 for samples annealed at 1563 K, 1613 K, 1673 K, 1723 K and 1773 K. Agreement between the values for the interdiffusion coefficients calculated from the concentration vs. distance curves of the two diffusing species was good. The results show that the interdiffusion coefficient increases with increasing Ba concentration and temperature. The variation of diffusivity with composition is especially marked for low concentrations of Sr. This also suggests that the value of the diffusion coefficient for Ba^{2+} and Sr^{2+} ions are strongly affected by the constituents of the lattice and large Ba^{2+} ions diffuse slower than the smaller Sr^{2+} ions. These results are consistent with the work of Ozdemir and Schwartz (42) for the (Sr,Ba)TiO_3 system. Although the values vary very widely with N_A, the actual values should be considered at the position of $N_A = 0.5$ (112), corresponding to the average composition of $BaZrO_3$ and $SrZrO_3$ and these results are listed in Table 5.22 for all the samples annealed at different temperatures. This table shows that at higher temperatures, the reaction rates are more rapid. The activation energy associated with the interdiffusion process was calculated to be 73.11 Kcal/mole from the Arrhenius plot of log D_I vs. 1/T (Figure 5.41) based on the Arrhenius expression:

$$D_I(T) = D_0 \exp(-\frac{Q}{kT}) \tag{5.52}$$

Table 5.17

INTERDIFFUSION COEFFICIENTS MEASURED AT 1563 K FOR $Sr_{1-x}Ba_xZrO_3$

Composition	Interdiffusion Coefficient (cm^2/s)
$Sr_{0.3}Ba_{0.7}ZrO_3$	5.30×10^{-13}
$Sr_{0.4}Ba_{0.6}ZrO_3$	3.64×10^{-13}
$Sr_{0.5}Ba_{0.5}ZrO_3$	3.24×10^{-13}
$Sr_{0.6}Ba_{0.4}ZrO_3$	2.75×10^{-13}
$Sr_{0.7}Ba_{0.3}ZrO_3$	2.27×10^{-13}

Table 5.18

INTERDIFFUSION COEFFICIENT MEASURED AT 1613 K FOR $Sr_{1-x}Ba_xZrO_3$

Composition	Interdiffusion Coefficient (cm^2/s)
$Sr_{0.3}Ba_{0.7}ZrO_3$	8.74×10^{-12}
$Sr_{0.4}Ba_{0.6}ZrO_3$	4.24×10^{-12}
$Sr_{0.5}Ba_{0.5}ZrO_3$	2.96×10^{-12}
$Sr_{0.6}Ba_{0.4}ZrO_3$	2.63×10^{-12}
$Sr_{0.7}Ba_{0.3}ZrO_3$	2.20×10^{-12}

Table 5.19

INTERDIFFUSION COEFFICIENTS MEASURED AT 1673 K FOR $Sr_{1-x}Ba_xZrO_3$

Composition	Interdiffusion Coefficient (cm^2/s)
$Sr_{0.3}Ba_{0.7}ZrO_3$	4.33×10^{-11}
$Sr_{0.4}Ba_{0.6}ZrO_3$	9.38×10^{-12}
$Sr_{0.5}Ba_{0.5}ZrO_3$	7.38×10^{-12}
$Sr_{0.6}Ba_{0.4}ZrO_3$	6.30×10^{-12}
$Sr_{0.7}Ba_{0.3}ZrO_3$	5.46×10^{-12}

Table 5.20

INTERDIFFUSION COEFFICIENTS MEASURED AT 1723 K FOR $Sr_{1-x}Ba_xZrO_3$

Composition	Interdiffusion Coefficient (cm^2/s)
$Sr_{0.3}Ba_{0.7}ZrO_3$	9.55×10^{-11}
$Sr_{0.4}Ba_{0.6}ZrO_3$	5.39×10^{-11}
$Sr_{0.5}Ba_{0.5}ZrO_3$	1.22×10^{-11}
$Sr_{0.6}Ba_{0.4}ZrO_3$	1.04×10^{-11}
$Sr_{0.7}Ba_{0.3}ZrO_3$	8.46×10^{-12}

Table 5.21

INTERDIFFUSION COEFFICIENTS MEASURED AT 1773 K FOR $Sr_{1-x}Ba_xZrO_3$

Composition	Interdiffusion Coefficient (cm^2/s)
$Sr_{0.3}Ba_{0.7}ZrO_3$	1.30×10^{-10}
$Sr_{0.4}Ba_{0.6}ZrO_3$	1.20×10^{-10}
$Sr_{0.5}Ba_{0.5}ZrO_3$	1.10×10^{-10}
$Sr_{0.6}Ba_{0.4}ZrO_3$	0.90×10^{-10}
$Sr_{0.7}Ba_{0.3}ZrO_3$	0.40×10^{-10}

Table 5.22

TEMPERATURE DEPENDENCE OF INTERDIFFUSION COEFFICIENT FOR $(Sr,Ba)ZrO_3$

Reaction Temperature (K)	Diffusion Coefficient (cm^2/s)
1463	3.24×10^{-13}
1613	2.96×10^{-12}
1673	7.38×10^{-12}
1723	1.22×10^{-11}
1773	1.10×10^{-10}

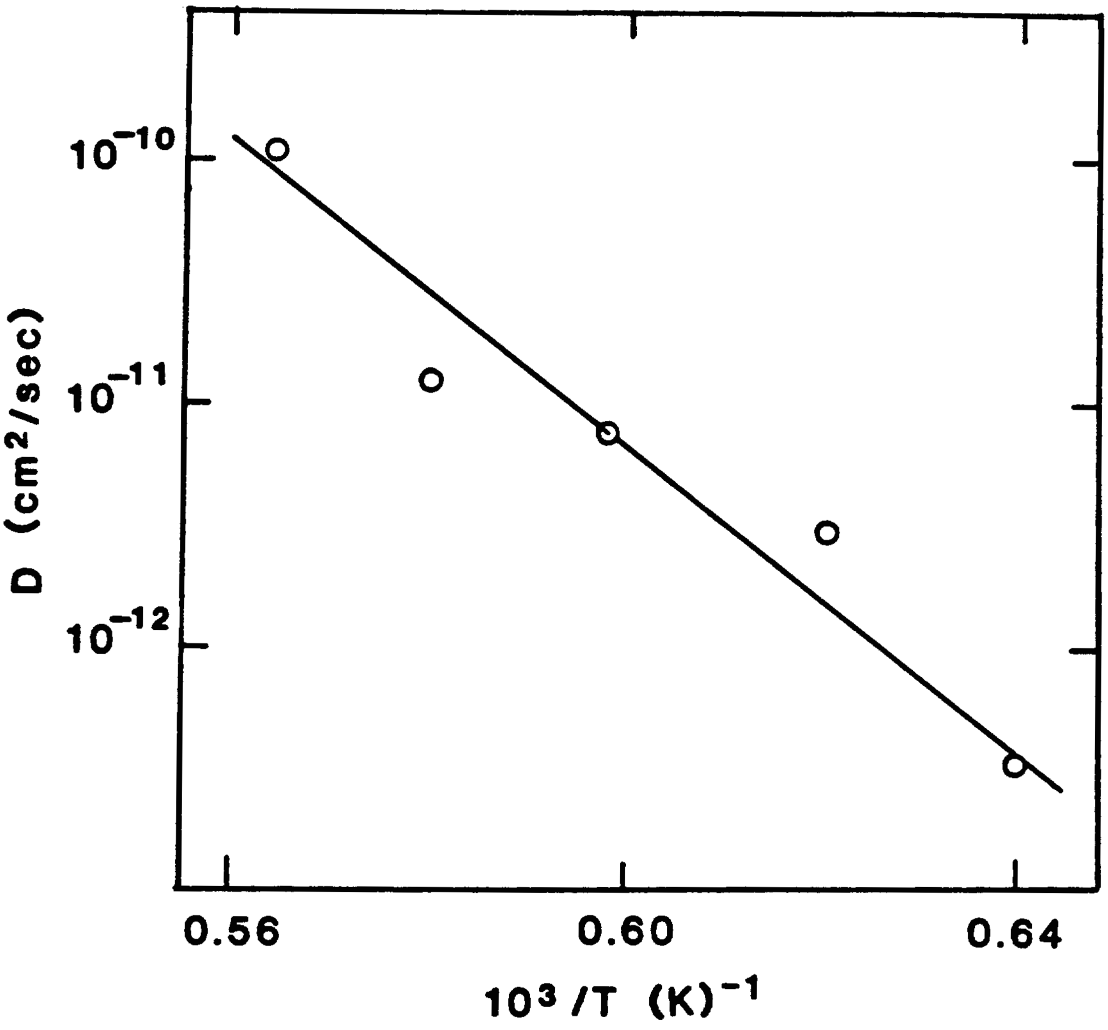

Figure 5-41: DIFFUSION COEFFICIENT VS. RECIPROCAL OF ABSOLUTE TEMPERATURE

5.7 Raman Spectra of $SrZrO_3$

Laser-excited Raman spectra were obtained for pure powder specimens at various temperatures (Figures 5.42 and 5.43). The ideal perovskite structure is cubic wherein the center of the unit cell is occupied by tetravalent cations such as zirconium, the corners by divalent cations and the face centers by oxygen atoms (Figure 5.44). $SrZrO_3$ is distorted from ideal perovskite symmetry to an orthorhombic symmetry with the space group P_{bnm} (52), with four molecular units per cell (46,48). The available site symmetries for this space group are $2C_i(4)$, $C_s(4)$ and $C_1(8)$. They represent all the possible kinds of sites for a $D_{2h}{}^{16}$ crystal, which is the Schoenflies symbol of space group P_{bnm} (113), but some of these may not be occupied in a specific crystal. The number contained in parentheses represents the number of equivalent atoms which have that particular site symmetry. Some of the site symmetries have numerical coefficients, such as $2C_i(4)$. The coefficient 2 here indicates the presence of two different and distinct kinds of C_i sites in the unit cell and each of them can accommodate four equivalent atoms.

Factor group analysis was used to interpret the spectra on the basis of space group $D_{2h}{}^{16}$ - P_{bnm}. The method of classifying fundamental vibrational modes of crystals, as developed by Bhagavantam and Venkatarayudu (114) is a laborious and difficult procedure. Hence, the correlation method of Fately et al (115) was adopted in this study to obtain the vibrational selection rules.

Although the available site symmetries are $2C_i(4)$, $C_s(4)$ and $C_1(8)$, the actual occupied site symmetries in $SrZrO_3$ are 4Sr(C_s- sites), 4O(C_s-sites), 4Zr(C_i-sites) and 8O(C_1-sites) (46). Once the site symmetry for each atom in the lattice is found, the symmetry species are identified for each equivalent set of atom displacements in the site. The displacements become the lattice vibrations in the crystal. These site species for the displacements are then related to the

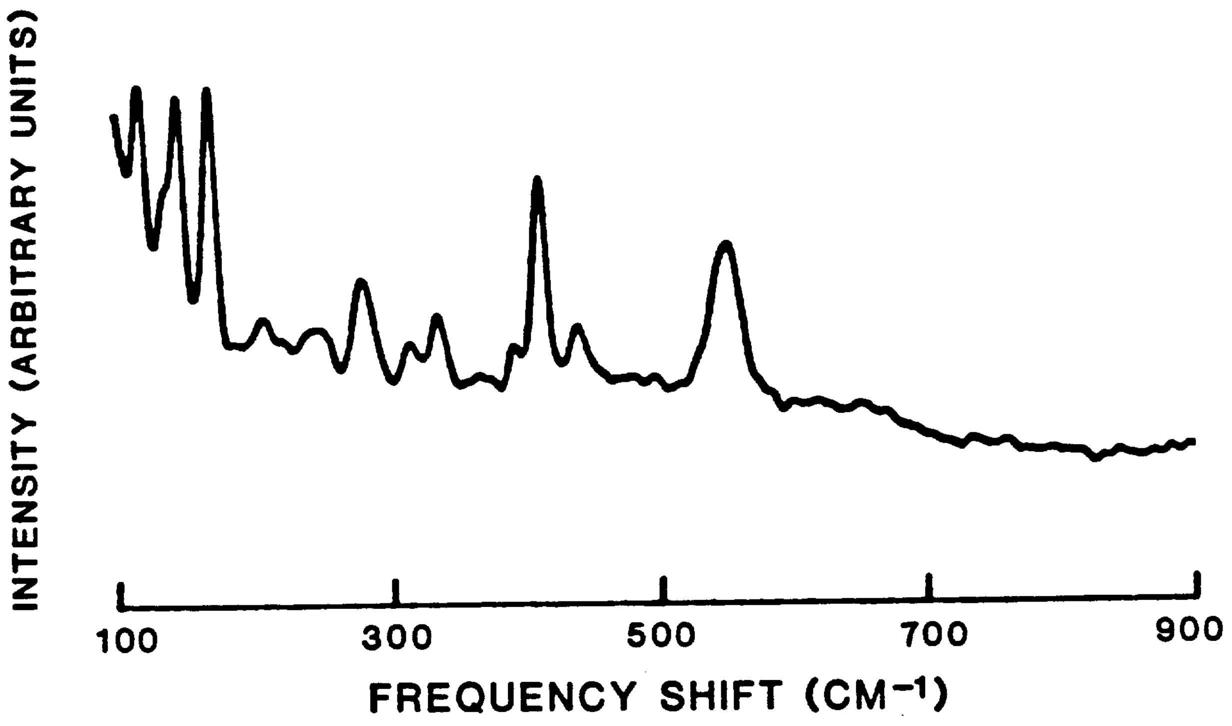

Figure 5-42: RAMAN SPECTRA OF POLYCRYSTALLINE $SrZrO_3$ AT ROOM TEMPERATURE

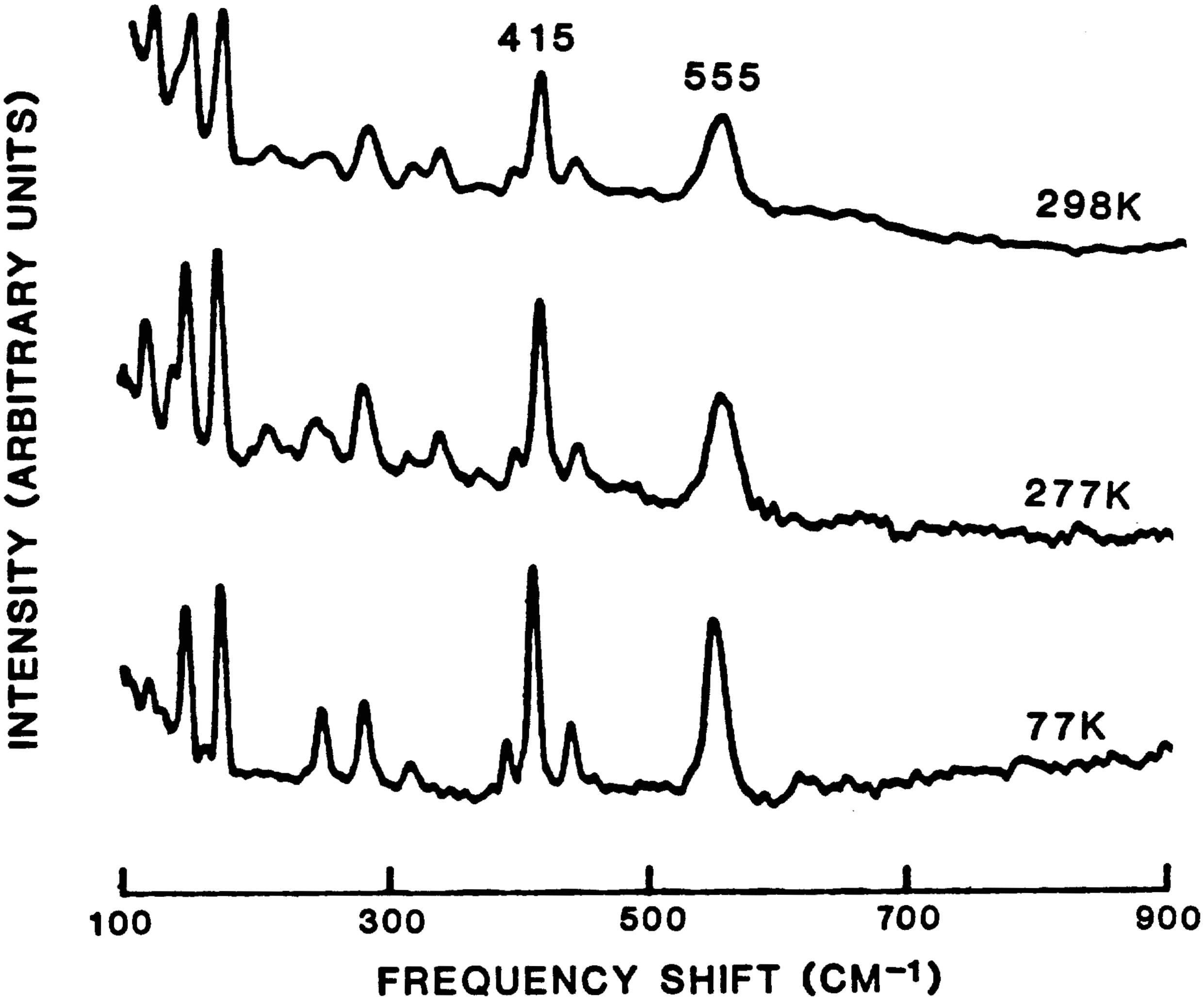

Figure 5-43: RAMAN SPECTRA OF POLYCRYSTALLINE $SrZrO_3$ AS A FUNCTION OF TEMPERATURE

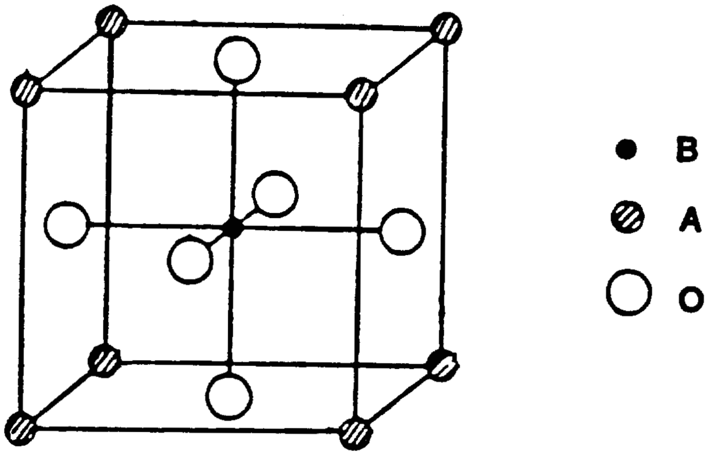

Figure 5-44: STRUCTURE OF CUBIC PEROVSKITE

species of the factor group by using the correlation tables. This correlation explicitely identifies the species of the lattice vibration in the crystal and further allows the predictions of infrared or Raman activity.

The irreducible representation that contains the number and species of the lattice vibrations can be obtained from the Bravais cell to get a minimum number of vibrations to represent the lattice vibrations of the crystal. The problem of including too many Bravais cells in the crystallographic cell can be eliminated by dividing the number of molecules per unit crystallographic cell (Z), by a small integer, which is identical to the number of lattice points (LP) in a crystallographic cell. For $SrZrO_3$, the Bravais space cell and the unit cell are identical (LP = 1) and there are 4 molecular units per cell. Hence, the number of molecules in the Bravais cell equals Z/LP (that is, 4/1).

The complete character tables for the point groups D_{2h}, C_i, C_s and C_1, are given in Tables 5.23-5.26. Each set of equivalent atoms, (strontium, zirconium and oxygen) is treated separately. For example, consider the 4Zr atoms which occupy the C_i site symmetry. The vibrational displacements of the zirconium atoms in the lattice can be derived as simple motions parallel to the x, y or z axis and then classified into one of the species of the C_i site symmetry. For instance, the displacements of the zirconium atom parallel to the z axis has the same character as the translation in the z direction. From the character table of C_i, the translation in x, y and z directions is seen to belong to the species A_u. Therefore, the atom displacements parallel to x, y or z axis also belongs to the A_u species, as shown in Table 5.27.

Now, the species of the site symmetry is identified for each excursion of the zirconium atom and the displacements that are described become the lattice vibrations in the crystal. Thus, information is integrated by the correlation tables to the species of the factor group that contains this lattice vibration. If t^{γ}

Table 5.23

CHARACTER TABLE FOR POINT GROUP D_{2h}

D_{2h}	E	$C_2(z)$	$C_2(y)$	$C_2(x)$	i	$\sigma(xy)$	$\sigma(xz)$	$\sigma(yz)$		
A_g	1	1	1	1	1	1	1	1		x^2, y^2, z^2
B_{1g}	1	1	-1	-1	1	1	-1	-1	R_z	xy
B_{2g}	1	-1	1	-1	1	-1	1	-1	R_y	xz
B_{3g}	1	-1	-1	1	1	-1	-1	1	R_x	yz
A_u	1	1	1	1	-1	-1	-1	-1		
B_{1u}	1	1	-1	-1	-1	-1	1	1	T_z	
B_{2u}	1	-1	1	-1	-1	1	-1	1	T_y	
B_{3u}	1	-1	-1	1	-1	1	1	-1	T_x	
$\Gamma_{x,y,z}$	3	-1	-1	-1	-3	1	1	1		

Table 5.24

CHARACTER TABLE FOR POINT GROUP C_i

C_i	E	i		
A_g	1	1	R_x, R_y, R_z	x^2, y^2, z^2, xy, xz, yz
A_u	1	-1	T_x, T_y, T_z	
$\Gamma_{x,y,z}$	3	-3		

Table 5.25

CHARACTER TABLE FOR POINT GROUP C_s

C_s	E	σ_h		
A'	1	1	T_x, T_y, R_z	x^2, y^2, z_2, xy
A''	1	-1	T_z, R_x, R_y	yz, xz
$\Gamma_{x,y,z}$	3	1		

Table 5.26

CHARACTER TABLE FOR POINT GROUP C_1

C_1	E
A	1

represents the number of translations in each site species γ and f^{γ} represents the degrees of vibrational freedom present in each site species γ, then,

$$t^{\gamma}n = f^{\gamma} \tag{5.53}$$

where n is the number of atoms (ions or molecules) in an equivalent set. There are 3 translations (t^{γ} = 3) in A_u species of C_i and 4 equivalent atoms (n = 4). Thus, the degree of vibrational freedom f^{γ} equals 12 (from equation (5.53). Table 5.28 indicates the presence of the zirconium lattice vibrations designated as degrees of freedom in species A_g and A_u. If a_{γ} is the degree of freedom contributed by each site species γ to a factor group species ζ, then,

$$f^{\gamma} = a_{\gamma}\sum_{0\,\zeta}^{\gamma} C_{\zeta} \tag{5.54}$$

where C_{ζ} is the degeneracy of the species ζ of the factor group.

The next step is to correlate the species of C_i to the D_{2h} factor group species. Using the correlation tables (116,117), the relationship between the site and factor groups is obtained as shown in Table 5.29. Since only the site species A_u contains the translations T_x, T_y and T_z, which are the lattice vibrations in the crystal, the correlations relating these species to the species in this factor group are of immediate interest. By integrating the site species which contains the translations into the factor group through the correlation table (Table 5.29), it is easy to identify these lattice vibrations in the factor group species. Table 5.29 shows this correlation and identifies the species of the lattice vibration in the crystal.

The irreducible representation of the zirconium atom for the factor group is obtained from the equation:

$$\Gamma = \sum_{\zeta} a_{\zeta}\zeta \tag{5.55}$$

Table 5.27

DEGREES OF FREEDOM IN C_i SITE SPACIES

C_i site species	Translation	t^γ	$f^\gamma = nt^\gamma$
A_g		0	0
A_u	$T_{x,y,z}$	3	12

* Zirconium atoms is on site C_i. The degrees of vibrational freedom for each species for n = 4 atoms/equivalent set.

Table 5.28

RELATIONSHIP BETWEEN SITE AND FACTOR GROUPS

C_i	Correlation	D_{2h}
A_g	→	A_g
	→	B_{1g}
	→	B_{2g}
	→	B_{3g}
A_u	→	A_u
	→	B_{1u}
	→	B_{2u}
	→	B_{3u}

Table 5.29

CORRELATION BETWEEN SITE SYMMETRY C_s AND FACTOR GROUP D_{2h}

f^{γ}	t^{γ}	C_s Site Species γ	Correlation $\longrightarrow$	D_{2h} Factor Gr. Species ζ	C_{ζ}	$a_{\zeta} = \Sigma_{\gamma} a_{\gamma}$ $(a_{A'} + a_{A''})$
8	2(T_x, T_y)	A'	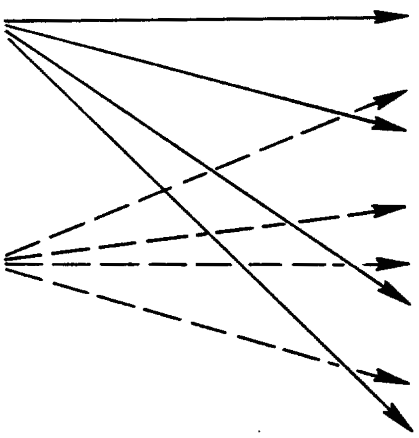	A_g	1	2 = 2 + 0
				B_{1g}	1	1 = 0 + 1
				B_{2g}	1	2 = 2 + 0
				B_{3g}	1	1 = 0 + 1
4	1(T_z)	A''		A_u	1	1 = 0 + 1
				B_{1u}	1	2 = 2 + 0
				B_{2u}	1	1 = 0 + 1
				B_{3u}	1	2 = 2 + 0

Therefore, the species of the factor group which contains the lattice vibrations involving the zirconium atom can be written as the following irreducible representation Γ_{Zr}, viz.,

$$\Gamma_{Zr} = 3A_u + 3B_{1u} + 3B_{2u} + 3B_{3u} \qquad (5.56)$$

Following the same procedure outlined above, the irreducible representations Γ_{Sr} and Γ_{Oxy} can be obtained for the equivalent set of strontium and oxygen atoms. Tables 5.30 and 5.31 show the correlations of site symmetry C_s and factor group D_{2h} and site symmetry C_1 and factor group D_{2h} respectively and also identify the species of the lattice vibrations in the crystal.

Strontium atoms in $SrZrO_3$ occupy the C_s site symmetry. Hence, from Table 5.30, the irreducible representation of strontium atoms for the factor group can be written as :

$$\Gamma_{Sr} = 2A_g + B_{1g} + 2B_{2g} + B_{3g} + A_u + 2B_{1u} + B_{2u} + 2B_{3u} \qquad (5.57)$$

Four equivalent oxygen atoms occupy the C_s site symmetry. Hence, the irreducible representation of the oxygen atoms can be obtained from Table 5.30 as follows:

$$\Gamma_{O_I} = 2A_g + B_{1g} + 2B_{2g} + B_{3g} + A_u + 2B_{1u} + B_{2u} + 2B_{3u} \qquad (5.58)$$

The irreducible representation of the species of the factor group, which contains the lattice vibrations involving the other eight equivalent oxygen atoms occupying the C_1 site symmetries, can be written from Table 5.31 as :

$$\Gamma_{O_{II}} = 3A_g + 3B_{1g} + 3B_{2g} + 3B_{3g} + 3A_u + 3B_{1u} + 3B_{2u} + 3B_{3u} \qquad (5.59)$$

The total representations of the crystal Γ_{SrZrO_3} can be construed as the sum of the individual irreducible representations for each set of equivalent atoms, viz.,

$$\Gamma_{SrZrO_3} = \Gamma_{Sr} + \Gamma_{Zr} + \Gamma_{O_I} + \Gamma_{O_{II}} \qquad (5.60)$$

Table 5.30

CORRELATION BETWEEN SITE GROUP C_i AND FACTOR GROUP D_{2h}

f^γ	C_i Site Species γ	Correlation $\longrightarrow$	D_{2h} Factor Gr. Species ζ	C_ζ	$a_\zeta = \Sigma_\gamma a_\gamma$
12 $(T_{x,y,z})$	A_u	$\longrightarrow$	A_u	1	3
		$\longrightarrow$	B_{1u}	1	3
		$\longrightarrow$	B_{2u}	1	3
		$\longrightarrow$	B_{3u}	1	3

Table 5.31

CORRELATION BETWEEN SITE SYMMETRY C_1 AND FACTOR GROUP D_{2h}

f^{γ}	t^{γ}	C_1 Site Species	Correlation $\longrightarrow$	D_{2h} Factor Gr. Species ζ	C_{ζ}	a_{ζ}
24	$3(T_x, T_y, T_z)$	A	$\longrightarrow$	A_g	1	3
			$\longrightarrow$	B_{1g}	1	3
			$\longrightarrow$	B_{2g}	1	3
			$\longrightarrow$	B_{3g}	1	3
			$\longrightarrow$	A_u	1	3
			$\longrightarrow$	B_{1u}	1	3
			$\longrightarrow$	B_{2u}	1	3
			$\longrightarrow$	B_{3u}	1	3

Summing up equations (5.56) through (5.59),

$$\Gamma_{SrZrO_3} = 7A_g + 5B_{1g} + 7B_{2g} + 5B_{3g} + 8A_u + 10B_{1u} + 8B_{2u} + 10B_{3u} \qquad (5.61)$$

There are 3N degrees of freedom for a crystal containing N atoms in the primitive cell. Of the 3N degrees of freedom, three represent pure translations and appear as the acoustic modes involved in the propagation of sound waves through the crystal. The remaining 3N-3 modes are distributed between internal (molecular) modes, translatory (lattice vibrational) modes and rotatory modes. The three acoustical vibrations are included in the irreducible representations (Γ_{SrZrO_3}) given above and these are readily identifiable in factor groups, since they have the same character as the translations. These acoustic modes are B_{1u}, B_{2u} and B_{3u} species of the factor group D_{2h}. When those vibrations at the center of the Brillouin zone (that is, k=0) are considered, the three acoustical vibrations have nearly zero frequency. Since vibrations with zero frequency are of no physical interest here, they can be subtracted from the irreducible representations, giving,

$$\Gamma^{vib}{}_{SrZrO_3} = 7A_g + 5B_{1g} + 7B2g + 5B_{3g} + 8A_u + 9B_{1u} + 7B_{2u} + 9B_{3u} \qquad (5.62)$$

The results of this factor group analysis indentify the number of lattice vibrations in each species and the spectral activity of each mode.The modes having Raman polarizibility tensors are involved in Raman scattering. In order to be active in infrared absorption, a mode should have a translation vector in its irreducible representation. The results are summarized in Table 5.32. which gives the following selection rules for first-order Raman and IR activity in the $SrZrO_3$ crystal:

For the Raman spectra, 24 fundamental lattice vibrations are allowed ($7A_g + 5B_{1g} + 7B_{2g} + 5B_{3g}$) and for infrared spectra, 25 fundamental lattice vibrations are allowed ($9B_{1u} + 7B_{2u} + 9B_{3u}$).

Table 5.32

RESULTS OF FACTOR GROUP ANALYSIS FOR $SrZrO_3$

D_{2h} Factor Gr. Species	Translation Species	Acoustic Mode	$\Gamma^{crystal}_{SrZrO_3}$ Coefficient	$\Gamma^{vib}_{SrZrO_3}$ Coefficient	IR Activity	Raman Polarization Tensor Species	Raman Activity
A_g			7	7		$\alpha_{xx}+\alpha_{yy}+\alpha_{zz}$	
B_{1g}			5	5		α_{xy}	
B_{2g}			7	7		α_{xz}	
B_{3g}			5	5		α_{yz}	
A_u			8	8			
B_{1u}	T_z	1	10	9			
B_{2u}	T_y	1	8	7			
B_{3u}	T_x	1	10	9			

There will be no coincidences of the same vibrational mode which is active and observable by both the Raman effect and in the infrared spectrum. The A_u mode is a silent mode, that is, neither IR or Raman active. In this silent mode, only the oxygen atoms vibrate, with the zirconium and strontium atoms remaining fixed.

In the present study, when the Raman spectra obtained at 298, 277 and 77 K (Figures 42 and 5.43) are compared, no evidence of phase transitions is seen. Other investigators also did not observe any low temperature phase transitions in this system but at higher temperatures, found evidence for such phase transitions. Carlsson (37,51) identified an antiferroelectric to paraelectric transition at 1443 K in addition to two other phase transitions at 973 and 1123 K in $SrZrO_3$. Krainik (118) also predicted a transition between a non polar and a paraelectric phase at 1373 K and another transition between non polar phases at 973 K in this system. Ahtee et al (52,53) identified only an orthorhombic structure upto 993 K, as evidenced by the observation of neutron powder profile reflections due to tilted octahedra and displaced cations, corresponding to the space group P_{bnm}. The absence of phase transitions in the present study is consistent with the above results. The superlattice reflections, associated with tilted octahedra, obtained by Ahtee et al (52,53), can be applied to a pseudocubic system, wherein the lattice relationship is $a_p = b_p \neq c_p$, with $\gamma \neq 90^\circ$, to yield the $SrZrO_3$ tilt system as $a^- a^- c^+$, corresponding to the space group P_{bnm}. Further, the reflections due to displaced cations are consistent with having cations within any layer perpendicular to [001] displaced parallel to one another, but with the displacements in successive layers antiparallel (an arrangement, common in perovskites having this type of tilt system). As to the oxygen environment around strontium ions caused by tilting, simple packing considerations suggest that the effect of oxygen atoms is to push the strontium ions slightly away from the centers. In Figure

5.45, the true orthorhombic unit cell is indicated, wherein Zr ions lie on centers of symmetry (and hence, cannot be displaced). However, the Sr atoms are displaced along b_0, parallel to one another within (001) layers, each successive layer being antiparallel. The oxygen tetrahedra in this system are very regular with a mean Zr-O bond length of 2.091 A and a mean O-O bond length of 2.957 A. With respect to the orthorhombic cell, the octahedra are tilted 7.6° about c_0 and 11.2° about b_0 (that is, about the direction of Sr displacement). These tilt angles cause distortion of the environment of the Sr atoms, tending to push these atoms away from the center. The resultant Raman active lattice vibrational modes in such an oxygen tetrahedra compound should exhibit high scattering efficiencies, leading to fairly broad Raman lines, with some degree of the relaxation of the Raman selection rules. However, in the spectra of Figure 5.42 it appears that either many of the bands originating from the factor group overlap or that the polarizabilities of many modes are low enough to prevent their bands from being seen. Further, the intensity of the spectral lines is a function of the orthorhombic distortion and it is likely that the distortions involved in $SrZrO_3$ are not large enough to yield spectral resolution. To verify this hypothesis, Raman spectrum was obtained from $CaZrO_3$ powder specimens prepared by standard liquid mix technique at 298 K (Figure 5.46). This system was chosen because it is structurally identical to $SrZrO_3$. with a space group representation of ${D_{2h}}^{16} - P_{bnm}$. The resulting spectrum is similar to that of $SrZrO_3$ (Figure 5.38), with much higher Raman line intensities. Small variations in the peak positions between the two systems are due to differences in the bond force constants and relative masses of the atoms.

In studies of Raman scattering involving other perovskite crystals, observed spectra were distinguished into internal modes of the oxygen octahedra and external modes due to the lattice vibrations involving cation motions

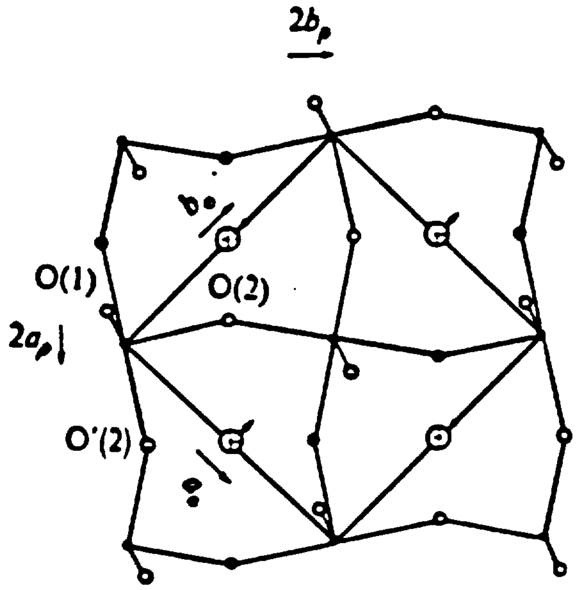

Figure 5-45: ORTHORHOMBIC UNIT CELL OF $SrZrO_3$ STRUCTURE SHOWING ONE [53] LAYER OF OCTAHEDRA PERPENDICULAR TO c_0

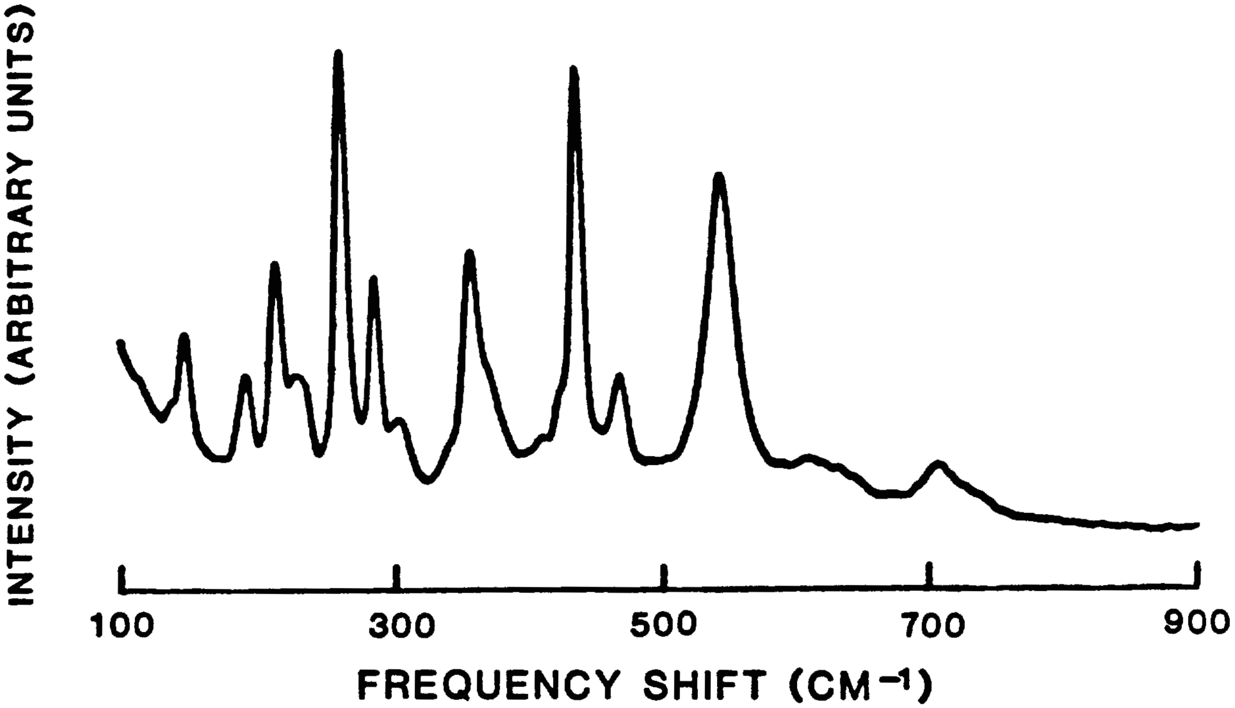

Figure 5-46: RAMAN SPECTRA OF POLYCRYSTALLINE $CaZrO_3$ AT ROOM TEMPERATURE

with respect to the octahedra framework (63,119,120). These external modes are situated in the low frequency part of the Raman spectra ($\leq 100\ cm^{-1}$) and depend on the combination of the cations (120). Similarly, the fundamental vibrational modes in $SrZrO_3$ also can be classified into the internal ZrO_3 vibrations and the external vibrations of Sr against the ZrO_3 group. The interactions between these motions depend upon the masses and restoring forces of the vibrating atoms, and can be expected to be small for $SrZrO_3$ when compared with $CaZrO_3$ (Figures 5.42 and 5.46).

The Sr - (ZrO_3) vibrations can be studied by considering the ZrO_3 group as a single atom and treating the vibrational problem as that of a diatomic crystal of equivalent structure. The ZrO_3 group is considered to be arranged as a central Zr atom octahedrally surrounded by six O half-atoms, to give the group the correct symmetry properties. If a vertical axis is chosen through a Zr-O chain, and the two O half-atoms lying along this chain are labelled O_I, with the four O half-atoms at right angles to this axis labelled O_{II}, the two A_{1g} normal vibrations can be illustrated as shown in Figure 5.47 [128]. In Figure 5.47a the motion is primarily that of a change of length of the $Zr-O_I$ bond. In Figure 5.47b, the motion is that of a change in the $O_{II}-Zr-O_I$ bond angle. Both the relative magnitude and sign of the displacements will depend on the bond-force constants and relative masses of the atoms. The above analysis can be applied to interpret the experimental results. Two sets of strong lines were seen around 555 and 415 cm^{-1} (Figure 5.42). The observation of a similar pair of intense lines in other zirconate systems ($CaZrO_3$, $SrZrO_3$ and $PbZrO_3$) elsewhere (46) and also in this study (Figure 5.46) indicates that these lines are the internal modes of ZrO_3 octahedra. Using group theory analysis, it can be shown that three of the A_g modes which are Raman active modes are the stretching vibrational modes. Further, A_g symmetry is a total symmetry and hence, will have high frequency

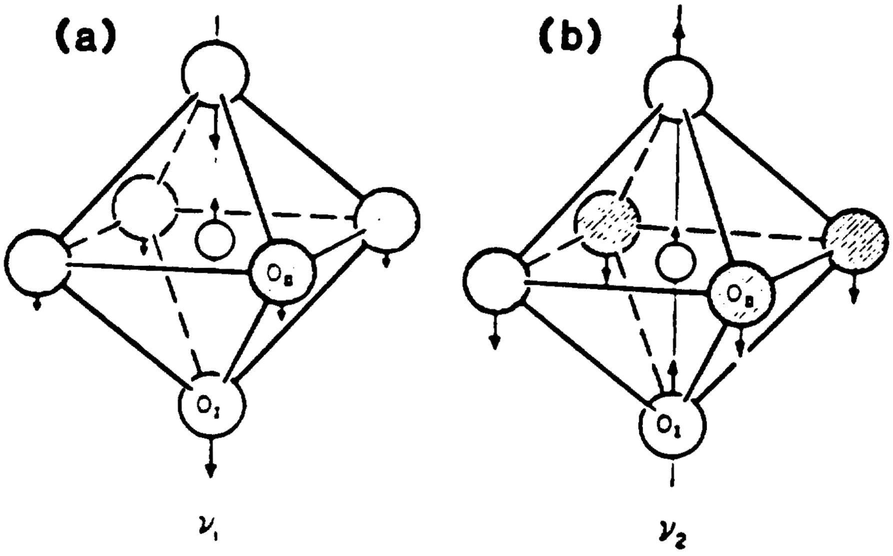

Figure 5-47: SCHEMATIC NORMAL VIBRATION OF A ZrO_6 OCTAHEDRON [128]
ν_1: higher-frequency 'stretching vibration'
ν_2: lower-frequency 'bending vibration'

vibrational modes. The line at 555 cm^{-1} is attributed to the A_g 'stretching' vibration of free ZrO_3 molecules, since the modes in which band stretching occurs are found at higher frequencies than those for bending vibrations involving those same bonds (121). The band at 415 cm^{-1} is assigned to the O-Zr-O bending mode. Bands below 150 cm^{-1} are assigned to the external modes due to the Sr - (ZrO_3) lattice vibrations. All the above Raman modes were stable with respect to temperature (Figure 5.43), consistent with the fact that these are fundamental vibrational modes. This is also in agreement with the tentative band assignment for $SrZrO_3$ proposed by Pasto and Condrate (46).

The peaks at 340 and 120 cm^{-1} exhibited a temperature dependence, with the intensity decreasing with decreasing temperature (Figure 5.43). This indicates that these peaks are obviously not fundamental vibrational modes. Following the space group selection rules for two-phonon Raman scattering for a crystal lattice possessing inversion symmetry that have been derived by Loudon (122,123), these two peaks can be assigned as the difference combination band of the two phonons. In addition, the low intensity peak at about 620 cm^{-1} is believed to be an impurity induced band because this Raman band is strongly sample dependent. Further, from the high temperature electrical conductivity studies (Section 5.3), there is evidence for the presence of small amounts of acceptor impurities in the sample.

Room temperature Raman spectra of La-doped $SrZrO_3$ were also obtained at three dopant levels (1, 4 and 6 at.%), as shown in Figure 5.48. The strong lines at 555 and 415 cm^{-1} remained essentially unchanged when compared with the Raman spectra of the undoped sample (Figure 5.42), except for a change in the shoulder position (at 394 cm^{-1}) on the right hand side of the low frequency peak (415 cm^{-1}). This secondary peak (394 cm^{-1}) shifted to the left and at higher La concentration almost merged with the main peak at 415 cm^{-1}. Below 300 cm^{-1},

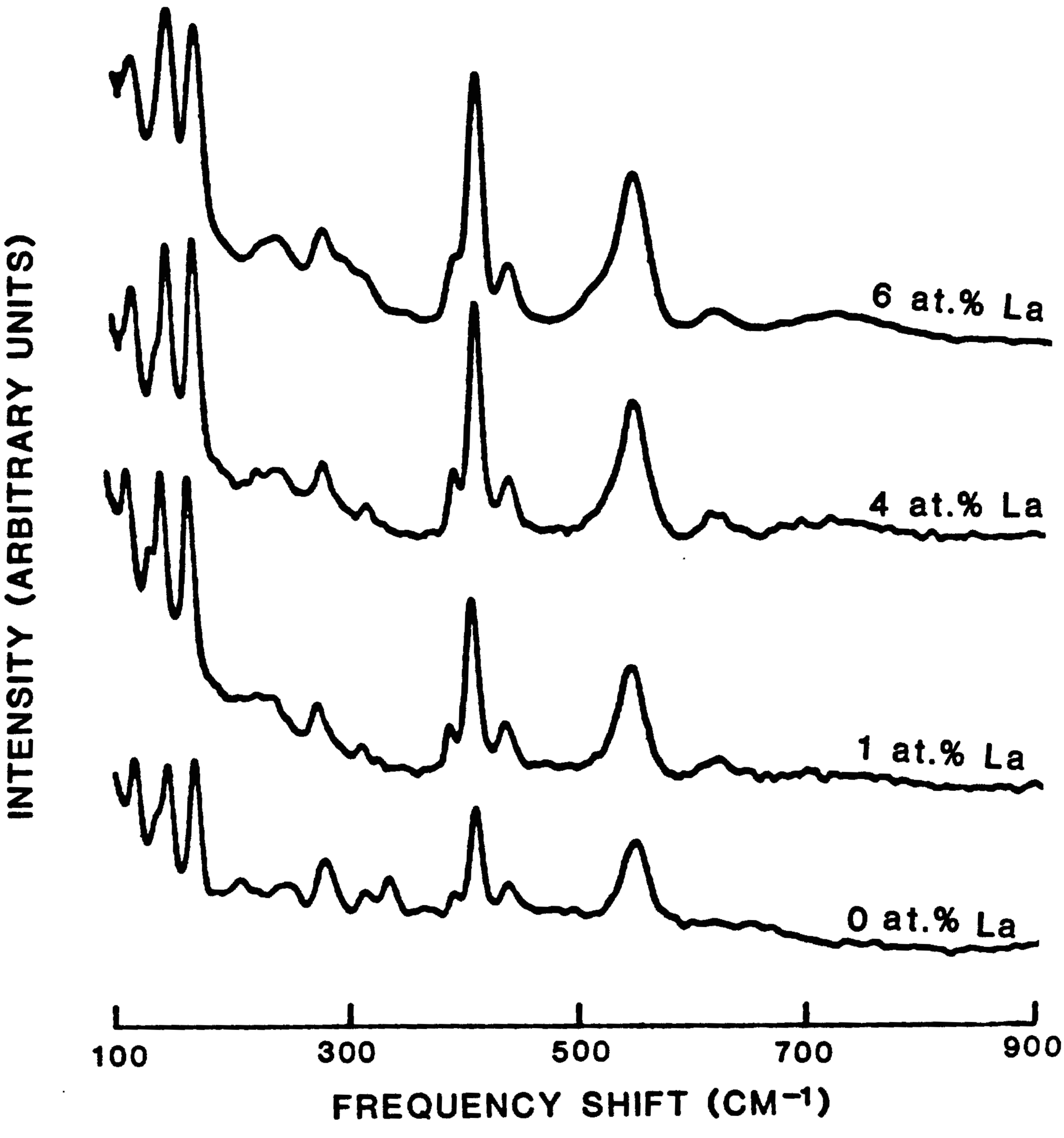

Figure 5-48: RAMAN SPECTRA OF POLYCRYSTALLINE $SrZrO_3$ AS A FUNCTION OF *La* CONCENTRATION

spectral resolution decreased and only a broad band was observed.

Pasto and Condrate (46) studied the effecs of Al and Si additions on the Raman spectra of $SrZrO_3$. They observed a drastic change in the spectra, unlike the results of this investigation, in which only minor changes were noted. The reason for this anamoly could be due to the nature of impurity incorporation in the lattice. Al (or Si) substitutes for Zr and hence major changes in the Raman spectra would result in the internal modes of vibration (the basic oxygen tetaherdra is now Al_2O_3), due to differences in the atomic masses and bond force constants. However, when La is added, these atoms occupy Sr sites and hence any changes in the spectra would be observed only in the external vibrational modes, that is, at lower frequencies (where only a broad band was observed in this study). It is interesting to compare the results of this work with those obtained by Prater et al for Nb-doped and Li-doped $KTaO_3$ (59,60). The Raman spectra were obtained only below 200 cm^{-1}. When Nb was added to $KTaO_3$, no effect on the intensity of any disorder- induced features were obtained. The major peak in $KTaO_3$ was noted at 90 cm^{-1} and since $KTaO_3$ is ideal cubic, this peak was attributed to the presence of native Li impurities. On the other hand, when Li was added to $KTaO_3$, disorder-induced scattering features were observed in the spectra. The low frequency peaks increased in intensity with increasing Li concentration. However, in the present study, addition of La to $SrZrO_3$ decreased the intensity of the low frequency peaks. $KTaO_3$ is ideal cubic and addition of Nb or Li increases lattice distortion. Nb replaces Ta and hence, changes in the spectra would be obtained mostly at higher frequencies (internal vibrational modes), consistent with the absence of disorder-induced features with Nb addition below 200 cm^{-1}. Li substitutes for K and thus the low frequency spectra (external vibrational modes) will change, as was observed by the above investigators. The intensity was found to increase with increasing Li because of increasing lattice distortion. In the present study, where $SrZrO_3$, a distorted perovskite, was used, addition of La reduces the extent of distortion and consequently leads to a decrease in the intensity of the low frequency bands.

CONCLUSIONS

6.1 Solubility Limit of La in $SrZrO_3$

1. No changes in the microstructure of $SrZrO_3$ were observed upto 6 at.% La additions through scanning electron microscopy. When the amount reached 7 at.%, acicular precipitates started appearing and these were rich in La and Zr electron counts, with virtually no Sr counts, as determined by energy dispersive x-ray analysis.
2. The structure of $SrZrO_3$ was identified as orthorhombic by x-ray diffraction. The lattice constant of $SrZrO_3$ decreased with increasing La additions, upto 6 at.%, consistent with a Vegard's law dependency, but remained constant for higher concentrations. Through both x-ray fluorescence and x-ray diffractometry, the extra lines in the diffraction patterns above 6 at.% were identified as those due to $La_2Zr_2O_7$.
3. Transmission electron microscopy confirmed the above results. No second phase reflections were observed in the selected area diffraction patterns upto 6 at.% La additions. At higher values, dark field images obtained using extra reflections assignable to $La_2Zr_2O_7$, clearly highlighted the needle -shaped second phase.
4. The solubility limit of La in $SrZrO_3$ was thus determined to be 6 at.% by the above methods. A tentative partial ternary diagram of $SrO-La_2O_3-ZrO_2$ system was also proposed, consistent with the experimental results.

6.2 Thermogravimetric Measurements

1. Thermogravimetric studies showed that the reversible change of oxygen content, between specified states of oxidation and reduction, was proportional to the La concentration. In the oxidized state, undoped $SrZrO_3$ samples were light purple in color and doped samples were light yellow. In the reduced state, all undoped and doped samples were dark in color.
2. There was good agreement between the calculated amount of oxygen necessary to compensate for the La^{+3} ions and the measured reversible oxygen weight change, with self compensation occurring right upto the solubility limit of La in $SrZrO_3$.
3. A model was proposed to explain the compensation of donor- doped $SrZrO_3$, through the creation of Sr vacancies, with the resulting additional Sr atoms combining with oxygen to form ordered layers of SrO between $SrZrO_3$ unit cells (structural accommodation).

6.3 Electrical Conductivity of Undoped $SrZrO_3$

1. Undoped $SrZrO_3$ exhibited p-type conductivity throughout the temperature (1173-1373 K) and oxygen partial pressure (10^0-10^{-15} atm.) ranges of study.
2. A point defect chemistry approach was used to study the conductivity behavior. The P_{O_2} range was subdivided into high and intermediate regions. In the high P_{O_2} region (10^0-10^{-4} atm.), the variation of conductivity was consistent with a Schottky reaction with a simplified neutrality condition of:

$$[p] = 2[V_A''] + 4[V_B''''] \tag{1.37}$$

The conductivity variation as the 3/16 power of P_{O_2} was accounted for by considering the oxidation reaction:

$$\frac{3}{2}O_2 = 3O_O + V_A'' + V_B'''' + 6p \qquad (5.6)$$

The activation enthalpy for the above reaction was calculated to be 167.06 Kcal/mole. In the intermediate P_{O_2} region (10^{-7}–10^{-15} atm.), the conductivity varriation was explained by considering a defect model, emphasizing the role of acceptor impurities, with a simplified neutrality condition of:

$$2[V_O^{\cdot\cdot}] = A' \qquad (5.11)$$

The dependency of conductivity as the 1/4 power of P_{O_2} in this region was due to the oxidation reaction:

$$V_O^{\cdot\cdot} + \frac{1}{2}O_2 = O_O + 2p \qquad (5.10)$$

The activation enthalpy for the above reaction was evaluated as 43.65 Kcal/mole.

3. An alternative explanation for the conductivity behavior was also developed, by treating the entire P_{O_2} range as a single region, and was considered more probable than the first case, wherein the conductivity invariant region (between the high and intermediate P_{O_2} regions), predicted by defect chemistry analysis, was not experimentally observed. The conductivity variation (very nearly as the 1/4 power of P_{O_2} throughout the pressure range) was attributable to the acceptor impurity effect, similar to the treatment of the intermediate P_{O_2} region in the first case. The activation enthalpy for the oxidation reaction was calculated to be 42.87 Kcal/mole.

6.4 Electrical Conductivity of La-doped $SrZrO_3$

1. For 0.05 at.% La-doped samples, a conductivity minimum was observed, with p-type behavior in the high P_{O_2} region and n-type behavior in the low P_{O_2} region. The temperature range of study was 1173-1373 K and the oxygen partial pressure range was $10^0-10^{-19} atm$. Conductivity varied as the 1/4 power of P_{O_2} in the p-type region and was explained by considering the reaction:

   $$2La_{Sr}^{\cdot}+Sr_{Sr}+\frac{1}{2}O_2 = SrO+2La_{Sr}^{\cdot}+V_{Sr}''+2p \qquad (5.2)$$

   where SrO is formed as ordered layers between $SrZrO_3$ unit cells. The simplified neutrality condition considered in this region was:

   $$[La^{\cdot}] = 2[V_{Sr}'' = constant \qquad (5.16)$$

   In the n-type region, conductivity variation as the -1/4 power of P_{O_2} was explained by considering the higher concentration of electrons together with the same neutrality condition and the oxidation reaction as in the p-type region. From the minima in the conductivity at the n-p transition, the band gap energy of $SrZrO_3$ was calculated to be 3.4 eV. The activation enthalpies for the conduction reaction in the p and n-type regions were determined to be 54.21 Kcal/mole and 130.47 Kcal/mole respectively.

2. The 0.1 at.% La-doped samples exhibited p-type behavior in the high P_{O_2} region but a conductivity invariant behavior in the low P_{O_2} region. The conductivity variation as the 1/4 power of P_{O_2} in the high P_{O_2} region was similar to the behavior of the 0.05 at.% La-doped samples. The invariant conductivity in the low P_{O_2} region was accounted for by considering the reaction:

   $$La_2O_3 = 2La^{\cdot}_{Sr}+2n+2O_O+\frac{1}{2}O_2 \qquad (5.20)$$

The corresponding neutrality condition considered in this region was:

$$[La^{\cdot}] = [n] = constant \tag{5.22}$$

As predicted by point defect chemistry theory, a small n-type region was also observed between the p-type and the conductivity invariant regions.

3. The absolute conductivity values in the p-type region in both the 0.05 at.% and 0.1 at.% La-doped samples were lower than the corresponding values for pure $SrZrO_3$. However, when compared with each other, the 0.1 at.% La-doped samples exhibited a half order of magnitude higher values. The mean grain size of the 0.05 at.% and 0.1 at.% La-doped samples were measured as 600 and 700 nm respectively and the higher conductivity of the latter samples was attributed to the grain size and associated density effects.

6.5 Chemical Diffusion Coefficient in Undoped $SrZrO_3$

1. The activation enthalpy for the motion of oxygen vacancies was evaluated from the chemical diffusion coefficient data to be 16.62 Kcal/mole. The enthalpy of formation of these defects, calculated as 42.87 Kcal/mole from equilibrium conductivity data for undoped $SrZrO_3$, was combined with the enthalpy of motion, to yield the enthalpy for the total process of self - diffusion of ionized oxygen vacancies in $SrZrO_3$ as 26.25 Kcal/mole.
2. The chemical diffusion coefficient was independent of P_{O_2} value for small step changes in P_{O_2} and also for larger step changes under oxidizing conditions.

6.6 Interdiffusion in $BaZrO_3$ - $SrZrO_3$

1. Penetration curves of Sr and Ba possessed gentle slopes in the $BaZrO_3$ rich side but sharply increased with Sr concentration, indicating that interdiffusivity was a strong function of concentration.
2. There was good agreement between the values calculated from the concentration profiles of the two diffusing species. The activation enthalpy for the interdiffusion process was determined to be 73.11 Kcal/mole.

6.7 Raman Spectra of $SrZrO_3$

1. Factor group analysis was used to interpret the Raman spectra of $SrZrO_3$ on the basis of space group $D_{2h}{}^{16}$ - P_{bnm}. The irreducible representations of the 4Zr (C_i - sites), 4Sr(C_s-sites), 4O($C_s$$-sites$) and 8O($C_1$$-sites$) atoms, calculated individually were summed and the three degrees of freedom, representing pure translations (acoustic modes) were subtracted from these 3N degrees of freedom to yield the total representation of the $SrZrO_3$ crystal as:

   $$\Gamma_{SrZrO_3} = 7A_g+5B_{1g}+7B_{2g}+5B_{3g}+8A_u+9B_{1u}+7B_{2u}+9B_{3u} \qquad (5.62)$$

   Raman and infrared active modes were separated from these and the results were applied to the experimental Raman spectra obtained at 298, 277 and 77 K.
2. No phase transitions were seen when the Raman spectra obtained at different temperatures were compared. Due to overlapping of many of the bands originating from the factor group, low polarizabilities of many of the modes and small distortions in the $SrZrO_3$ crystal which prevent spectral

resolution, many of the Raman active modes were not observed.

3. The fundamental vibrational modes were classified into internal ZrO_3 vibrations and external vibrations of Sr against the ZrO_3 group. In particular, the spectral line at 555 cm^{-1} was attributed to the A_g stretching vibration of free ZrO_3 molecules and the band at 415 cm^{-1} was assigned to O-Zr-O bending mode. Bands below 150 cm^{-1} were assigned to the external modes due to the Sr-ZrO_3 lattice vibrations. All these fundamental Raman vibrational modes were stable with respect to temperature. The peaks at 340 and 120 cm^{-1} exhibited a direct temperature dependence (non-fundamental modes) and were assigned as the difference combination band of the two phonons. The low intensity peak at 620 cm^{-1} was an impurity induced band. Room temperature Raman spectra of 1,4 and 6 at.% La-doped $SrZrO_3$ indicated a shifting of the secondary peak at 394 cm^{-1} to higher wavelength and at higher La concentration, the secondary peak almost merged with the main peak at 415 cm^{-1}. Below 300 cm^{-1} spectral resolution decreased and only a broad band was observed.

REFERENCES

1. F.A. Kroger and H.J. Vink, Solid State Phys., 3, 307 (1956).
2. H. Schmalzried, and C. Wagner, Z. Phys. Chem. N.F., 31, 198 (1962).
3. J. Frenkel, Z. Phys. 35, 652 (1926).
4. C. Wagner and W. Schottky, Z. Phys. Chem., B11, 163 (1930).
5. W. Schottky, Z. Phys. Chem., B29, 335 (1935).
6. W. Jost, J. Chem. Phys., 1, 466 (1933).
7. C. Wagner, Z. Phys. Chem., Bodenstein Festband, 177 (1931).
8. C. Wagner, Z. Phys. Chem., B22, 181 (1933).
9. D.G. Thomas and J.J. Lander, J. Chem. Phys., 25, 1136 (1956).
10. J.B. Price and J.B. Wagner, Z. Phys. Chem., 49, 257 (1966).
11. L.C. Walters and R.E. Grace, J. Phys. Chem. Solids, 28, 245 (1967).
12. W.L. George and R.E. Grace, J. Phys. Chem. Solids, 30, 889 (1969).
13. A.B. Newman, Trans. Am. Inst. Chem. Engrs., 27, 310 (1931).
14. R.H. Campbell, W.J. Kass and M. O'Keeffe, 'Interdiffusion Coefficients from Electronic Conductivity Measurements - Application to Cu_2O ', Presented at NBS Conf. on Mass Transport in Oxides, Washington D.C. (1967)
15. G.H. Haertling and C.E. Land, J. Amer. Ceram. Soc., 54 [1], 1 (1971).
16. W.A. Schulze, T.G. Miller and J.V. Biggers, J. Amer. Ceram. Soc. 58 [1-2], 21 (1975).
17. T. Ikeda and T. Okano, Jap. J. Appl. Phys., 3 [2], 63 (1964).
18 T. Ikeda, ibid., 3 [8], 493 (1964).
19. D.A. Berlincourt, 'Research on Piezoelectric Materials and Phenomena', Sandia Laboratories Summary Rep. # 323160 (1965).

20. K.H. Hardtl and D. Hennings, J. Amer. Ceram. Soc., 55 [5], 230 (1972).

21. T. Sasamoto, W.R. Cannon and H.K. Bowen, Ceramic International, 7 [1], 3 (1981).

22. N.G. Eror and D.M. Smyth, 'The Chemistry of Extended Defects in Non-Metallic Solids', L. Eyring and M. O'Keefe (Eds.), North-Holland Pub.Co. (Amsterdam) 62 (1970).

23. J. Bouwma, K.J. Devries and A.J. Burggraff, Phys. Stat. Sol. (A), 35, 281 (1976).

24. T.Y. Tien and A. Hummel, Trans. Brit. Ceram. Soc., 66, 233, (1967).

25. U. Balachandran and N.G. Eror, Comm. Amer. Ceram. Soc., C-75, April 1981.

26. B.C. Tofield and W.R. Scott, J. Solid State Chem., 10, 183 (1974).

27. D. Hennings, Mat. Res. Bull., 6, 329 (1971).

28. T.L. Pivovar and V.Ya. Tolstaya-Belik, High Temp., 8, 1227 (1970).

29. A.M. Anthony, A. Guillot, T. Sata and J. Bourgeois, Rev. Hautes. Temp. et Refract., 3, 147 (1966).

30. V. Longo and F. Ricciardiello, 'Conducibilita Electrica Di Composite Perovsketici', Instituto Di Chemica Applicata E. Industriale Rep. # N.87 (1979).

31. V. Longo and F. Ricciardiello, Science of Ceramics, 11, 539 (1981).

32. V. Longo and F. Ricciardiello, 'Considerazioni Sulla Struttura E Sul Meccanismo Di Conduzione Elettrica Di Titanati, Zirconati E Cerati Di Metalli Alcalino-Terrosi', Instituto Di Chimica Applicata E. Industriale Rep # N.88 (1979).

33. A.M. Anthony and M. Foex, Proc. Symp. on Magneto Hydrodynamic Electrical Power, Salzburg, Austria, July 1966, National Agency for International Publication Inc. (New York) 3, 265 (1966).

34. V. Longo and F. Ricciardiello, 'Meccanismi Di Conduzione Eletrica per La Soluzione Solida $CaZrO_3 - SrZrO_3$', Instituto Di Chimica Applicata E. Industriale Rep. # N.89 (1979).

35. V. Longo and F. Ricciardiello, Silic. Ind. 46 [1], 3 (1981).

36. H.P.R. Frederikse and W.R. Hosler, 'Electrical Conductivity of M.H.D.-Channel Materials' NBS (Washington D.C.) 4, 2 [1-3]

37. L. Carlsson, Acta Cryst., 23, 901 (1967).

38. N.I. Budim and M.S. Kozyreva, Izv. Akad. Nauk. SSSR, Neorg. Mates., 7 [8], 1451 (1971).

39. H. Dunwald and C. Wagner, Z. Phys. Chem., Abt. B24, 53 (1934).

40. J. Daren, Z.M. Jarzebski, S. Mrowec and T. Walec, Bull. Acad. Polon. Sci. Ser. Sci. Chim., 14 [2], 153 (1971).

41. D.G. Thomas and J.J. Lander, J. Chem. Phys. 25, 1136 (1956).

42. F.S. Ozdemir and R.J. Schwartz, Ceram. Bull., 51 [5], 474 (1972).

43. A.F. Iatsenko, Bull. Acad. Sci. USSR (Phys. Series), 22,1450 (1958).

44. C.H. Perry, D.J. Mc Carthy and G. Ruppecht, Phys. Rev., A 138, 1537 (1965).

45. T. Dupuis and M.V. Lorenzelli, C.R. Acad. Sci. (Paris), B264, 1019 (1967).

46. A.E. Pasto and R.A. Condrate, Sr., J. Amer. Ceram. Soc., 56 [8], 436 (1973).

47. A.E. Pasto and R.A. Condrate, Sr., 'Advances in Raman Spectroscopy', J.P. Mathieu (Ed.) Heyden and Son Ltd. 1, 196 (1973).

48. A.J. Smith and A.J.E. Welch, Acta Cryst., 13, 653 (1960).

49. R.W. Roth, J. Res. NBS, 58, 75 (1957).

50. H.E. Swanson, M.I. Cook, T. Isaacs and E.H. Evans, NBS Circ. # 539, 51 (1960).

51. L. Carlsson, J. Mat. Sci., 5, 325 (1970).

52. A. Ahtee, M. Ahtee, A.M. Glazer and A. Hewat, Acta. Cryst., B32, 3243 (1976).

53. M. Ahtee, A.M. Glazer and A.W. Hewat, Acta. Cryst. B34, 752 (1978).

54. R.A. Cowley, Phys. Rev., A981, 134 (1964).

55. A.S. Barker, Jr. and M. Tinkham, Phys. Rev., 125, 1527 (1962).

56. W.G. Spitzer, R.C. Miller, D.A. Kleinman, and L.E. Howard, Phys. Rev., 126, 1710 (1962).

57. P.S. Narayanan and K. Vedam, Zeit. fur. Phys., 163, 158 (1961).

58. W.G. Nelson and J.G. Skinner, J. Chem. Phys., 48 [5], 2240 (1968).

59. C.H. Perry, J.H. Fertel and T.F. McNelley, J. Chem. Phys., 47 [5], 1619 (1967).

60. R.L. Prater, L.L. Chase and L.A. Boatner, Phys. Rev., B23 [11], 5904 (1981).

61. C.H. Perry and D.B. Hall, Phys. Rev. Letters, 15 [17], 700 (1965).

62. S. Kuroda and Kubota, J. Phys. Chem. Solids., 44 [6], 527 (1983).

63. A. Scalabrin, S.P.S. Parto, H. Vargas, C.A.S. Lima and L.C.M. Miranda, Solid State Comm. 24, 291 (1977).

64. M. Pechini, U.S. Patent # 3,330,697, July 11, 1967.

65. C. Marcilly, P. Courty and B. Delmon, J. Amer. Ceram. Soc., 53, 56 (1970).

66. H. Schmalzried, Prog. Solid State Chem., 2, 265 (1965).

67. M. Pechini, U.S. Patent # 3,231,328, Jan. 25, 1966.

68. J.S. Smith, T.R. Dolloff and K.S. Mazdiyasni, J. Amer. Ceram. Soc., 91 (1970).

69. N.G. Eror 'Electrical Conductivity and Thermogravimetric Studies on CoO, NiO and MnO', Ph.D. Thesis, Northwestern Univ., Evanston, Ill. (1965).

70. U. Balachandran 'An Investigation of Undoped and Impurity-Added $SrTiO_3$ ", Ph.D. Thesis, Oregon Graduate Center, Beaverton, Or. (1980).

71. L.S. Darken and R.W. Gurry, J. Amer. Ceram. Soc., 67, 1308 (1945); 68, 1798 (1946).

72. S.P. Mitoff, J. Chem. Phys., 35, 882 (1961).

73. G.H. Jonker, Solid State Electronics, 7, 895 (1964).

74. N.G. Eror and U. Balachandran, J. Solid State Chem., 40, 55 (1981).

75. T. Noguchi, T. Okubo and O. Yonemochi, J. Amer. Ceram. Soc., 52, 178 (1969).

76. G. Tilloca and P.Y. Jorba, Rev. Hautes. Temp. et Refract., 1, 331 (1964).

77. J.B. Nelson and D.P. Riley, Proc. Phys. Soc. (London), 57, 16 (1945).

78. R.S. Roth, J. Res. NBS, 56, 17 (1956).

79. S.N. Ruddlesden and P. Popper, Acta. Cryst., 11, 54 (1958).

80. D.M. Smyth, J. Solid State Chem., 16 [1-2], 73 (1976).

81. N.H. Chan and D.M. Smyth, J. Electrochem. Soc., 123 [10], 1584 (1976).

82. N.H. Chan, R.K. Sharma, and D.M. Smyth, J. Amer. Ceram. Soc., 64 [9], 556 (1981).

83. N.H. Chan, R.K. Sharma and D.M. Smyth, J. Electrochem. Soc., 128 [8], 1762 (1981).

84. N.H. Chan, R.K. Sharma and D.M. Smyth, J. Amer. Ceram. Soc., 65 [3], 167 (1982).

85. J. Mizusaki, T. Sasamoto, W.R. Cannon and H.K. Bowen, J. Amer. Ceram. Soc. 65 [8], 363 (1982).

86. N.G. Eror, J. Solid State Chem., 38 (1981)

87. J.H. Becker and H.P.R. Frederikse, J. Appl. Phys., 33, 447 (1962).

88. T.A. Noland, Phys. Rev., 94, 724 (1954).

89. M. Cardona, Phys. Rev., 140, A651 (1965).

90. M.I. Cohen and R.F. Blunt, Phys. Rev., 168, 929 (1968).

91. A.H. Kahn and A.Y. Leyendecker, Phys. Rev., A1321, 135 (1964).

92. F. Miyauchi, Phys. Soc. Jap., 12, 308 (1957).

93. C.H.J. Goodman, J. Electronics, 1, 115 (1955).

94. T. Murakami, T. Miyashita, M. Nakahara and E. Sekine, J. Amer. Ceram. Soc., 56 [6], (1973).

95. J.J. Dih and R.M. Fulrath, J. Amer. Ceram. Soc., 61, 9 (1978).

96. J.E. Bauerle, J. Phys. Chem. Solids, 30, 2657 (1969).

97. N.M. Beekmans and L. Heyne, Electrochem. Acta., 21, 303 (1976).

98. E. Schouler, G. Giroud and M. Kleitz, J. Chem. Phys., 70 [9], 1309 (1973).

99. S.H. Chu and M.A. Seitz, J. Solid State Chem., 23, 297 (1978).

100. R.W. Powers and S.P. Mitoff, J. Electrochem. Soc., 122 [2], 226 (1975).

101. R.W. Powers 'Superionic Conductors', G.D. Mahan and W.L. Roth (Eds.), Plenum Press (N.Y.) 315 (1976).

102. Da Yu Wang and A.S. Nowick, Proc. Symp. on Grain Boundary Phenomena in Electronic Ceramics, Chicago, Ill., April 1980, L.M. Levinson (Ed.), The Amer. Ceram. Soc. Inc. (Columbus).

103. C. Wagner, Z. Phys. Chem., 11, 139 (1930).

104. C. Wagner, Z. Phys. Chem., 32, 447 (1936).

105. L.S. Daren, Trans. AIME, 175, 184 (1948).

106. J.B. Wagner, Jr., Proc. Symp. held at Gaithersburg, Md., Oct. 1967, J.B. Wachtman, Jr. and A.D. Franklin (Eds.), NBS (Washington D.C.) NBS Spec. Pub. # 291 (1968).

107. P. Kofstad, 'Nonstoichiometry, Diffusion and Electrical Conductivity in Binary metal Oxides', Wiley-Interscience (New York) 1972.

108. J.M. Wimmer, R.N. Blumenthal and I. Bransky, J. Phys. Chem. Solids, 36 [4], 269 (1975).

109. U. Chowdhry and R.L. Coble, J. Amer. Ceram. Soc., 65 [7], 336 (1982).

110. D. Kalar, M. Trontelj and Z. Stadler, J. Amer. Ceram. Soc., 65 [10], 470 (1982).

111. C. Matano, Jap. J. Phys., 8, 109 (1933).

112. J.W. Lee and W.D. Laidig, J. Electronic Mat., 13 [1], 147 (1984).

113. International Tables for X-ray Crystallography, I, N.F.M. Henry and K. Lonsdale (Eds.), (Birmingham, England) 1965.

114. S. Bhagavantam and T. Venkatarayudu, Proc. Indian Acad. Sci., 9A, 224 (1939).

115. W.G. Fately, E.R. Dollish, N.T. McDevitt and F.F. Bentley, 'Infrared and Raman Selection Rules for Molecular and Lattice Vibrations', Wiley-Interscience (New York) 1972.

116. E.B. Wilson, Jr., J.C. Decius and P.C. Cross, 'Molecular Vibrations', Mc Graw-Hill (New York) 1955.

117. D.M. Adams, 'Metal-Ligand and Related Vibrations', St. Martin's Press (New York) 1968.

118. N.N. Krainik, Soviet Phys. Tech. Phys., 3,493 (1958).

119. G. Burns, J.D. Axe and D.F. O'Kane, Solid State Comm., 7, 933 (1969).

120. K.G. Bartlett and L.S. Wall, J. Appl. Phys., 44, 5192 (1973).

121. Harris and Bertolucci, 'Symmetry and Spectroscopy', New York Oxford University Press (New York) 1978.

122. R. Loudon, Adv. Phys., 14, 423 (1960).

123. R. Loudon, Phys. Rev., A1784, 137 (1965).

124. Y.H. Han and D.M. Smyth, "Non-stoichiometry in $CaTiO_3$ ", Paper # 121-E-84, Presented at the 86th Ann. Meet. of the Amer. Ceram. Soc., Pittsburgh, Pa., April-May 1984.

125. Y.H. Han and D.M. Smyth, "Calcium as an Acceptor Dopant in $BaTiO_3$ ", Paper # 13-E-83, Presented at the 85th Ann. Meet. of the Amer. Ceram. Soc., Chicago, Ill., April 1983.

126. T.M. Loehr, W.E. Keyes and P.A. Pincus, Anal. Biochem., 96, 456 (1979).

127. B.M. Sjoberg, T.M. Loehr and J.S. Loehr, Biochem., 21, 96 (1982).

128. J.T. Last, Phys. Rev., 105 [6], 1740 (1957).

BIOGRAPHICAL NOTE

The author was born on January 16, 1952, in Bangkok, Thailand. After attending the Samakom Rongreinraj High School at Bangkok between 1964 and 1966, she joined the Chulalongkorn University, also at Bangkok and obtained a B.S. degree in Chemical Engineering in April 1970. She then served as an Experimental Scientist at the Applied Scientific Research Corp. of Thailand, at Bangkok, before moving over to the Youngstown State University at Youngstown, Ohio, in January 1978, from where she graduated with a M.E. degree in Materials Science in July 1979. At that juncture, she accepted a Research Fellowship in the Dept. of Materials Science and Engineering at the Oregon Graduate Center, Beaverton, Or., where she completed the requirements for the Doctor of Philosophy degree in July 1984.